



**MANAS  
JOURNAL OF  
ENGINEERING**

***MJEN***



**BISHKEK 2024**



ISSN: 1694- 7398  
Year: 2024  
Volume: 12  
Special Issue: 2  
<http://journals.manas.edu.kg>  
[journals@manas.edu.kg](mailto:journals@manas.edu.kg)

#### PUBLICATION PERIOD

Manas Journal of Engineering (MJEN) is published twice year, MJEN is a peer reviewed journal.

**OWNERS** Kyrgyz - Turkish Manas University  
Prof. Dr. Alpaslan CEYLAN  
Prof. Dr. Almaz İBRAEV

**EDITOR** Assoc. Prof. Dr. Rita İSMAİLOVA

**ASSOCIATE EDITOR** Prof. Dr. Mirbek TURDUEV

**FIELD EDITORS** Assoc. Prof. Dr. Rita İSMAİLOVA (Computer Engineering, Information Technology)  
Prof. Dr. Mirbek TURDUEV (Electrical and Electronics Engineering)  
Asist. Prof. Dr. Peyil ESENGUL KIZI (Mathematics, Applied Mathematics)  
Asist. Prof. Dr. Ruslan ADİL AKAI TEGİN (Food Engineering, Microbiology, Chemical Engineering )  
Asist. Prof. Dr. Kubat KEMELOV (Environmental Engineering)

**EDITORIAL BOARD** Prof. Dr. Asylbek KULMYRZAEV (Food industry devices and technologies, physical chemistry of food systems, rheology, fluorescence, infrared and ultrasonic, spectroscopic analysis methods )  
Prof. Dr. Ozgul Salor DURNA (Electrical and Electronics Engineering)  
Prof. Dr. Ebru DURAL (Civil engineering, Mechanics of Solid Bodies, Building Mechanics, Numerical Modeling)  
Prof. Dr. Jamila SMANALIEVA (Food technology, Food sciences)  
Prof. Dr. Mehmet KOBYA (Environmental Engineering)  
Prof. Dr. Ercan ÇELİK (Mathematics, Differential Equations, Integral Equations, Partial Differential Equations, Optimization, Numerical Analysis, Natural Sciences)  
Assoc. Prof. Dr. Rayimbek SULTANOV (Computer Engineering, Information Technology)

**EDITORIAL ASSISTANTS** Asist. Prof. Dr. Peyil ESENGUL KIZI  
Asist. Prof. Dr. Ruslan ADİL AKAI TEGİN  
Kayahan KÜÇÜK  
Yusuf GÜNDÜZ  
Jumagul NURAKUN KYZY

#### CORRESPONDENCE ADDRESS

Kyrgyz Turkish Manas University  
Chyngyz Aitmatov Avenue 56 Bishkek, KYRGYZSTAN  
URL: <http://journals.manas.edu.kg>  
e-mail: [journals@manas.edu.kg](mailto:journals@manas.edu.kg)  
Tel : +996 312 492763- Fax: +996 312 541935



## CONTENT

### Research article

|   |   |                |
|---|---|----------------|
| <i>Samet Turan,<br/>Huseyin Enes<br/>Salman</i>                                     | <i>Tooth Tip Interference and Stress Analysis of High Contact Ratio Spur Gear Pairs Using an Optimized Design Tool</i>                        | <i>157-162</i> |
| <i>Degnechew Genene Demisu</i>  | <i>Extraction of Oil from Azadirachta indica and Moringa stenopetala Seeds and Evaluation of its Physicochemical Properties</i>               | <i>163-176</i> |
| <i>Burak Ođul</i>   | <i>Dynamics of the rational difference equations</i>  | <i>177-184</i> |
| <i>Şeyda Kılıçođlu,<br/>Semra Yurttançıkma</i>                                      | <i>A modelling of the natural logarithm and Mercator series as 5<sup>th</sup>, 6<sup>th</sup>, 7<sup>th</sup> order Bézier curve in plane</i> | <i>185-191</i> |
| <i>İsrafil Okumuş,<br/>Ercan Çelik</i>  | <i>A Modified Key Generation Algorithm to Rebalanced-RSA and RPower-RSA</i>   | <i>192-197</i> |
| <i>Fatih Ramazan İstanbulluguil,<br/>Mustafa Atasever</i>                           | <i>Investigation of growth and survival of some pathogens in koumiss</i>  | <i>198-207</i> |
| <i>Venera Adanova,<br/>Maksat Atagoziev</i>   | <i>Detection and Identification of Stuttering Types Using Siamese Network</i>   | <i>208-214</i> |
| <i>Sevda Esmâ Darama,<br/>Semra Çoruh,<br/>Selim Ceylan,<br/>Elif Hatice Gürkan</i> | <i>Hydrochar Production from Cigarette Butts and Tobacco for Dye Adsorption</i>   | <i>215-223</i> |
| <i>Özgür Önder Karakılınç</i>   | <i>A Study on Controllable Mod Exploiting the Intrinsic Symmetry Breaking of Low-symmetry Photonic Crystals</i>                               | <i>224-235</i> |

# Tooth Tip Interference and Stress Analysis of High Contact Ratio Spur Gear Pairs Using an Optimized Design Tool

Samet Turan<sup>1</sup>, Huseyin Enes Salman<sup>2,\*</sup>

<sup>1</sup> TOBB University of Economics and Technology, Ankara, Türkiye, sametturan@etu.edu.tr, ORCID: 0000-0001-9075-8664

<sup>2</sup> TOBB University of Economics and Technology, Ankara, Türkiye, hsalman@etu.edu.tr, ORCID: 0000-0001-7572-9902

## ABSTRACT

Gears are structural elements that function to transmit power in mechanical systems. The power transmission is carried out by the rolling motion of the teeth pair. The average number of teeth that come into contact while the gears are running is called the contact ratio and this value is generally between 1 and 2 for gears with standard profile. As the number of teeth of the gear increases, the contact ratio may exceed 2, and the gears with a contact ratio greater than 2 are called high contact ratio (HCR) gears. For HCR gears, there is a higher risk of tooth tip interference when compared to the standard gears and they require contact point calculation to avoid interference. In this study, a mathematical tool is developed using MATLAB to analyze and avoid tool tip interference in HCR spur gears. The addendum diameter, dedendum diameter, pressure angle and modulus values are optimized using the developed mathematical tool in order to obtain an HCR geometry with minimal volume and no tip interference. In addition, the spur gear stresses are calculated using the AGMA standards. According to the results, it has been analytically proven that the load carrying capacity of the HCR spur gear is higher than that of the standard gear with the same diameter and volume. The developed optimization tool provided accurate and optimized geometries for the analyzed HCR spur gears.

## ARTICLE INFO

### Research article

Received: 16.12.2022

Accepted: 09.07.2024

### Keywords:

high contact ratio gear,  
optimization,  
tip interference

\*Corresponding author

## 1. Introduction

The contact ratio in spur gears can be defined as the average number of teeth in contact between two meshing gears. In standard spur gears, this ratio is approximately between 1.2 and 1.6, and it is generally desired to be at least 1.3-1.4 for a smooth power transmission [1]. For the high contact ratio (HCR) spur gears, this ratio is between 2 and 3, which is meaning that the number of teeth in contact is at least two. In standard gears, tooth root stress analysis is performed according to a single tooth, but in HCR gears, this analysis is performed by sharing the total load on two teeth.

The contact ratio varies depending on the tooth diameter and pressure angle of the gears. When these values are brought to the desired level, it is possible to increase the contact ratio above 2. However, the increased tooth diameter in HCR gears increases the risk of tip interference. For this reason, a geometric optimization is needed for the HCR gears. The parameters that can be optimized are the module, tooth diameter, tooth root diameter, pressure angle, base diameter, backlash, and profile shift.

In the literature, there are several studies on the geometric optimization and force analysis in HCR gears. In a study

conducted by Özgüven [2], a software is developed for calculating the dynamic forces on teeth and dynamic transmission errors, as well as the dynamic factors for gears and pinions in spur gears. Rackov et al. [3] demonstrated the Generalized Particle Swarm (GPS) optimization process to create an HCR spur gear pair without tooth tip interference or undercut teeth. By increasing tooth number and decreasing pressure angle to fix the maximum gear diameter, Rameshkumar et al. [4] replaced normal contact ratio (NCR) gears with HCR gears in 35-Ton military vehicles. They discovered that this increased load carrying capacity, decreased the noise and vibration, and slightly improved power-to-weight ratio.

Mohanty [5] employed an analytical approach to determine the load distribution in HCR gears. In the stated study an equivalent stiffness is determined using the bending, axial compression and contact stiffness.

Marimuthu and Muthuveerappan [6] performed finite element analysis in order to determine the exact load carrying capacity of an asymmetrical HCR spur gear set. In their study, the effect of backlash and friction between the gears are neglected. It is stated that asymmetrical HCR gears provided an improved load carrying capacity.

In the literature, there are also studies conducted on the design [7], efficiency [8], static and dynamic loading conditions [9], determination the critical loading points [10], nonlinear dynamic analysis [11], and the modification of the gear profiles [12] of HCR gears.

Within the scope of this study, tip interference analysis is performed for HCR gears by rotating the gear in a virtual environment developed in MATLAB. Addendum, dedendum, pressure angle, profile shift and backlash values are optimized by assigning a number of constraints, such as tip interference and sufficient gap between the teeth. In addition to the geometric optimization, the optimized HCR gear pair is compared to a normal contact ratio (NCR) gear pair in terms of the load carrying capacity.

**2. Method**

Spur gears work by rolling the pinion and gear with mutually pairing involute flanks. These involute flanks are formed by the projection of the base diameter of the gears depending on the angle scanned by the end points, as shown in Figure 1.

While evaluating the gear geometries, the formulations specified in the AGMA 913-A98 standard [13] are followed, and firstly, the diameters determining the gear surface are divided into certain intervals from the root diameter of the gear to the tip diameter. Pressure angle and tooth thickness are calculated, and then the involute values of the obtained pressure angles are determined. With the help of the values obtained, the geometric profiles of the gears are optimized by employing a MATLAB code. During the optimization, several boundary values are used such as the contact ratio, the tip interference and the limit value of the top land thickness to prevent case crashing during carburizing of hardened gears. In Figure 2 and Figure 3, the geometric dimensions used for the optimization calculations are summarized for the gear tooth profile and gear root profile, respectively.

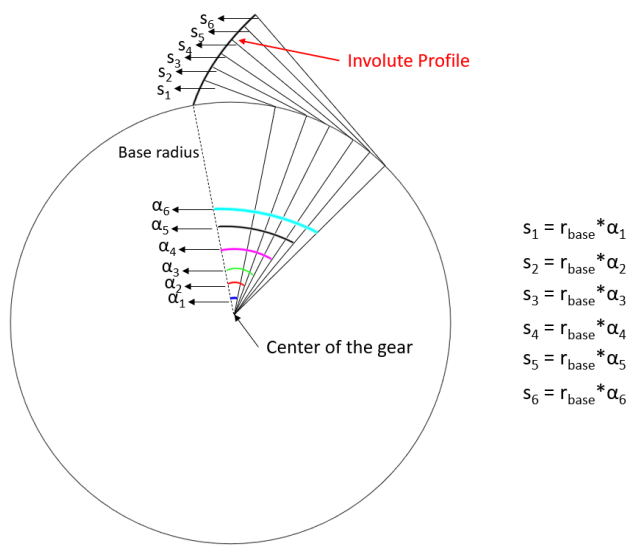


**Figure 1.** The method of involute profile evaluation.

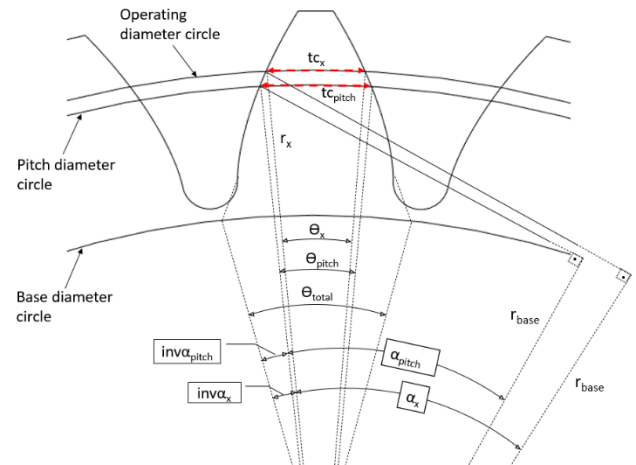


**Figure 2.** Gear tooth profile evaluation.

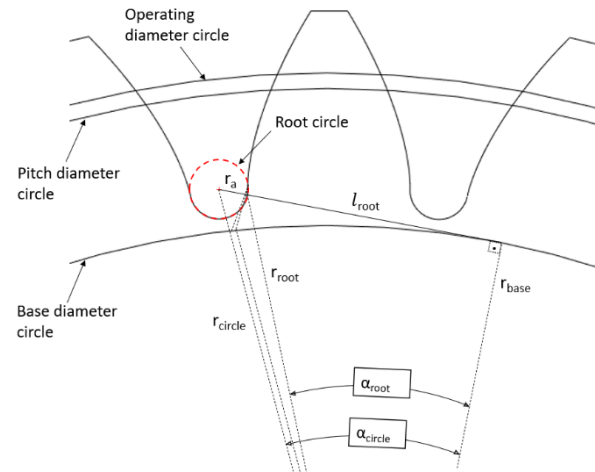


**Figure 3.** Gear root profile evaluation.

**2.1 Constraints**

**2.1.1 Contact ratio**

The contact ratio is usually between 2 and 3 for HCR gears, and this value can be expressed as the ratio of the minimum length between the point of contact where the contact starts and the point where the contact is interrupted to the diametral pitch of the gear in the transverse section. Figure 4 shows the contact points in the transverse section for the opposing pinion and gear.

By the nature of high-contact, the HCR gears transfer the load through the contact of two or three tooth pairs at the same time, and the contact points of the contacting tooth pairs are shown in Figure 4.

Active profile is the region formed by the contact points of the mutually working tooth pairs, and if the contact points are

combined on a line, the resulting line is called line of action (LA).

The point where the first gear contact starts is called SAP (Start of active profile), and from this moment, the two-tooth pair contact starts. This point where the gears contact is called SFTC (Start of first tooth contact).

Meanwhile, the contact of the tooth pair next to the first tooth pair is the second tooth pair that is in contact. This second contact point is called SSTC (Start of second tooth contact). The load transfer is provided by these two tooth pairs for a certain period of time. Then, the third pair of teeth ends the contact and then the first pair of teeth comes out of the contact. This point is shown by ESTC (End of second tooth contact) in Figure 4.

The third pair of teeth, whose contact ends, are separated at the EAP (End of active profile), where the active profile and the contact area end. The parameter of  $p_b$  which is illustrated in Figure 4 represents the base pitch and corresponds to the linear length between two adjacent teeth. The ratio of line of action to base pitch is called contact ratio.

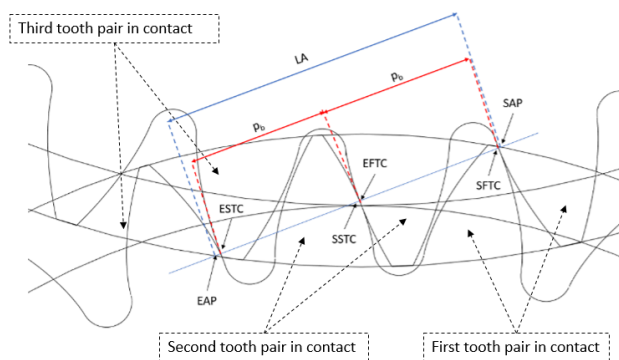


**Figure 4.** Line of action of the HCR gear pair.

Detailed equations on how to formulate the contact ratio can be found in the AGMA 913 A-98 standard [13]. As can be seen from the formulations, the factors that increase or decrease the contact ratio of the gear pair are the diameter of the addendum and the pressure angle of the gear. Dedendum diameter can be used as a factor if the gear is undercut or tip interference does not occur, and it does not directly affect the calculation of the coupling ratio.

### 2.1.2 Interference

In order to obtain an HCR gear, tooth diameter should be increased and the pressure angle should be reduced. This means that HCR gears in the same module have thinner and longer teeth than NCR gears, which is increasing the possibility of end interference. There must be a continuous clearance between the tip diameter of the pinion gear and the root diameter of the gear during the operation of the gear pair. This situation is shown in Figure 5.

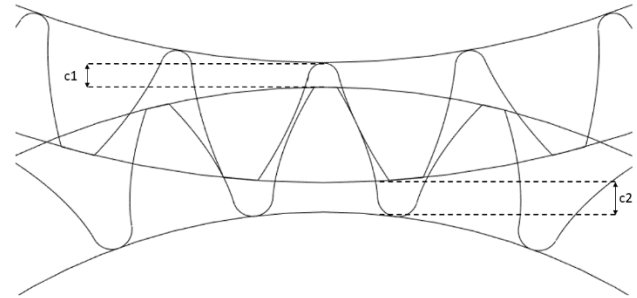


**Figure 5.** Tip-root clearance between pinion and gear.

Theoretically,  $c1$  and  $c2$  clearance values specified in Figure 5 are sufficient for tip-root interference, but in cases where real situations are considered, this value should be determined by considering manufacturing tolerances. In addition to the tip-root interference, the tip-flank interference is also one of the issues to be considered, and in this study, the efforts are mainly performed to prevent this situation.

A number of numerical implementations are carried out in the MATLAB code by gradually increasing the angle scanned by the gear until it enters and exits the contact region. The points with high risk of interference are determined. After performing iterations, an optimal gear geometry with no interference is presented to the user.

Figure 6 shows the condition with a high probability of tooth tip-involute face interference. Several improvements have been performed to prevent tip-face interference, considering backlash enhancement, tooth thinning, profile shifting, root modification and root crown. In this study, the interference is specifically prevented by using backlash boost and profile shift.

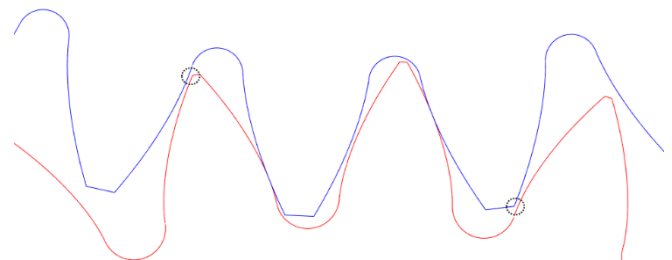


**Figure 6.** Tooth tip-Involute face interference point.

### 2.1.3 Top land thickness

Top land thickness is a critical factor for smooth load transfer, especially for spur gears with hardened surfaces used in aviation industry. Increasing the case hardness values of the surfaces is a method of obtaining high allowable stress values and is carried out by absorbing carbon from the surface in special furnaces. If the top land thickness is lower than the required case hardness depth, a case crash occurs and a highly brittle region is formed at the tip of the gear, which is

increasing the risk of crack formation and the failure of the gear. Figure 7 shows a case with cracked gear in top land.

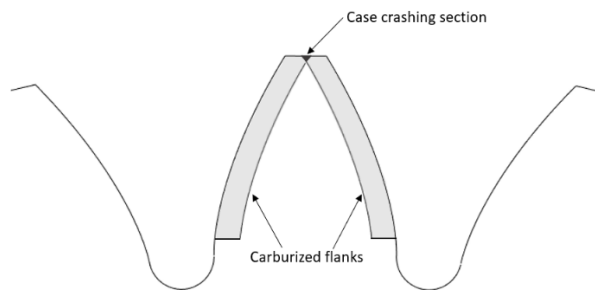


**Figure 7.** Case hardness crash at the top land.

There are a few methods that can be applied to prevent case crash in the top land region. For example, applying a copper plating process to top land can reduce the case hardness depth or increase the top land thickness. Compared to other processes, increasing the top land thickness is a method that does not require heat treatment and prevents case crash at the design stage of the gear. Figure 8 shows dimensions for the calculation of the top land thickness.

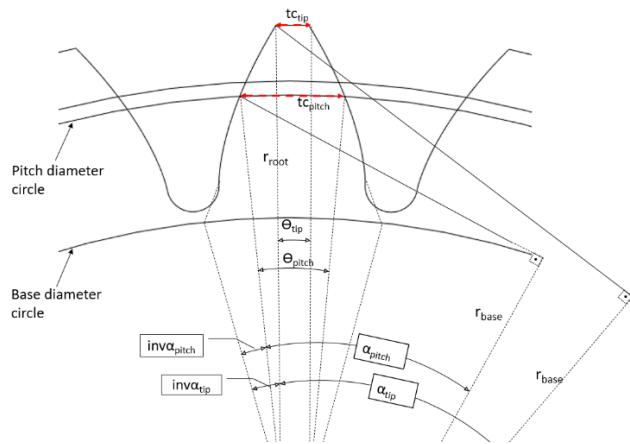


**Figure 8.** Top land thickness evaluation.

### 2.2 Load sharing and stress analysis

With the previously explained design method and boundary conditions, optimization process is carried out with the developed MATLAB code to obtain an HCR gear that would not allow any tip interference. Load distribution analysis is performed on gears meshing simultaneously under the obtained geometry and a sample loading condition. Since the contact ratio in standard gears is between 1 and 2, the load is transferred with a single tooth. As a general approach, the load acts from the HPSTC (Highest point of single tooth contact) point on the tooth as specified in the AGMA standard. By drawing a normal curve to the base diameter of the tooth from this point where the load is acting, a Lewis parabola is formed with the center point of the peak. Then, the load angle and

radius are obtained, and the critical point where the maximum stress will occur is determined. Detailed geometric formulations in the determination process can be obtained from the AGMA 908 B-98 standard [14].

### 3. Results and discussion

The stress on spur gears can be divided into two parts, where one of them is the contact and the other is the bending stress. Contact stress is achieved by using systems such as normal load, speed and lubrication, which are formed on the surface based on the Hertzian contact theory. Bending stress, on the other hand, is the type of stress calculated by using the tangential load and geometrical factors, which are the highest at the critical point at the base of the tooth. The formulations specified in the AGMA 2101-C95 standard [15] is used within the scope of this study while calculating the stress analytically. The distribution of the loads used in the analysis is assumed to be equal for the meshing teeth. The stiffness values of the teeth should be calculated in order to determine the load distribution on the teeth in detail, and it requires other assumptions such as keeping the total normal load constant and the friction coefficient the same in each tooth [5]. Within the scope of this study, it is assumed that the total load will be equally distributed on the 2 meshing gears of the HCR gears. Gear geometry is created using a standard tooth profile, which can be defined as the macro geometry obtained in the HCR gear design and analysis processes specified in the above sections. These processes determine the maximum diameter of the gear by keeping the number of teeth and the module constant. The resulting geometry is analyzed with the same level of load as the load condition on the HCR gear.

For the NCR case, the optimal gear geometry indicated in Figure 9 has been obtained. Afterwards, the optimal HCR geometry is determined for the same diameter of NCR gear pair, as shown in Figure 10. As can be seen in Figure 10, the tooth profile of the optimized HCR gear is significantly different from the optimized NCR gear. The main differences can be summarized as the general curved profile of the tooth, the thickness of the tooth, and the length of the top land region on the top of the tooth. The macro-geometric parameters of the optimized NCR and HCR gears are compared in Table 1. After completing the geometric optimization, the optimized NCR and HCR gear pairs are exposed to the same loading conditions given in Table 2, and critical bending stresses are calculated. According to the results obtained, optimized NCR and HCR pinions are exposed to approximately 675 MPa and 467 MPa, respectively.

With this analytical study, an HCR gear pair is obtained by converting a spur gear pair with a normal contact ratio. During the processes, the number of modules and teeth are preserved, and the load carrying capacity is increased. The main difference of this study from the other HCR studies in the literature is to obtain HCR profile by preserving the number of teeth and diameter, and keeping the transmission ratio constant during increasing the transmitted power capacity in the gearbox.

#### 4. Conclusion

In this study, the tip interference analysis of the HCR gear pair, which has the same values of diameter, module and tooth number as the NCR gear pair, is performed and the necessary pressure angle, addendum and dedendum diameter, backlash and profile shift values are optimized using MATLAB software. Afterwards, the HCR and NCR gears with the same maximum diameter are compared in terms of load carrying capacities, when the maximum bending stress values formed at the tooth base in Table 2 are examined. It has been observed that the bending stress in the HCR gear pair is 30.8% less than the NCR gear pair. This means that the load carrying capacity of the HCR gear with the data given in Table 1 is quite better than the NCR gear.

This theoretical study demonstrates the superiority of the HCR gears in terms of the load carrying capacity. In order to implement this study into the real life, gear manufacturing capabilities need to be further developed compared to today's circumstances, because the gear cutting tools used to create the gear profile need special manufacturing for each case.

There are a few limitations in this study. The allowable stress values used to control the stress levels obtained as a result of contact and stress analysis are taken from the AGMA standard. As a future work, it is necessary to determine experimental allowable stress values with devices such as single tooth bending machines in order to determine more accurate values for the HCR gear pairs. In addition, an equal load distribution is assumed for the contacting teeth pairs. For a more realistic approach, the exact load distribution between the teeth can be determined using finite element analysis and can be verified with experimental measurements on the teeth deformations. Nevertheless, this study provides important results to demonstrate the high capability of the HCR gears and shows directions for an appropriate HCR gear design.

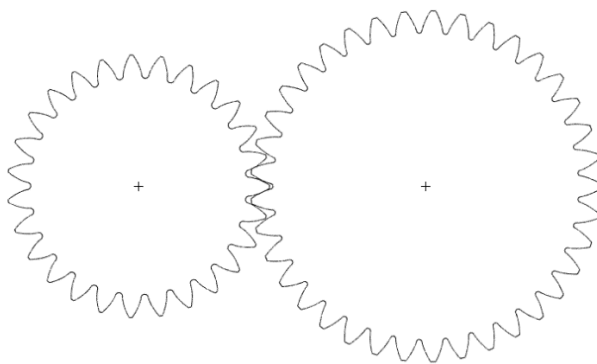


**Figure 9.** Standard gear pair with 27 and 37 teeth, 2.5 mm module, and 25 degrees pressure angle.

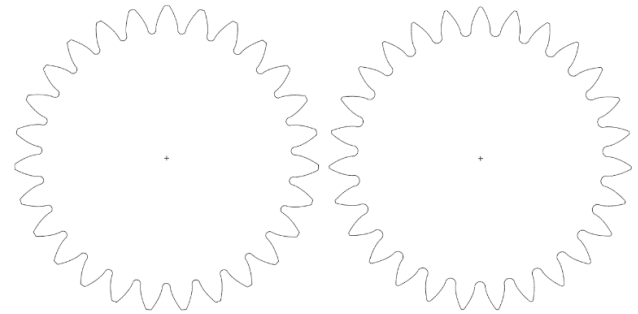


**Figure 10.** NCR (at the left) and HCR (at the right) gear geometry with the data given in Table 1.

**Table 1.** Macro-geometries for HCR and NCR spur gear pairs.

|                           | Macro-geometries |      |               |      |
|---------------------------|------------------|------|---------------|------|
|                           | NCR Gear Pair    |      | HCR Gear Pair |      |
|                           | Pinion           | Gear | Pinion        | Gear |
| Number of teeth           | 27               | 37   | 27            | 37   |
| Module, mm                | 2.5              |      |               |      |
| Addendum coefficient      | 1                |      | 1.35          |      |
| Dedendum coefficient      | 1.25             |      | 1             |      |
| Pressure angle, °         | 25               |      | 21.7          |      |
| Profile shift coefficient | 0.1              | -0.1 | 0.1           | -0.1 |
| Total Backlash, mm        | 0                |      | 0.2           |      |
| Contact Ratio             | 1.48             |      | 2.07          |      |

**Table 2.** Kinematic and stress analyses results of HCR and NCR spur gear pairs for the data given in Table 1.

|                                 | Analysis results |            |
|---------------------------------|------------------|------------|
|                                 | HCR Pinion       | NCR Pinion |
| Load point diameter, mm         | 74.1619          | 67.3694    |
| Pressure angle at load point, ° | 32.2563          | 24.7607    |
| Load angle, °                   | 35.6291          | 23.0419    |
| Critical height, mm             | 5.673            | 2.8685     |
| Critical thickness, mm          | 4.8527           | 5.3839     |
| Transmitted Load, N             | 100              |            |
| Geometry factor                 | 0.0014           | 0.002      |
| Bending stress, MPa             | 467.3758         | 675.278    |

#### References

- [1] Turan S., "Yüksek Kavrama Oranına Sahip Düz Dişli Çiftlerinin Uç-Kök Girişim Analizi ve Yük Taşıma Kapasitesinin Belirlenmesi", Master's Thesis, (2023), TOBB University of Economics and Technology.
- [2] Özgüven H.N., "A non-linear mathematical model for dynamic analysis of spur gears including shaft and

- bearing dynamics”, *Journal of Sound and Vibration*, 145, (1991), 239-260.
- [3] Rackov M., Vers M., Kuzmanovic Z.K., “HCR gearing and optimization of its geometry”, *Advanced Materials Research*, 633, (2013), 117-132.
- [4] Rameshkumar M., Sivakumar P., Sundaresh S., Gopinath K., “Load Sharing Analysis of High-Contact-Ratio Spur Gears in Military Tracked Vehicle Applications”, *Gear Technology*, 1, (2010), 115-126.
- [5] Mohanty S.C., “Tooth load sharing and contact stress analysis of high contact ratio spur gear in mesh”, *Journal of the Institution of Engineers (India), Part MC, Mechanical Engineering Division*, 84, (2003), 66-70.
- [6] Marimuthu P., Muthuveerappan, G., “Investigation of load carrying capacity of asymmetric high contact ratio spur gear based on load sharing using direct gear design approach”, *Mechanism and Machine Theory*, 96, (2016), 52-74.
- [7] Podzharov E., Mozuras A., “Design of high contact ratio spur gears cut with standard tools”, *Gear Technology*, 20, (2003), 34-37.
- [8] Anderson N.E., Loewenthal S.H., “Efficiency of nonstandard and high contact ration involute spur gears”, *Journal of Mechanisms, Transmissions, and Automation in Design*, 108, (1986), 119-126.
- [9] Aydeniz A.İ., “Yüksek kavrama oranının düz alın dişli mekanizmalarında statik ve dinamik davranışa etkileri”, *Doctoral Dissertation*, (2007), Istanbul Technical University.
- [10] Thirumurugan, R., Muthuveerappan, G., “Critical loading points for maximum fillet and contact stresses in normal and high contact ratio spur gears based on load sharing ratio”, *Mechanics Based Design of Structures and Machines*, 39, (2011), 118-141.
- [11] Huang K., Yi Y., Xiong Y., Cheng Z., Chen H., “Nonlinear dynamics analysis of high contact ratio gears system with multiple clearances”, *Journal of the Brazilian Society of Mechanical Sciences and Engineering*, 42, (2020), 98.
- [12] Yildirim N., Gasparini G., Sartori S., “An improvement on helicopter transmission performance through use of high contact ratio spur gears with suitable profile modification design”, *Proceedings of the Institution of Mechanical Engineers, Part G: Journal of Aerospace Engineering*, 222, (2008), 1193-1210.
- [13] AGMA 913 A-98, “Method for specifying the geometry of spur and helical gears”, *American Gear Manufacturers Association*, 1998.
- [14] AGMA 908 B-98, “Geometry factors for determining the pitting resistance and bending strength of spur, helical and herringbone gear teeth”, *American Gear Manufacturers Association*, 1989.
- [15] AGMA 2101-C95, “Fundamental rating factors and calculation methods for involute spur and helical gear (Metric version)”, *American Gear Manufacturers Association*, 1995.

# Extraction of Oil from *Azadirachta indica* and *Moringa stenopetala* Seeds and Evaluation of its Physicochemical Properties

Degnechew Genene Demisu<sup>1,\*</sup>

<sup>1</sup> Forest Products Innovation Center of Excellence, Ethiopian Forest Development, Addis Ababa, Ethiopia, [gdegnecheweth1@gmail.com](mailto:gdegnecheweth1@gmail.com), ORCID: 0000-0002-4412-174X

## ABSTRACT

*Azadirachta indica* and *Moringa stenopetala* trees have been regarded as underutilized, tropical plants, fast-growing, drought-tolerant, robust, oleaginous, and evergreen perennial trees growing widely in various regions of Ethiopia. Almost every part of these plants (i.e., roots, stems, foliage, seeds, and barks) can be used as food additives and as raw materials for pharmaceuticals, cosmetics, soap, and biofuel processing industries. This study aimed at the extraction and characterization of oil from *A. indica* and *M. stenopetala* seeds using the solvent method. The Box-Behnken Design was employed in the experimental design and result analysis. The particle size (0.2, 0.5, 0.8 mm), solvent-to-solute ratio (3:1, 6:1, 9:1), and extraction time (2, 5, 8 hrs) were experimental variables with three levels of low, medium, and high, whereas, the extraction temperature was kept uniform. Seventeen experiments were conducted for each species thereby developing the quadratic models with a  $P$ -value  $< 0.0001$  (significant). The quality and adequacy of the models were evaluated by analysis of variance (ANOVA) at 5% least significant difference. Results of the physicochemical determination of oils were triplicated and obtained as mean  $\pm$  standard deviation. The determined physicochemical properties of *A. indica* and *M. stenopetala* seed oils were kinematic viscosity, specific gravity, pH value, refractive index, acid value, free fatty acid, saponification value, iodine value, and peroxide value. The obtained experimental results showed that the extracted oils from *A. indica* and *M. stenopetala* seeds exhibit good oil quality, and hence, they can be employed for commercial and industrial purposes, and the generation of renewable energy (biofuel).

## ARTICLE INFO

### Research article

Received: 18.10.2023

Accepted: 09.07.2024

### Keywords:

*Azadirachta indica*,  
*Moringa stenopetala*,  
*n*-hexane,  
oil extraction,  
physicochemical properties

\*Corresponding author

## 1. Introduction

*Moringa stenopetala* and *Azadirachta indica* are underutilized species growing in sub-tropical and tropical regions of Ethiopia. These tree species are considered multipurpose plants possessing several economic benefits, like industrial, medicinal, and nutritional values [1 -3]. Almost every part of these non-edible vegetables (i.e., the leaf, stem, bark, roots, and seed) is useful and has a broad range of applications. *Moringa stenopetala* tree offers the benefit of fuel wood, soil and water conservation, livestock forage, medicine, water purification, green manure, and dye and it generates income for farmers and *Moringa* growing enterprises [4 - 6]. On the other hand, *A. indica* (Neem) provides various industrial benefits (i.e., to produce cosmetics, biofuels and to synthesize medicines - Antiseptic, Anti-tuberculosis, Antiviral, Antitumour [2], environmental (i.e., it serves as fixation of dune, reclamation of soil in salinity areas, and organic manure or

organic fertilizer from non-edible Oil cake); and socio-economic benefits such as employment generation, income generation [7].

### *Moringa stenopetala*

*Moringa* is a tropical plant that originates and grows all around the tropics; and belongs to the *Moringaceae* family. The genus *Moringa* comprises fourteen species that cover the sub-tropics and tropical parts of the Earth's surface [3, 5, 8, 9], out of which five *Moringa* species including *Moringa stenopetala*, *Moringa rivae*, *Moringa oleifera*, *Moringa ruspoliana* and *Moringa longitudo* exist in the Northeast tropic of Africa [5]. Among these species, *M. stenopetala* is predominantly found in the southern part of Ethiopia and the Northern part of Kenya; hence, considered an African *Moringa* tree. It has also been domesticated in the lowlands of East Africa, specifically, it is known as an indigenous species to Ethiopia among the

*Moringaceae* family [5, 9, 10]. It covers a wide range of the south-western part of Ethiopia, for instance, Konso, Gamo, Burji, and Gofa people cultivated it as a food crop and consume its leaves as a vegetable [1, 11]. Its English name is known as ‘Cabbage tree’, ‘Ben oil tree’, ‘Africa Moringa tree’, and ‘Horse-radish tree’. In Ethiopia, *M. stenopetala* is known by various vernacular names, such as ‘Haleko’ in Wolaita and Gofa Zones, ‘Shiferaw’ in Amharic and ‘Shelagda’ in Konso areas [4, 10, 12].

*M. stenopetala* is a drought-tolerant, evergreen perennial plant, well-adapted to semi-arid, arid, and poor soil areas with a 500-1,400 mm annual rainfall. It grows naturally in riverine; and can also be cultivated in gardens and terraced fields due to its ease of propagation, multiple usages, and adaptability to degraded and harsh environments [1, 11]. Nonetheless, it does not grow in waterlogged or swampy soils; and it grows best in well-drained soils, with altitude varying from 400 - 2,100 m above sea level and annual temperature varying from 24-30 °C. Its seeds are triangular and covered with a thick, spongy, and yellowish seed coat. The seed kernel has an oval shape and a whitish-grey color (Figure 1). *M. stenopetala* tree can produce up to 4,500 - 10,000 seeds that weigh 2.3-5 kg from about 500-1,000 pods [13]. The *M. stenopetala* seed is a crucial source of oil that can be used for either cooking or various industrial applications, for instance, it is a potential feedstock for the production and utilization of biodiesel [14].



**Figure 1.** Moringa stenopetala Tree, its un-dehulled and dehulled seeds

### Azadirachta indica Tree

The neem tree, *Azadirachta indica*, belongs to the family of *Meliaceae* (*Mahogany*). It is native to regions of the Indian sub-continent and Burma [15]. It is an evergreen perennial tree species found in tropical and subtropical areas of South Asia, Africa, Australia, and America. *A. indica* tree has a broad range of adaptability potential to various topographic and climatic conditions. It is drought-tolerant and grows under humid and semi-arid conditions. The neem tree thrives well on poor soil fertility (i.e., calcareous, dry, and stony soils); and improves the soil conditions [16]. Currently, the tree is cultivated and grown in several countries across the globe (i.e., in Australia, Asia, Africa, and Central, Southern, and Northern parts of America). In Ethiopia, *A. indica* is planted and grown widely in the dry, moist ‘Kolla’ and ‘Weyna Dega’ agro-climatic regions, such as Gambella, Afar, Humara, Metema, Gonder, Kefa, Arsi, Hararge, Illubabor, Shoa, and other regions. It grows in altitudes ranging from 400 - 2,000 m above sea level. It is also a medium-sized and fast-growing tree that can reach over 20-25 m in height with an oval-shaped canopy and a dense leaf. The neem tree begins fruiting in 3-5

years and it becomes fully productive in about 10 years. Based on the climatic conditions and genotype of the plant, a single *A. indica* tree can produce about 30 - 100 kg of fruit annually (Figure 2). The neem seed comprises about 40-46% oil and the remaining part is the matrix of the seed. The neem oil is non-edible, brownish yellow with an unpleasant odor [17, 18]. Thus, neem oil, which is extracted from neem seeds, can be employed for the production of biodiesel, cosmetics, soap, and medicinal products in pharmaceutical industries.



**Figure 2.** *Azadirachta indica* Tree and Seeds

Extraction of oil is a process of obtaining or separating triglycerides from oil-bearing vegetables or animal tissues. This process can be carried out via several extraction techniques or methods while diminishing the alteration of the desired product quality and maximizing the yield of the product. The extraction of oil from non-edible vegetable oils predominantly depends on the part of the plant, for instance, the seed kernel, the pulp, or the foliage [19]. In this study, the Soxhlet extraction method with the solvent n-Hexane is employed. The oil extraction involves a solubility-controlled phase which is a fast physical process that helps to separate oil from the outer surface of the considered particles; and the diffusion-controlled phase which is a relatively slower process enables to obtain oil from the internal part of the subjected particle [20]. Moreover, this process of oil extraction from the oleaginous seed materials (i.e., *A. indica* and *M. stenopetala* seeds) is affected by a number of several operational variables, such as moisture content of the oilseed, particle size, quality of the solvent used, the time allowed for the extraction, the solvent-to-solute ratio, and extraction temperature [21, 22] that in turn affects the quality and the yield of the desired oil [23]. Regardless of the method of extraction to be employed, pre-treatment of the non-edible oilseeds is an indispensable step before extraction. The oilseed pre-treatment step comprises, cleaning, removal of pod or seed coat (de-hulling), winnowing, sorting, and particle size reduction or milling [24, 25]. The removal of moisture content or drying of oilseeds by oven drying is necessitated before grinding proceeds [26]. Size reduction or grinding of the oilseeds (i.e., *A. indica* and *M. stenopetala* seeds) ruptures or breaks the cell embedded in the structure of fiber to increase the surface area of the oil-bearing minute cells for to ensure the release of the desired oil by leaching [27, 28]. The present study aimed at the extraction of oil from *A. indica* and *M. stenopetala* seeds by employing the Soxhlet extraction technique and using n-Hexane as; and determination of physicochemical properties of extracted oils following the standard methods of American Society for Testing Materials (ASTM) and Association of Official Analytical Chemists (AOAC).

## 2. Materials and Methods

### Sample collection and Preparation:

The sample of *A. indica* seed was collected from the Afar Region, district of *Amibara*, which is about 242 km from Addis Ababa, the capital city of Ethiopia, in the Northeastern part. The sample collection area has latitude of 09°15' North, a longitude of 40°10' East, and an altitude of 740m above sea level (a.s.l.). The sample of *M. stenopetala* seed was collected from Sidama Region Agricultural Center, 273 km from Addis Ababa, in the southern part of Ethiopia, with the geographical location of latitude 7° 3' north, longitude 38° 28' east, and altitude of 1,708 m a.s.l. The collected samples were transported to Addis Ababa Institute of Technology, School of Chemical and Bioengineering, laboratory to conduct the experiment. Then, the samples were cleaned and free from foreign materials, such as weed seeds, molds, stones, and other contaminants. Prior to oil extraction, the collected seeds were first de-hulled (i.e., decorticated). Following the decortication, the outer husk was separated from the kernels by winnowing. Then, samples of seed kernel were dried in an oven at 60 °C for 24 hours to remove the moisture content, and drying was continued until the moisture content was below 5% [29].

$$\text{Moisture content [\%]} = \frac{W_0 - W_1}{W_0} * 100 \quad (1)$$

Where,  $W_0$  - initial weight of the sample (before drying);  $W_1$  - final weight of the sample (after drying)

The dried samples of *A. indica* and *M. stenopetala* seed kernels were ground into the paste at the particle sizes, 0.20 mm, 0.50 mm, and 0.80 mm turn-by-turn using grinder to provide a higher surface area of particles for the ease of extraction. The range of desired particle size was obtained through the vibrated sieve shaker. The milling operation ruptured the cell wall and released the solute for direct contact with the solvent during the oil extraction process (i.e., by Soxhlet Extraction Method). The ground samples were put into a Low-Density Polyethylene (LDPE), labeled, and stored until dispatch.

### Experimental Design:

The response surface methodology (RSM), Box-Behnken Design (BBD), was employed in the design of the experiment. The operational variables in the study were particle sizes (A), solvent-to-solute ratio (B), and extraction time (C), with three experimental levels for each variable, low (-1), medium (0), and high (+1) and the yield of oil (%) was the response of the experiment (Table 1). The influence of operational variables on the response was examined along with their interaction effects. A total of 17 experimental runs were carried out with three levels and five central replication points following the BBD method [30]:

$$N = K^2 + K + C_p \quad (2)$$

Where,  $N$ - total experimental runs;  $K$ - number of variables; and  $C_p$ - central replication point

**Table 1-** Experimental levels for the considered factors of study following the BBD method

| Symbols | Levels                  |       |          |            |           |
|---------|-------------------------|-------|----------|------------|-----------|
|         | Variables               | Units | -1 (Low) | 0 (Medium) | +1 (High) |
| A       | Particle size           | mm    | 0.20     | 0.50       | 0.80      |
| B       | Solvent-to-solute ratio | -     | 3        | 6          | 9         |
| C       | Extraction time         | Hrs.  | 2        | 5          | 8         |

The powder of *A. indica* and *M. stenopetala* seeds was obtained turn-by-turn and subjected to an extraction process with various experimental variables including, particle size, solvent-to-solute ratio, and extraction time. The considered particle sizes were 0.20mm, 0.50mm, and 0.80mm; and the solvent-to-solute ratio of 3:1, 6:1, and 9:1, whereas, the extraction time was 2 hrs, 5 hrs, and 8 hrs. In addition, the extraction temperature (°C) and amount of powder sample (g) per run and were allowed to be constant during the experiment (Table 1).

### The Procedure for Oil Extraction Process:

The Soxhlet extraction method, with *n-hexane* as a solvent, was employed for the extraction of oil from the considered species. A 120 g of ground sample was weighed and placed in thimble paper. Then, the thimble paper containing the sample was inserted into the Soxhlet apparatus. A measured solvent (*n-hexane*) at various proportions to solute (3:1, 6:1, and 9:1)

was poured into a 1000 mL round bottom flask and adjusted in the set-up of the extraction vessel. The extraction temperature was kept constant at 72 °C (i.e., slightly higher than the boiling point of the solvent) and the extraction process was continued for 3 hrs, 5 hrs, and 8 hrs to obtain the desired crude oils. As the extraction temperature increased and the process of heating continued, the solvent commenced to evaporate and condensed back to the thimble containing the sample. The solvent was recycled and refluxed back to the flask receiving crude oil and this process was continued until the extraction hour was reached. Then, to recover the solvent from the crude oil-solvent mixture, a rotary evaporator was used at the temperature of about 72 °C. The extraction process was continued until a reasonable amount of crude oil was obtained [31].

### Determination of Physicochemical Properties of Extracted Oil

The physicochemical properties of the extracted oil were determined following the American Society for Testing Materials (ASTM) and Association of Official Analytical Chemists (AOAC). The evaluated properties were acid value and free fatty acid content, saponification value, specific gravity, kinematic viscosity, pH value, iodine value, and refractive index.

#### Determination of acid value and free fatty acid:

The amount of acid number or acid value and free fatty acid (FFA) are used to show the edibility and rancidity of vegetable oils. The acid number indicates the number of milligrams of potassium hydroxide (mg KOH) required to neutralize about 1g of FFA in the given vegetable oil; and the free fatty acid (i.e., usually half of the acid value) is the weight percent of the determined fatty acid like percentage of oleic acid ( $C_{18}H_{34}O_2$ ) in the non-edible vegetable oils [32]. The acid value and free fatty acid determination for *M. stenopetala* and *A. indica* seed oil were conducted according to the standard test method of Association of Official Analytical Chemists (AOAC).

#### Determination of saponification value:

The saponification value of the non-edible vegetable oil is used to indicate the quality, size, and characteristics of chains of fatty acids that can be esterified into glycerol. It also provides the magnitude of the mean length of the fatty acid chain that comprises fat. In amalgamation with an acid number, the saponification value helps to offer information, such as the average weight, amount, and type of glycerides presented in the provided sample of the non-edible vegetable oils [33, 34]. The determination of the saponification value for both samples of crude oils (i.e., *M. stenopetala* and *A. indica* oil) was carried out following the AOAC standard test method [35].

#### Determination of iodine value:

The iodine number or iodine value indicates the mass of iodine (g) that is added to 100 g of the considered sample while measuring the unsaturation levels of the subjected organic compound. The iodine value also shows the number of double bonds that exist in the test samples; and the higher the iodine value presented in the sample, the higher the number of double bonds exists and vice-versa. The iodine value of samples of *M. stenopetala* and *A. indica* seed oil was determined according to the standard test method provided in AOAC [36].

#### Determination of peroxide value:

The peroxide value is a measure of the extent to which the vegetable oils undergo oxidation during the storage and it helps to predict the stability and nature of oils [37]. A high degree of oil unsaturation induces higher peroxide value; and the peroxide value increases with increasing duration of oil contact with atmospheric oxygen, storage temperature, and oil storage time [34] which in turn causes the oxidative rancidity of oil. The determination of peroxide value for each sample (i.e., *M. stenopetala* and *A. indica* oil) was conducted using the standard test method [38].

#### Determination of kinematic viscosity:

Viscosity is a measure of opposition or resistance of flowing fluid (i.e., liquid or gaseous) to a deformation at a provided rate. The viscosity of the non-edible vegetable oil can be expressed in two ways based on the dynamic viscosity ( $\mu$ ) and kinematic viscosity ( $\nu$ ). The dynamic viscosity of vegetable oil is its shear force or resistance to flow because of the internal friction force in the oil molecule. On the other hand, the kinematic viscosity ( $\text{mm}^2/\text{s}$ ) of the oil is its shear force or opposition to flow due to gravity; and this can be determined by dividing the dynamic viscosity of the non-edible vegetable oil by its corresponding density ( $\rho$ ). The dynamic viscosity of each oil sample (i.e., *M. stenopetala* and *A. indica* oil) was determined using the SV- 10 Vibro-viscometer following the standard test method [39]. The volume of the oil sample was kept uniform throughout the measurement and the corresponding dynamic viscosity of each oil sample was recorded at various temperatures (i.e., at 22 °C, 40 °C, and 60 °C) respectively. The required temperature was adjusted by a hot water bath. Then, the kinematic viscosity of the oil sample was computed as follows:

$$\text{Kinematic viscosity } (\nu) = \frac{\text{dynamic viscosity of oil } (\mu)}{\text{density of oil } (\rho)} \quad (3)$$

Where,  $\nu$  ( $\text{mm}^2/\text{s}$ ),  $\mu$  (mPa.s),  $\rho$  ( $\text{kg}/\text{m}^3$ )

#### Determination of pH value:

The pH value of each sample of *M. stenopetala* and *A. indica* oils were determined using the standardized Digital pH meter. Three grams of each oil sample were weighed and added to the dry and clean beaker of 25 ml. Then, hot distilled water of 15 ml was added into a beaker containing the sample and gently stirred, and using the cold water bath, the sample was cooled. A mixture of  $\text{NH}_4\text{OH}$  and  $\text{NH}_4\text{Cl}$  buffer solution was used to standardize the pH electrode. Then, the electrode was immersed into the beaker containing the sample and the corresponding pH value of each oil sample was recorded [27].

#### Determination of specific gravity:

The specific gravity of the non-edible vegetable oils (i.e., *M. stenopetala* and *A. indica* oil) was determined by pycnometer according to the standard test method [40].

#### Determination of refractive index (RI)

The refractive index of oil, usually known as the index of refraction, is the ratio of the velocity of light in a vacuum to the velocity of light in a given non-edible vegetable oil [41]. The longer fatty acid chain in the oil results in a higher refractive index of oil and vice-versa. The refractive index of extracted *M. stenopetala* and *A. indica* seed oil were determined using a digital refracto-meter as per the AOAC standard test method [42].

### 3. Results and discussion

#### Determination of Moisture Content of the collected Seeds:

Determination of the moisture content was conducted for both *M. stenopetala* and *A. indica* seeds based on the dry biomass.

The initial moisture content was carried out using the moisture analyzer and the corresponding results were triplicated and the average percentages of moisture contents were provided below (Table 2).

The average mass per single seed was  $0.48 \pm 0.02$  g and  $0.62 \pm 0.15$  g for *M. stenopetala* and *A. indica* samples, respectively. The obtained initial average moisture content of *M. stenopetala* seed ( $6.48 \pm 0.32\%$ ) was comparable with the 5.70% value of moisture content obtained for *M. oleifera* [43].

To enhance the ease and effectiveness of oil extraction and to avoid challenges of oil water content in the downstream process, the collected samples were dried and pretreated properly. Thus, using the oven, the collected samples were dried continuously until the moisture content was below 5%. After drying, the average moisture contents of *M. stenopetala* and *A. indica* seeds were triplicated and obtained as  $3.12 \pm 0.38\%$  and  $4.34 \pm 0.42\%$ , respectively (Table 2).

**Table 2 - The moisture content of *M. stenopetala* and *A. indica* seeds based on dry biomass (DB)**

| S/N | Experimental samples       | Initial moisture (%) (mean $\pm$ SD) | Final moisture (%) (mean $\pm$ SD) | Average mass per seed (g) (mean $\pm$ SD) |
|-----|----------------------------|--------------------------------------|------------------------------------|---|
| (a) | <i>M. stenopetala</i> seed | 6.48 $\pm$ 0.32                      | 3.12 $\pm$ 0.38                    | 0.48 $\pm$ 0.02                           |
| (b) | <i>A. indica</i> seed      | 11.64 $\pm$ 0.54                     | 4.34 $\pm$ 0.42                    | 0.62 $\pm$ 0.15                           |

*SD – standard deviation*

### The Statistical Evaluation of *A. indica* and *M. stenopetala* Oil Yield Using the RSM:

The experimental results were evaluated and interpreted by employing the RSM, Box-Behnken Design method thereby carrying out the analysis of variance (ANOVA), regression analysis, and coefficients of the determinations for the model equation. The adequacy of the model equation was evaluated

by the results of ANOVA. The regression coefficients ( $R^2$ ), variation coefficients (CV), adjusted coefficients (adj- $R^2$ ), predicted coefficients (Pred- $R^2$ ), and F-test were applied to evaluate the significance and quality of the model equation, where the main comparison was conducted at 5% of the least significant difference (LSD).

**Table 3 - The effects of experimental variables on the yield of *M. stenopetala* and *A. indica* oil**

| Run | Factor A           | Factor B                | Factor C             | Amount of sample per run (g) | Extraction temperature ( $^{\circ}$ C) | Response: yield of oil (%) |                 |                      |                 |
|-----|--------------------|-------------------------|----------------------|------------------------------|--|----------------------------|-----------------|----------------------|-----------------|
|     | Particle size (mm) | Solvent-to-solute ratio | Reaction time (hrs.) |                              |  | <i>M. stenopetala</i> oil  |                 | <i>A. indica</i> oil |                 |
|     |                    |                         |                      |                              |  | Actual value               | Predicted value | Actual value         | Predicted value |
| 1   | 0.50 (0)           | 6:1 (0)                 | 5 (0)                | 120                          | 72                                     | 45.96                      | 45.35           | 44.23                | 42.99           |
| 2   | 0.20 (-1)          | 3:1 (-1)                | 5 (0)                | 120                          | 72                                     | 39.24                      | 38.68           | 36.18                | 35.43           |
| 3   | 0.80 (+1)          | 3:1 (-1)                | 5 (0)                | 120                          | 72                                     | 37.84                      | 37.54           | 35.32                | 34.91           |
| 4   | 0.50 (0)           | 6:1 (0)                 | 5 (0)                | 120                          | 72                                     | 45.52                      | 45.35           | 42.64                | 42.99           |
| 5   | 0.80 (+1)          | 9:1 (+1)                | 5 (0)                | 120                          | 72                                     | 40.72                      | 41.28           | 37.17                | 37.92           |
| 6   | 0.20 (-1)          | 6:1 (0)                 | 2 (-1)               | 120                          | 72                                     | 30.92                      | 31.51           | 28.12                | 28.83           |
| 7   | 0.50 (0)           | 3:1 (-1)                | 2 (-1)               | 120                          | 72                                     | 30.84                      | 30.81           | 27.51                | 27.55           |
| 8   | 0.80 (+1)          | 6:1 (0)                 | 2 (-1)               | 120                          | 72                                     | 30.62                      | 30.94           | 27.86                | 28.22           |
| 9   | 0.50 (0)           | 9:1 (+1)                | 8 (+1)               | 120                          | 72                                     | 49.48                      | 49.51           | 46.22                | 46.18           |
| 10  | 0.50 (0)           | 9:1 (+1)                | 2 (-1)               | 120                          | 72                                     | 30.78                      | 32.90           | 31.25                | 30.13           |
| 11  | 0.20 (-1)          | 9:1 (+1)                | 5 (0)                | 120                          | 72                                     | 42.72                      | 43.01           | 40.39                | 40.80           |
| 12  | 0.20 (-1)          | 6:1 (0)                 | 8 (+1)               | 120                          | 72                                     | 47.36                      | 47.04           | 44.72                | 44.36           |
| 13  | 0.80 (0)           | 6:1 (0)                 | 8 (+1)               | 120                          | 72                                     | 45.32                      | 44.73           | 42.28                | 41.57           |
| 14  | 0.50 (0)           | 6:1 (0)                 | 5 (0)                | 120                          | 72                                     | 44.82                      | 45.35           | 42.68                | 42.99           |
| 15  | 0.50 (0)           | 6:1 (0)                 | 5 (0)                | 120                          | 72                                     | 45.28                      | 45.35           | 43.28                | 42.99           |
| 16  | 0.50 (0)           | 6:1 (0)                 | 5 (0)                | 120                          | 72                                     | 45.15                      | 45.35           | 42.12                | 42.99           |
| 17  | 0.50 (0)           | 3:1 (-1)                | 8 (+1)               | 120                          | 72                                     | 41.64                      | 43.52           | 39.26                | 40.38           |

**Table 4** - Results of ANOVA for the extracted oils at various experimental variables

| Response   | Yield of <i>M. stenopetala</i> oil |    |             |         |                  |                        |
|--|------------------------------------|----|-------------|---------|------------------|------------------------|
| ANOVA for Response surface quadratic model [partial sum of squares-type III] |                                    |    |             |         |                  |                        |
| Source   | Sum of Squares                     | df | Mean square | F-value | P-value Prob > F |                        |
| <i>Model</i>   | 605.63                             | 9  | 67.29       | 118.19  | < 0.0001         | <i>significant</i>     |
| <i>A- Particle size</i>  | 4.12                               | 1  | 4.12        | 7.23    | 0.0311           |                        |
| <i>B- Solvent-to-solute ratio</i>  | 32.56                              | 1  | 32.56       | 57.19   | 0.0001           |                        |
| <i>C- Extraction time</i>  | 429.83                             | 1  | 429.83      | 754.96  | < 0.0001         |                        |
| <i>AB</i>  | 0.090                              | 1  | 0.090       | 0.16    | 0.7028           |                        |
| <i>AC</i>  | 0.76                               | 1  | 0.76        | 1.33    | 0.2868           |                        |
| <i>BC</i>  | 3.80                               | 1  | 3.80        | 6.68    | 0.0362           |                        |
| <i>A<sup>2</sup></i>   | 35.97                              | 1  | 35.97       | 63.19   | < 0.0001         |                        |
| <i>B<sup>2</sup></i>   | 22.14                              | 1  | 22.14       | 38.88   | 0.0004           |                        |
| <i>C<sup>2</sup></i>   | 63.00                              | 1  | 63.00       | 110.65  | < 0.0001         |                        |
| <i>Residual</i>  | 3.99                               | 7  | 0.57        |         |                  |                        |
| <i>Lack of Fit</i>   | 3.26                               | 3  | 1.09        | 5.98    | 0.0584           | <i>not significant</i> |
| <i>Pure Error</i>  | 0.73                               | 4  | 0.18        |         |                  |                        |
| <i>Cor Total</i>   | 609.62                             | 16 |             |         |                  |                        |

| Response                          | Yield of <i>A. indica</i> oil |    |        |        |          |                        |
|-----------------------------------|-------------------------------|----|--------|--------|----------|------------------------|
| <i>Model</i>                      | 623.22                        | 9  | 69.25  | 61.85  | < 0.0001 | <i>significant</i>     |
| <i>A- Particle size</i>           | 5.75                          | 1  | 5.75   | 5.13   | 0.0579   |                        |
| <i>B- Solvent-to-solute ratio</i> | 35.11                         | 1  | 35.11  | 31.36  | 0.0008   |                        |
| <i>C- Extraction time</i>         | 416.74                        | 1  | 416.74 | 372.20 | < 0.0001 |                        |
| <i>AB</i>                         | 1.39                          | 1  | 1.39   | 1.24   | 0.3016   |                        |
| <i>AC</i>                         | 1.19                          | 1  | 1.19   | 1.06   | 0.3372   |                        |
| <i>BC</i>                         | 2.59                          | 1  | 2.59   | 2.32   | 0.1719   |                        |
| <i>A<sup>2</sup></i>              | 38.40                         | 1  | 38.40  | 34.30  | 0.0006   |                        |
| <i>B<sup>2</sup></i>              | 30.81                         | 1  | 30.81  | 27.52  | 0.0012   |                        |
| <i>C<sup>2</sup></i>              | 75.16                         | 1  | 75.16  | 67.13  | < 0.0001 |                        |
| <i>Residual</i>                   | 7.84                          | 7  | 1.12   |        |          |                        |
| <i>Lack of fit</i>                | 5.24                          | 3  | 1.75   | 2.69   | 0.1815   | <i>not significant</i> |
| <i>Pure error</i>                 | 2.60                          | 4  | 0.65   |        |          |                        |
| <i>Cor total</i>                  | 631.05                        | 16 |        |        |          |                        |

**Table 5** - The model equation for the extracted oils at various factors of study

| Response                                  | Yield of <i>M. stenopetala</i> oil |                   |              |              |                    |                         |
|---|------------------------------------|-------------------|--------------|--------------|--------------------|-------------------------|
| Sequential model sum of squares [Type I ] |                                    |                   |              |              |                    |                         |
| Source                                    | Sum of Squares                     | Degree of freedom | Mean square  | F-value      | P-value Prob>F     |                         |
| <i>Mean vs Total</i>                      | 28758.31                           | 1                 | 28676.31     |              |                    |                         |
| <i>Linear vs Mean</i>                     | 466.51                             | 3                 | 155.50       | 14.13        | 0.0002             |                         |
| <i>2FI vs Linear</i>                      | 4.65                               | 3                 | 1.55         | 0.11         | 0.9511             |                         |
| <b><i>Quadratic vs 2FI</i></b>            | <b>134.47</b>                      | <b>3</b>          | <b>44.82</b> | <b>78.73</b> | <b>&lt; 0.0001</b> | <b><i>Suggested</i></b> |
| <i>Cubic vs Quadratic</i>                 | 3.26                               | 3                 | 1.09         | 5.98         | 0.0584             | <i>Aliased</i>          |
| <i>Residual</i>                           | 0.73                               | 4                 | 0.18         |              |                    |                         |
| <i>Total</i>                              | 29285.92                           | 17                | 1722.70      |              |                    |                         |

| Response                                  | Yield of <i>A. indica</i> oil |  |  |  |  |  |
|---|-------------------------------|--|--|--|--|--|
| Sequential model sum of squares [Type I ] |                               |  |  |  |  |  |

| Source                  | Sum of Squares | Degree of freedom | Mean square  | F-value      | P-value            | Prob>F           |
|-------------------------|----------------|-------------------|--------------|--------------|--------------------|------------------|
| Mean vs Total           | 24947.09       | 1                 | 24947.09     |              |                    |                  |
| Linear vs Mean          | 457.60         | 3                 | 152.53       | 11.43        | 0.0006             |                  |
| 2FI vs Linear           | 4.65           | 3                 | 1.72         | 0.10         | 0.9568             |                  |
| <b>Quadratic vs 2FI</b> | <b>160.45</b>  | <b>3</b>          | <b>53.48</b> | <b>47.77</b> | <b>&lt; 0.0001</b> | <b>Suggested</b> |
| Cubic vs Quadratic      | 5.24           | 3                 | 1.75         | 2.69         | 0.1815             | Aliased          |
| Residual                | 2.60           | 4                 | 0.65         |              |                    |                  |
| Total                   | 29376.56       | 17                | 1728.03      |              |                    |                  |

The amount of *A. indica* and *M. stenopetala* crude oils were recorded at the end of each step of the extraction process and the percentage of extracted oil was determined as follows:

$$\text{Oil yield [\%]} = \frac{\text{mass of crude extracted oil}}{\text{total mass of seed kernel}} * 100 \quad (4)$$

The results showed that the maximum oil yields, 49.48% and 46.22%, were recorded for *M. stenopetala* and *A. indica*, respectively, from the experimental run 9 at the particle size of 0.50mm, solvent-to-solute ratio of 9:1, and extraction time of 8 hrs (Table 3). The minimum oil yield (30.62%) was recorded for *M. stenopetala* from experimental run 8 and (27.51%) oil yield for *A. indica* from experimental run 7.

#### The model equation development and evaluation for the extracted oils

The BBD method and results of ANOVA were employed to develop the model equation and analyze its suitability and significance.

The ANOVA result indicated that the developed model equation for the conducted experiment is significant at the  $P < 0.0001$  signifying a 0.01% probability that the model F-value is large because of noise. The model terms are regarded as significant at  $P < 0.05$ . Hence, for the oil extraction process from *M. stenopetala* seed, the model terms  $A^2$ ,  $B^2$ ,  $C^2$ , BC, A, B, and C are considered significant as their respective  $P$  – value  $< 0.05$ , whereas, the terms AB and AC are not significant terms of the model (Table 4). On the other hand, for the oil extraction process from *A. indica* seed, the model terms  $A^2$ ,  $B^2$ ,  $C^2$ , B, and C are significant at  $P < 0.05$ , whereas, A, AB, AC, and BC are insignificant terms of the model. To improve the quality of the model equation, the insignificant terms would not be counted and hence, removed from the model. Moreover, the model fit summary was analyzed for the conducted experiments and the quadratic equation was selected with the statistically significant terms of the model ( $P < 0.0001$ ), where the model is not aliased (Table 5).

In addition, the adjusted determination coefficients of the developed model equations were in agreement with the prediction coefficients. The value of adequate precision is greater than 4 signifying the adequate signal-to-noise ratio and the desirability of the developed model (Table 6). Therefore, the developed model equations can be used to navigate the design space in the process of oil extraction via solvent method at various operational parameters.

**Table 6** - The measures of model adequacy for the extracted oils

| Adequacy measures  | <i>M. stenopetala</i> oil | <i>A. indica</i> oil |
|--------------------|---------------------------|----------------------|
| Standard deviation | 0.75                      | 1.06                 |
| Mean               | 41.07                     | 38.31                |
| C.V. (%)           | 1.84                      | 2.76                 |
| $R^2$              | 0.9935                    | 0.9876               |
| Adj- $R^2$         | 0.9851                    | 0.9716               |
| Pred- $R^2$        | 0.9126                    | 0.8607               |
| Adeq Precision     | 32.204                    | 22.95                |
| PRESS              | 53.27                     | 87.91                |

C.V.- coefficient of variations,  $R^2$ - determination coefficient, Adj- $R^2$ – adjusted determination coefficient, Pred- $R^2$ – predicted determination coefficient

The determination coefficients ( $R^2$ ) indicated that the estimated 99.35% (*M. stenopetala* oil) and 98.76% (*A. indica* oil) overall variations happened in the responses of the experiment were induced by the experimental variables. In addition, the minimum values of variation coefficients (i.e., the ratio of standard error to mean value of oil yield), signified the experiment was reproducible, reliable, and precise. Hence, the developed model expressions were conceived as reproducible and they can be employed at various factors of study thereby carrying out the oil extraction process [30]:

#### The model equation with coded factors to extract oils according to the BBD method:

$$\begin{aligned} \text{Yield of } M. \text{ stenopetala oil} = & - 2.92*A^2 - 2.29*B^2 - 3.87*C^2 - \\ & 0.15*B - 0.44*A*C + 0.97*B*C \\ & - 0.72*A + 2.02*B + 7.33*C + \\ & 45.35 \end{aligned} \quad (5)$$

$$\begin{aligned} \text{Yield of } A. \text{ indica oil} = & - 3.02*A^2 - 2.70*B^2 - 4.23*C^2 - \\ & 0.59*A*B - 0.54*A*C + \\ & 0.81*B*C - 0.85*A + 2.09*B + \\ & 7.22*C + 42. \end{aligned} \quad (6)$$

The diagnostics case statistics of the extracted oils:

Table 7 - The diagnostics case statistics of the extracted oils

| <i>M. stenopetala</i> seed oil |              |                 |                                 |                                 | <i>A. indica</i> seed oil |                 |                                 |                                 |
|--------------------------------|--------------|-----------------|---------------------------------|---------------------------------|---------------------------|-----------------|---------------------------------|---------------------------------|
| Run order                      | Actual value | Predicted value | Internally Studentized residual | Externally Studentized residual | Actual value              | Predicted value | Internally Studentized residual | Externally Studentized residual |
| 1                              | 45.96        | 45.55           | 0.910                           | 0.897                           | 44.23                     | 42.99           | 1.310                           | 1.396                           |
| 2                              | 39.24        | 38.93           | 1.484                           | 1.660                           | 36.18                     | 35.43           | 1.422                           | 1.562                           |
| 3                              | 37.84        | 37.80           | 0.782                           | 0.758                           | 35.32                     | 34.91           | 0.770                           | 0.745                           |
| 4                              | 45.52        | 45.55           | 0.258                           | 0.240                           | 42.64                     | 42.99           | -0.370                          | -0.346                          |
| 5                              | 40.72        | 41.03           | -1.484                          | -1.660                          | 37.17                     | 37.92           | -1.422                          | -1.562                          |
| 6                              | 30.92        | 30.81           | -1.557                          | -1.783                          | 28.12                     | 28.83           | -1.342                          | -1.442                          |
| 7                              | 30.84        | 30.81           | 0.073                           | 0.068                           | 27.51                     | 27.55           | -0.080                          | -0.074                          |
| 8                              | 30.62        | 30.69           | -0.855                          | -0.836                          | 27.86                     | 28.22           | -0.662                          | -0.662                          |
| 9                              | 49.48        | 49.51           | -0.073                          | -0.068                          | 46.22                     | 46.18           | 0.080                           | 0.074                           |
| 10                             | 30.78        | 30.40           | 2.339                           | 4.630                           | 31.25                     | 30.13           | 2.112                           | 3.247                           |
| 11                             | 42.72        | 42.77           | -0.782                          | -0.758                          | 40.39                     | 40.80           | -0.770                          | -0.745                          |
| 12                             | 47.36        | 47.29           | 0.855                           | 0.836                           | 44.72                     | 44.36           | 0.690                           | 0.662                           |
| 13                             | 45.32        | 44.98           | 1.557                           | 1.783                           | 42.28                     | 41.57           | 1.342                           | 1.442                           |
| 14                             | 45.82        | 45.55           | -0.779                          | -0.755                          | 42.68                     | 42.99           | -0.328                          | -0.306                          |
| 15                             | 45.28        | 45.55           | -0.098                          | -0.098                          | 43.28                     | 42.99           | 0.306                           | 0.286                           |
| 16                             | 45.15        | 45.55           | -0.290                          | -0.271                          | 42.12                     | 42.99           | -0.919                          | -0.908                          |
| 17                             | 41.64        | 42.02           | -2.339                          | -5.499                          | 39.26                     | 40.38           | -2.112                          | -3.247                          |

To evaluate the characteristics of the Model equations and the nature of their statistical distribution, the normal probability versus residual error was used in compliance with the Box-Behnken design and the plots showed that the normal distribution of residual errors in the linear patterns (Figure 3). Hence, in the experimental data distributions, a set of data points in the developed model equation were estimated to be

in a straight line with no sign of abnormality. Moreover, a high correlation coefficients (i.e., close to unity) were obtained from the experimental data indicating that the actual experimental values of oil yield (i.e., *M. stenopetala* and *A. indica* oils) were in agreement with their respective predicted values (Table 7), and a data set fits the model equation properly thereby providing a precise prediction of the desired response or yield of the extracted oils (Figure 3).

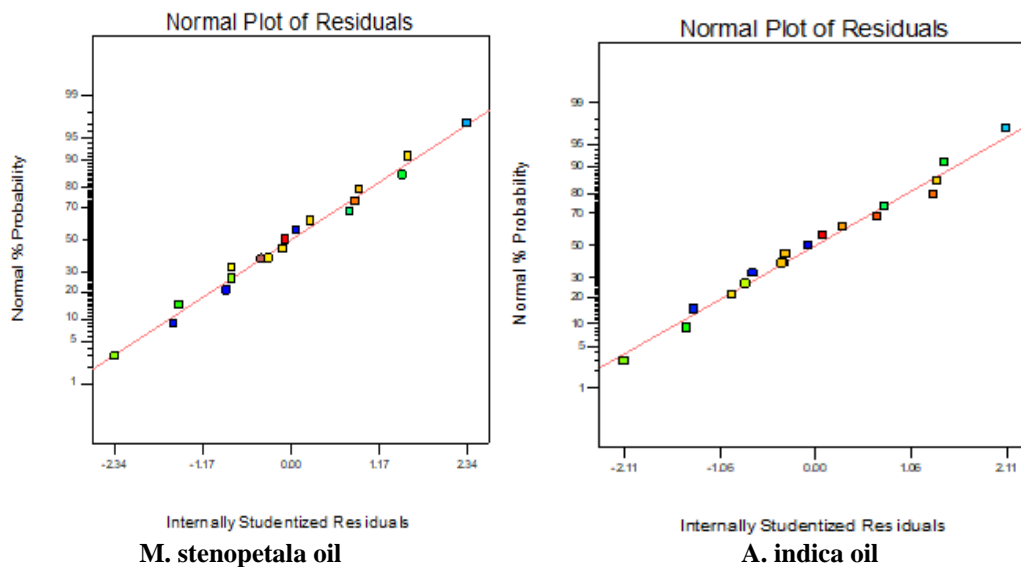


Figure 3. The normal probability versus residual errors plots for *M. stenopetala* and *A. indica* seed oils

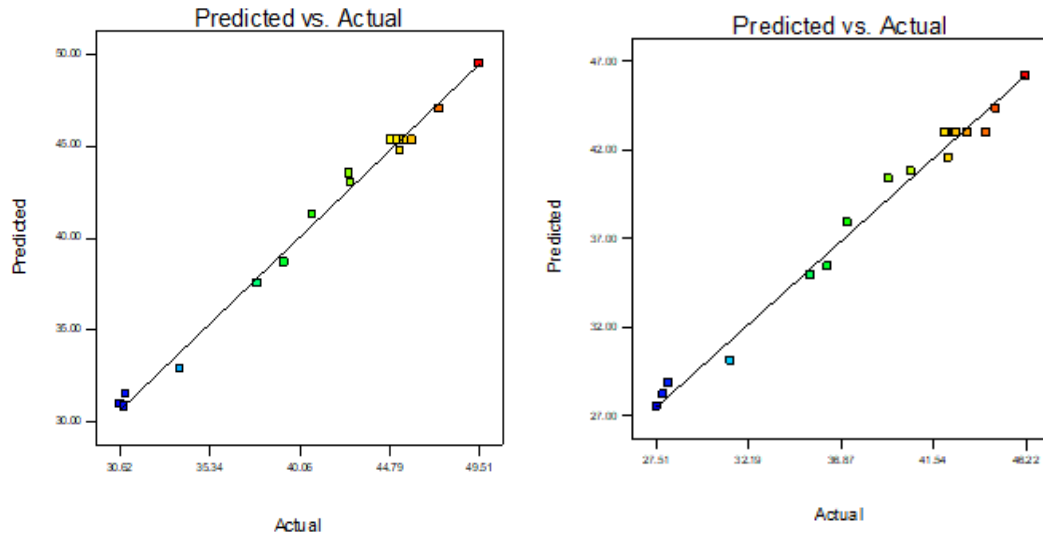


Figure 4. The predicted versus actual value plots for *M. stenopetala* and *A. indica* seed oils

### The Effect of Experimental Variables on the Yield of Oils:

#### The effect of particle size and solvent-to-solute ratio on the yield of oils

The ANOVA results signified that the particle size and solvent-to-solute ratio significantly affect the yield of oils of *M. stenopetala* and *A. indica* with a P- P-value less than 0.05, respectively (Table 4). For instance, the maximum oil yield (49.48%) was obtained for *M. stenopetala* seed when the particle size was 0.5 mm and the solvent-to-solute ratio was 9:1, whereas, the minimum oil yield (30.62%) was recorded at the particle size (0.8 mm) and solvent-to-solute ratio (6:1) with extraction time (2 hrs). Similarly, the maximum *A. indica* oil yield (46.22%) was recorded for the particle size (0.5mm) and solvent-to-solute ratio (9:1) with 8 hrs extraction time, whereas, the minimum oil yield (27.5%) was obtained at the particle size (0.5 mm) and solvent-to-solute ratio (3:1) with an extraction time of 2 hrs (Table 3). For the considered species under experimentation, the maximum and minimum oil yields were obtained by varying the particle size and solvent-to-solute ratio while keeping the extraction time constant (Figure 5). The 3D surface plot of BBD indicated that at uniform extraction time, minimum particle size enhances the oil yield and increasing the solvent-to-solute ratio up to the optimum point enhances the yield of oil and vice-versa. However, using a more solvent-to-solute ratio beyond the optimum level no longer increases the yield of the oil (Figure 5).

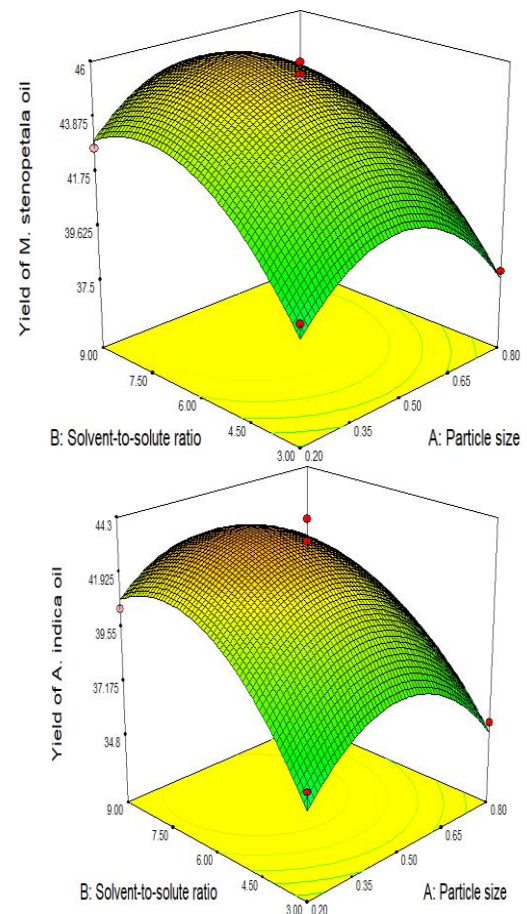
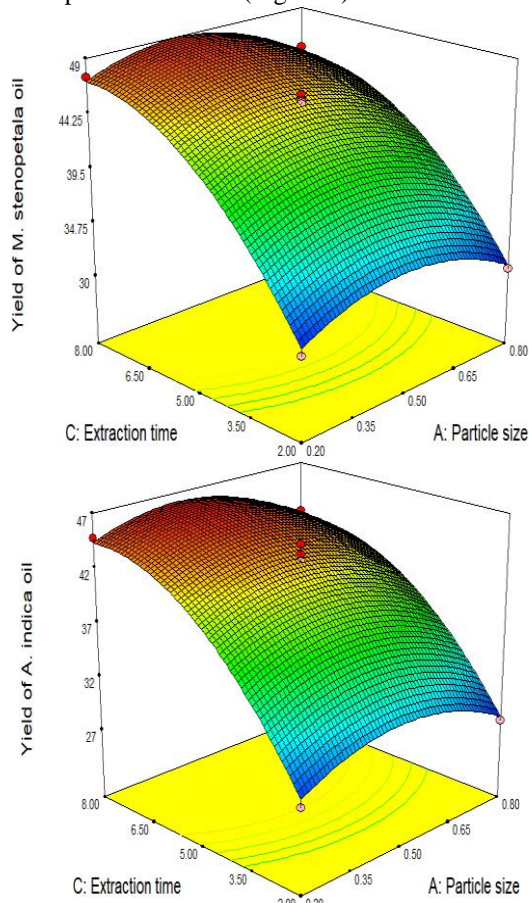


Figure 5. The effect of particle size and solvent-to-solute ratio on the oil yield

### The effect of particle size and extraction time on the oil yield

Results of ANOVA showed that the particle size and extraction time have significant effects on the yield of oil for both species with  $P < 0.05$  (Table 4). The respective maximum and minimum percentages of oil yields were obtained for both species by keeping the solvent-to-solute ratio uniform. Larger particle size and shorter extraction time diminish the oil yield and vice-versa while keeping the solvent-to-solute ratio constant. Increasing the extraction time from 2 - 8 hrs with smaller particle sizes increases the oil yield as shown in the 3D surface plot of the BBD (Figure 6).



**Figure 6.** The effect of particle size and extraction time on the oil yield

### The effect of solvent-to-solute ratio on the oil yield

As presented in the results of ANOVA, the solvent-to-solute ratio and extraction time significantly affect the yield of oil for both species with  $P < 0.05$  (Table 4). The respective maximum and minimum percentages of oil yields were obtained for both

species by keeping the particle size constant. It has been indicated that a more solvent-to-solute ratio and longer extraction time increase the oil yield and vice-versa while keeping the particle size constant. Increasing the extraction time from 2 - 8 hrs with increasing the solvent-to-solute ratio (3:1 - 9:1), increases the oil yield for both *M. stenopetala* and *A. indica* as shown in the 3D surface plot of BBD (Figure 7).

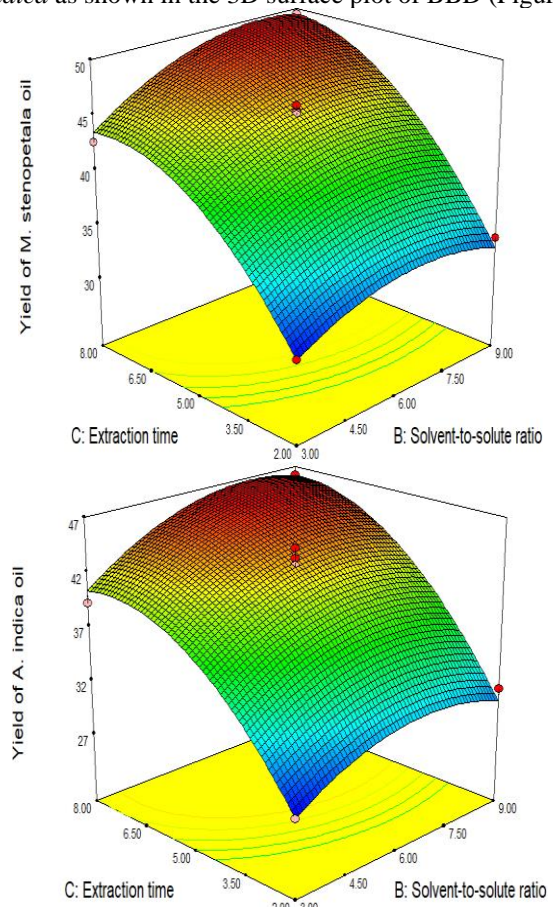


**Figure 7.** The effect of solvent-to-solute ratio and extraction time on the oil yield

### The Physicochemical Properties of Extracted Oil from *M. stenopetala* and *A. indica* Seed:

The physicochemical properties of *M. stenopetala* and *A. indica* seed oil were evaluated according to the standard test methods. The results were triplicated and their corresponding mean values with standard deviation were provided in Table 8. The main physicochemical characteristics of *M. stenopetala* and *A. indica* seed oil were acid value, free fatty acid, saponification value, iodine value, peroxide value, kinematic viscosity, specific gravity, pH value, and refractive index.

**Table 8 - The physicochemical properties of extracted *M. stenopetala* and *A. indica* seed oil**

| Physicochemical properties<br>oil | Units                   | Experimental results<br>(mean±SD) |                      | Standard Methods |      |
|-----------------------------------|-------------------------|-----------------------------------|----------------------|------------------|------|
|                                   |                         | <i>M. stenopetala</i> oil         | <i>A. indica</i> oil |                  |      |
|                                   |                         |                                   |                      |                  |      |
| Kinematic                         | at 22 °C                | mm <sup>2</sup> /s                | 47.73±0.42           | 49.84±0.33       |      |
| Viscosity                         | at 40 °C                | mm <sup>2</sup> /s                | 26.50±0.30           | 28.32±0.42       | [39] |
|                                   | at 60 °C                | mm <sup>2</sup> /s                | 12.30±0.20           | 14.12±0.12       |      |
| Specific gravity                  | -                       | -                                 | 0.89±0.01            | 0.92±0.02        | [40] |
| pH value                          | -                       | -                                 | 7.35±0.05            | 8.26±0.35        | -    |
| Refractive index                  | -                       | -                                 | 1.4132±0.03          | 1.4628±0.02      | [42] |
| Odor                              | -                       | -                                 | Odorless             | Unpleasant       | -    |
| Color                             | -                       | -                                 | Pale yellow          | Brownish-yellow  | -    |
| Acid value                        | mg KOH/g                |                                   | 5.68±0.08            | 18.60±0.64       | [44] |
| Free fatty acid (FFA)             | mg KOH/g                |                                   | 2.84±0.04            | 9.30±0.32        | [44] |
| Saponification value              | mg KOH/g                |                                   | 188.42±0.46          | 194.36±0.54      | [35] |
| Iodine value                      | g I <sub>2</sub> /100 g |                                   | 68.20±0.35           | 72.78±0.36       | [36] |
| Peroxide value                    | meq/kg                  |                                   | 17.12±0.15           | 16.24±0.74       | [38] |

*SD* – standard deviation

It has been found that the acid number of *M. stenopetala* seed oil (5.68±0.08 mg KOH/g oil) was relatively lower than that of *A. indica* seed oil (18.60±0.64 mg KOH/g oil) (Table 8). These values showed that the extracted oil from the two species (i.e., *M. stenopetala* and *A. indica* seeds) could not be subjected to utilization directly, for instance, in the biodiesel production via transesterification process. Thus, they necessitated acid pretreatment steps (i.e., esterification reaction) to convert the free fatty acid in the considered crude oils until their respective FFA values were less than 0.5%.

Moreover, the obtained saponification values of *M. stenopetala* seed oil (188.42±0.46 mg KOH/g oil) and *A. indica* seed oil (194.36±0.54 mg KOH/g oil) were of high value signifying that high free fatty acid (FFA) was presented in each extracted crude oils (Table 8). The result indicated that the obtained saponification value of *M. stenopetala* seed oil was in agreement with the reported values in the previous work, 186 mg KOH/g saponification value of oil was reported by Anwar *et al.*, [45] and 178.23 mg KOH/g by Andinet *et al.*, [14], whereas, the obtained saponification value of *A. indica* seed oil (194.36±0.54 mg KOH/g oil) was in comparable with the previous value, 199.810±1.584 mg KOH/g oil, reported by Bakari *et al.*, [46], for the sample of *A. indica* seed oil collected from Zidim, Cameroon.

The iodine number indicates the degree of unsaturation of oils. The lower iodine value of the oil signifies the lower degree of unsaturation and vice-versa. The experimental result showed that the iodine number of *M. stenopetala* seed oil was 68.20±0.35 g I<sub>2</sub>/100 g oil (Table 8). The obtained value of iodine number was relatively lower and hence, it showed that the *M. stenopetala* seed oil was less likely susceptible to oil rancidity. The result was also in agreement with the report of the previous study, 69 g I<sub>2</sub>/100 g oil by Andinet *et al.*, ([14], 2010) and 65.8 g I<sub>2</sub>/100 g oil by Lalas *et al.*, [47]. Besides, the obtained value of iodine number for the *A. indica* seed oil was 72.78±0.36 g I<sub>2</sub>/100 g oil. This value was in line with the

previously reported result, 74.448±0.564 g I<sub>2</sub>/100 g oil and 73.814±0.366 g I<sub>2</sub>/100 g oil in *A. indica* seed oil collected from the districts of Maroua and Zidim, Cameroon, respectively [46]. On the other hand, the peroxide number determines the amount of hydro-peroxides presented in the crude extracted vegetable oil [48]. The crude oil with lower number of peroxide is highly resistant to oxidation reaction. The peroxide value of *M. stenopetala* seed oil obtained in this study was 17.12±0.15 meq/kg, and this value was in comparable with a 17.60 meq/kg peroxide value of *M. stenopetala* seed oil obtained from Konso, Ethiopia according to the report by Meseret *et al.*, [49]. The peroxide value of *A. indica* seed oil (16.24±0.74 meq/kg) was less than that of the *M. stenopetala* seed oil signified that the *A. indica* seed oil was more resistant to oxidation than that of *M. stenopetala* seed oil (Table 8).

The kinematic viscosities obtained in experiment were recorded at various temperature (i.e., at 22 °C, 40 °C, and 60 °C) and the corresponding values at each specified temperature were recorded as 47.73±0.42 mm<sup>2</sup>/s, 26.50±0.30 mm<sup>2</sup>/s, and 12.30±0.20 mm<sup>2</sup>/s, respectively, for *M. stenopetala* seed oil, whereas, for the *A. indica* seed oil, the kinematic viscosities were recorded as 49.84±0.33 mm<sup>2</sup>/s, 28.32±0.42 mm<sup>2</sup>/s, and 14.12±0.12 mm<sup>2</sup>/s at 22 °C, 40 °C, and 60 °C, respectively (Table 8). For both crude oil samples, the result showed that the kinematic viscosities were decreased with increasing temperature of oil and vice-versa. The evaluated physicochemical properties of the *M. stenopetala* and *A. indica* seed oils (i.e., kinematic viscosity, specific gravity, and refractive index) were in agreement with the reported values in the previous work. The specific gravity of *M. stenopetala* and *A. indica* seed oil were 0.89 and 0.92, respectively, and these values were in comparable with the previously reported value [50], whereas, the values of refractive index, 1.4132±0.03 and 1.4628±0.02, for *M.*

*stenopetala* and *A. indica* seed oil, respectively (Table 8) were in line with the result shown in the previous study [45].

#### 4. Conclusion

In this study, samples of *A. indica* and *M. stenopetala* seeds were collected from different regions of Ethiopia. The collected seeds were first de-hulled (i.e., decorticated). Following the decortication, the outer husk was separated from the kernels by winnowing. The dried samples of *M. stenopetala* and *A. indica* seed kernels were ground into the paste at particle sizes of 0.20 mm, 0.50 mm, and 0.80 mm turn-by-turn using a grinder thereby providing a higher surface area of particles for the ease of oil extraction and to obtain better oil yield. The Soxhlet extraction method, with *n-hexane*, was employed for the extraction of oil from the considered species. In the extraction process, the maximum oil yield, 49.48% *M. stenopetala* oil, and 46.22% *A. indica* oil were obtained from experimental run 9, with particle size 0.5mm, solvent-to-solute ratio of 9:1, and 8 hrs extraction time. On the other hand, the minimum values of oil yield, 30.62% *M. stenopetala* oil was recorded at the particle size of 0.8 mm, solvent-to-solute ratio of 6:1, and 2 hrs extraction time, whereas, the minimum oil yield for *A. indica* (27.51%) was obtained at the particle size 0.5 mm, 3:1 solvent-to-solute ratio, and extraction time of 2 hrs. The physicochemical properties of the extracted oils were determined following the methods of ASTM and AOAC. The results were triplicated and obtained as mean  $\pm$  standard deviation (Table 8). The determined physicochemical properties of *A. indica* and *M. stenopetala* seed oil were kinematic viscosity, specific gravity, pH value, refractive index, acid value, free fatty acid, saponification value, iodine value, and peroxide value. The results of this study indicated that the extracted oils from the considered species had good oil quality, and therefore, they can be utilized for several applications (i.e., commercial and industrial purposes, and production of biofuels).

#### Acknowledgements

The author is thankful to Addis Ababa Institute of Technology, School of Chemical and Bioengineering, for financial support and providing laboratory facilities during the study. The author is also indebted to all laboratory personnel in the School of Chemical and Bioengineering for their cooperation and fruitful contributions to this work during the experimentation.

**Conflict of Interest:** There is no conflict of interest on the publication and authorship of the Paper.

#### References

- [1]. Bania J., Nath AJ, Das A., Sileshi G., "Integrating *Moringa oleifera* and *Moringa stenopetala* in Agroforestry for Adaptation and Mitigation of Climate Change in Asia and Africa. In: Dagar, J.C., Gupta, S.R., Sileshi, G.W. (eds) Agroforestry for Sustainable

Intensification of Agriculture in Asia and Africa", Sustainability Sciences in Asia and Africa, Springer, Singapore, (2023). [https://doi.org/10.1007/978-981-19-4602-8\\_22](https://doi.org/10.1007/978-981-19-4602-8_22)

- [2]. Kumssa D., Joy E., Young S., Odee D., Ander E., Magare C. *et al.*, "Challenges opportunities for Moringa growers in southern Ethiopia and Kenya", PLoS ONE, 12(11), (2017), e0187651. <https://doi.org/10.1371/journal.pone.0187651>
- [3]. National Research Council, "Lost Crops of Africa, Vol. II, Vegetables", The National Academies Press, Washington, DC., (2006).
- [4]. Yisehak K., Solomon M., Tadelles M., "Contribution of Moringa (*Moringa stenopetala*, Bac.), a Highly Nutritious Vegetable Tree, for Food Security in South Ethiopia: A Review", *Asian Journal of Applied Sciences*, 4, (2011), 477-488. <https://doi.org/10.3923/ajaps.2011.477.488>
- [5]. Jiru D., Sonder K., Alemayehu L., Mekonen Y., Anjulo A., "Leaf yield and Nutritive value of Moringa stenopetala and Moringa Oleifera Accessions: Its potential role in food security in constrained dry farming agroforestry systems", Addis Ababa, Ethiopia, (2006).
- [6]. Melesse A., Tiruneh W., Negesse T., "Effects of feeding Moringa stenopetala leaf meal on nutrient intake and growth performance of Rhode Island Red chicks under Tropical climate", *Tropical and Subtropical Agroecosystems*, 14, (2011), 485-492.
- [7]. Gad N., Sekara A., Abdelhamid M., "The Potential Role of Cobalt and/or Organic Fertilizers in Improving the Growth, Yield, and Nutritional Composition of *Moringa oleifera*," *Agronomy*, 9(12) (2019), 862. <https://doi.org/10.3390/agronomy9120862>
- [8]. Beyene D., "Genetic variation in Moringa stenopetala Germplasm of Ethiopia by using Random Amplified Polymorphic DNA as genetic Marker. Msc. thesis Addis Ababa University, Ethiopia", (2005).
- [9]. Gebregiorgis F., Negesse T., Nurfeta A. Feed intake and utilization in sheep fed graded levels of dried Moringa (*Moringa stenopetala*) leaf as a supplement to Rhodes grass hay", *Tropical Animal Health and Production*, 41, (2011), 1-9.
- [10]. Addis G., Jiru D., Mekonnen Y., Dage E., "Moringa [*Moringa stenopetala* (Bak.f) Cufod]. In Guide to Use and Processing Practices. Addis Ababa, Ethiopia: Horn of Africa Regional Environment Center and Network and Addis Ababa University", (2014).
- [11]. Abuye C., Urga K., Knapp H., Selmar D., Omwega A., Imungi J., Winterhalter P., "A compositional study of *Moringa stenopetala* leaves", *East Afr Med J* 80(5), (2003), 247-252. <https://doi.org/10.4314/eamj.v80i5.8695>.
- [12]. Teketay D., "Edible Wild Plants in Ethiopia," Addis Ababa University Press, Addis Ababa, (2010), 260-262.

- [13]. EIAR, Ethiopian Institute of Agricultural Research, Importance of *Moringa stenopetala*, Addis Ababa", (2003).
- [14]. Andinet E., Araya A., Nigist A., Peter L. "*Moringa stenopetala* seed oil as a potential feedstock for Biodiesel production in Ethiopia, Department of Chemistry, Addis Ababa University", (2010). <https://doi.org/10.1039/b916500b>
- [15]. Vietmeyer N., "Neem: A Tree for Solving Global Problems," National Academy Press, Washington DC, (1992), 1-141.
- [16]. Islas J., Acosta E., G-Buentello Z., Delgado-Gallegos J., Moreno-Treviño M., Escalante B, Moreno-Cuevas J., "An overview of Neem (*Azadirachta indica*) and its potential impact on health", *Journal of Functional Foods*, 74, (2020). <https://doi.org/10.1016/j.jff.2020.104171>
- [17]. Adepoju T., Olawale O, "Optimization and Predictive Capability of RSM Using Controllable Variables in *Azadirachta indica* Oilseeds Extraction Process", *International Journal of Chemistry and Materials Research* 3(1), 2015, 1-10.
- [18]. Elteraifi I., Hassanali A, "Oil and *Azadirachtin* contents of neem (*Azadirachta indica* A. Juss) seed kernels collected from trees growing in different habitats in Sudan", *Int. J. Biol. Chem. Sci* 5(3), (2011), 1063-1072.
- [19]. Baskar G., Kalavathy G., Aiswarya R., Selvakumari I., "Advances in bio-oil extraction from nonedible oilseeds and algal biomass. In *Advances in Eco-Fuels for a Sustainable Environment*; Woodhead Publishing Series in Energy: Cambridge, UK, (2019), 187-210.
- [20]. Mustapa A., Manan Y., Azizi A., Norulaini A., Omar K., "Effects of parameters on yield for sub-critical R134a extraction of palm oil", *J Food Eng*, 95, (2009), 606-616.
- [21]. Chaiklahana R., Chirasuwana N., Lohab V., Bunnage B., "Lipid and fatty acids extraction from the cyanobacterium *Spirulina*. *Science Asia* 34, (2008), 299-305.
- [22]. Siddiquee M., Rohani S., "Lipid extraction and biodiesel production from municipal sewage sludges: A review," *Renewable and Sustainable Energy Reviews*, 15, (2011), 1067-1072.
- [23]. Olaniyan A., "Effect of extraction conditions on the yield and quality of oil from castor bean," *Journal of Cereals and Oilseeds*, 1, (2010), 24-33.
- [24]. Ogunniyi D., "Castor Oil: a vital industrial raw material", *Bio-resource Technology*, 97, (2006), 1086-1091.
- [25]. Yusuf A., Mamza P., Ahmed A., Agunwa U., "Extraction and characterization of castor seed oil from wild *Ricinus communis* L.," *International Journal of Science, Environment and Technology*, 4(5), (2015), 1392-1404.
- [26]. Patel V., Durmanças G., Viswanath L., Maples R., Subong B., "Castor oil: properties, uses and optimization of processing parameters in commercial production. *Lipid Insights*, 9, (2016), 1-12.
- [27]. Akpan U., Jimoh A., Mohammed A., "Extraction, characterization and modification of castor seed oil," *Leonardo Journal of Sciences*, 8, (2006), 43-52.
- [28]. Tayde S., Patnaik M., Bhagt S., Renge V., "Epoxidation of vegetable oils: A review", *International Journal of Advanced Engineering Technology*, 2 (4), (2011), 491-501.
- [29]. Adejumo B., Abayomi D., "Effect of Moisture Content on Some Physical Properties of *Moringa Oleifera* Seed", *Jour. Ag. Vet. Sc*, 1(5), (2012), 12-21.
- [30]. Aslan N., Cebeci Y., "Application of Box-Behnken design and response surface methodology for modeling of some Turkish coals," *Turkish coals. Fuel*, 86, (2007), 90-97. <https://doi.org/10.1016/j.fuel.2006.06.010>
- [31]. Aliyu A., Nwaedozie J., Ahmed A., "Quality Parameters of Biodiesel Produced from Locally Sourced *Moringa oleifera* and *Citrullus colocynthis* L. Seeds Found in Kaduna, Nigeria, *International Research Journal of Pure & Applied Chemistry*, 3(4), (2013), 377-390.
- [32]. Othman O., Ngaasapa F., "Physicochemical characteristics of some imported edible vegetable oils and fat marketed in Dare Salaam", *Tanzania Journal of Natural and Applied Sciences*, 1 (2), (2010), 138-147.
- [33]. Fazal W., Musa K., Mohsan N., Khakemin K., "Comparison of some Physico-chemical properties of different oils available in the local market in Pakistan", *International Journal of Recent Research Aspects*, 2(2), (2015), 93-98.
- [34]. Mohammed I., Ali T., "Physicochemical characteristics of some imported edible vegetable oils in Iraq. *Research Journal of Pharmaceutical, Biological and Chemical Sciences*, 6(5), (2015), 488-494.
- [35]. AOAC, 17<sup>th</sup> edn., "Official Method 920.160-Saponification Number of Oils and Fats/IUPAC 2.202 I.S.I Hand Book of Food Analysis (Part XIII)," (2000).
- [36]. AOAC, 17<sup>th</sup> edn., "Official Method 920.159-Iodine Absorption Number of Oils and Fats/I.S.I Hand Book of Food Analysis Part-III", (2000).
- [37]. Nangbes J., Nvau J., Buba W., Zukdimma A., "Extraction and characterization of castor (*Ricinus Communis*) seed oil", *The International Journal of Engineering and Science*, 2(9), (2013), 105-109.
- [38]. AOAC, 17<sup>th</sup> edn., "Official Method 965.33 Peroxide value in oils and fats/Pearson's composition and analysis of food," (2000), pp. 641.
- [39]. ASTM D445., "American Society for Testing Materials, Standard Test Method for Kinematic Viscosity of Transparent and Opaque Liquids (and Calculation of Dynamic Viscosity)", (2021).
- [40]. AOAC, 17<sup>th</sup> edn., "Official method 920.212, Specific gravity (Apparent) of Oils, Pycnometer method/I.S.I. Hand book of Food analysis (Part XIII)," (2000), pp. 72.
- [41]. Jack P., Daniel S., Kristin M., Price L., Dean T., "Refractive index and density measurements of peanut

- oil for determining oleic and linoleic acid contents”, *Journal of the American Oil Chemists' Society*, 90, (2013), 199-206. <https://doi.org/10.1007/s11746-012-2153-4>
- [42]. AOAC, 17<sup>th</sup> edn., “Official method 921.08- Index of refraction of oils and fats/I.S.I Handbook of Food analysis (Part XIII)”, (2000), pp. 70.
- [43]. Anwar F., Bhanger M., “Analytical characterization of *Moringa oleifera* seed oil grown in temperate regions of Pakistan,” *J Agric. Food Chem*, 51, (2003), 6558-6563.
- [44]. ISO 660:2020. Animal and vegetable fats and oils - Determination of acid value and acidity, (2020). <https://www.iso.org/standard/44879.html>
- [45]. Anwar F., Zafar S., Rashid U., “Characterization of *Moringa oleifera* seed oil from drought and irrigated regions of Punjab, Pakistan”, *Grasas Aceites*, 57 (2), (2006), 160-168.
- [46]. Bakari H., Ruben Z., Delattre C., Pierre G., Dubessay P., Michaud P., “Influence of Physicochemical Characteristics of Neem Seeds (*Azadirachta indica* A. Juss) on Biodiesel Production”, *Biomolecules*, 10, (2020), 616. <https://doi.org/10.3390/biom10040616>
- [47]. Lalas S., Tsaknis J., Sflomos K., “Characterization of *Moringa stenopetala* seed oil variety “Marigat” from island Kokwa”, *Eur. J. Lipid Sci. Technol*, 105(1), (2003), 23-31.
- [48]. Kapoor I., Singh B., Singh G., De Heluani C., De Lampasona M., Catalan C., “Chemistry and in vitro antioxidant activity of volatile oil and oleoresins of black pepper (*Piper nigrum*),” *J Agric. Food Chem*, 57(12), (2009), 5358-5364.
- [49]. Meseret H., Haile T., Gebremedhin C., Chala G., “Effects of location and extraction solvent on Physicochemical properties of *Moringa stenopetala* seed oil”, *Heliyon*, 5, (2019), e02781.
- [50]. Adegebe A., Larayetan R., Omojuwa T., “Proximate analysis, physicochemical properties and chemical constituents’ characterization of *Moringa Oleifera* (Moringaceae) seed oil using GC-MS analysis. *Am. J. Chem* 6 (2), (2016), 23-28.

## Dynamics of the rational difference equations

Burak Oğul<sup>1\*</sup>

<sup>1</sup> Department of Management Informations Systems, Faculty of Applied Sciences, Istanbul Aydin University, Istanbul 34295, Turkey, burakogul@aydin.edu.tr, ORCID: 0000-0002-3264-4340

### ABSTRACT

Discrete-time systems are sometimes used to explain natural phenomena that happen in non-linear sciences. We study the periodicity, boundedness, oscillation, stability, and certain exact solutions of nonlinear difference equations of generalized order in this paper. Using the standard iteration method, exact solutions are obtained. Some well-known theorems are used to test the stability of the equilibrium points. Some numerical examples are also provided to confirm the theoretical work's validity. The numerical component is implemented with Wolfram Mathematica. The method presented may be simply applied to other rational recursive issues. In this research, we examine the qualitative behavior of rational recursive sequences provided that the initial conditions are arbitrary real numbers. We examine the behavior of solutions on graphs according to the state of their initial value

$$x_{n+1} = \frac{x_n x_{n-8}}{\pm x_{n-7} \pm x_n x_{n-7} x_{n-8}}, \quad n \in \mathbb{N}_0.$$

### ARTICLE INFO

#### Research article

Received: 16.01.2024

Accepted: 14.10.2024

**Keywords:** Equilibrium point, solution of difference equation, stability, boundedness, global asymptotic stability

\*Corresponding author

### 1. Introduction

Differential equations are often used to describe some natural phenomena when the time is continuous. However, some real life problems can be simply investigated using discrete-time equations. Differential equations occur naturally in many nonlinear sciences, including ecology and economics. In such cases, the state of a phenomenon at a specific point in time completely predicts its state after a year. Dynamical systems theory is useful in discussing the behavior of some models without solving them. Most natural phenomena are studied using difference equations. For instance, recursive equations have been well used in modeling some natural phenomena such as the size of a population, the Fibonacci sequence, the drug in the blood system, the transmission of information, the pricing of a certain commodity, the propagation of annual plants, and others [12]. In addition, some scholars have used differ-

ence equations to find the numerical solutions of some differential equations. More specifically, discretizing a given differential equation gives a difference equation. For example, Runge-Kutta scheme is obtained from discretizing a first order differential equation. This raises the question of the convergence of the difference scheme to the solution of a differential equation. Or, in a broader sense, the question of the correspondence between the properties of solutions of differential equations and their difference approximations. The work [17] is devoted to questions of conservation of a solution bounded on the entire axis in the transition from differential to difference equations and vice versa. In [18], similar questions were considered to preserve the oscillatory property of solutions to second-order equations. The development of technology has motivated the use of recurrence equations as approximations to partial differential equations.

It is worth mentioning that fractional order difference equations are often utilized to investigate some real life phenomena emerging in nonlinear sciences.

Alayachi et al. [5] analyzed the local and global attractivity, periodicity and the solutions of a sixth order difference equation. Some numerical examples have been also presented in [5]. In [28], Sanbo and Elsayed presented the periodicity, stability and some solutions of a fifth order recursive equation. Almatrafi and Alzubaidi [8] discussed the dynamical behaviors of an eighth order difference relation and showed some 2D figures for the obtained results. Moreover, Ahmed et al. [2], found new solutions and investigated the dynamical analysis for some nonlinear difference relations of fifteenth order. More discussions about nonlinear recursive problems can be seen in refs. [1–30].

Let  $I$  be some interval of real numbers and let

$$f : I^{k+1} \rightarrow I,$$

be a continuously differentiable function. Then for every set of initial conditions

$$x_{-k}, x_{-k+1}, \dots, x_0 \in I$$

the difference equation

$$x_{n+1} = f(x_n, x_{n-1}, \dots, x_{n-k}), \quad (1)$$

has a unique solution  $\{x_n\}_{n=-k}^\infty$  [23]. A point  $\bar{x} \in I$  is called an equilibrium point of equation (1) if

$$\bar{x} = f(\bar{x}, \bar{x}, \dots, \bar{x}).$$

That is,  $x_n = \bar{x}$  for  $n \geq 0$  is a solution of equation (1), or equivalently,  $\bar{x}$  is a fixed point of  $f$ .

**Definition 1.1.** (Stability).

- (i) The equilibrium point  $\bar{x}$  of equation (1) is called locally stable if for every  $\epsilon > 0$ , there exists  $\delta > 0$  such that for all

$$x_{-k}, x_{-k+1}, \dots, x_{-1}, x_0 \in I,$$

with

$$|x_{-k} - \bar{x}| + |x_{-k+1} - \bar{x}| + \dots + |x_0 - \bar{x}| < \delta,$$

we have

$$|x_n - \bar{x}| < \epsilon \quad \text{for all } n \geq k.$$

- (ii) The equilibrium point  $\bar{x}$  of equation (1) is called locally asymptotically stable if  $\bar{x}$  is a locally stable solution of equation (1) and there exists  $\gamma > 0$ , such that for all

$$x_{-k}, x_{-k+1}, \dots, x_{-1}, x_0 \in I,$$

with

$$|x_{-k} - \bar{x}| + |x_{-k+1} - \bar{x}| + \dots + |x_0 - \bar{x}| < \gamma,$$

we have

$$\lim_{n \rightarrow \infty} x_n = \bar{x}.$$

The equilibrium point  $\bar{x}$  of equation (1) is called a global attractor if for all

$$x_{-k}, x_{-k+1}, \dots, x_{-1}, x_0 \in I,$$

we have

$$\lim_{n \rightarrow \infty} x_n = \bar{x}.$$

- (iv) The equilibrium point  $\bar{x}$  of equation (1) is called a global asymptotically stable if  $\bar{x}$  is locally stable and  $\bar{x}$  is also a global attractor of equation (1).

- (v) The equilibrium point  $\bar{x}$  of equation (1) is called unstable if  $\bar{x}$  is not locally stable. The linearized equation of equation (1) about the equilibrium  $\bar{x}$  is the linear difference equation

$$y_{n+1} = \sum_{i=0}^k \frac{\partial f(\bar{x}, \bar{U}, \dots, \bar{x})}{\partial x_{n-i}} y_{n-i}.$$

**Theorem 1.** (see[21]). Assume that  $p, q \in \mathbb{R}$  and  $k \in \mathbb{N}_0$ . Then

$$|p| + |q| < 1$$

is a sufficient condition for the asymptotic stability of the difference equation

$$x_{n+1} + px_n + qx_{n-k} = 0, \quad n \in \mathbb{N}_0.$$

**Remark 2.** Theorem 1 can be easily extended to general linear equations of the form

$$x_{n+k} + p_1x_{n+k-1} + \dots + p_kx_n = 0, \quad n \in \mathbb{N}_0, \quad (2)$$

where,  $p_1, p_2, \dots, p_k \in \mathbb{R}$  and  $k \in \mathbb{N}$ . Then (2) is asymptotically stable provided that

$$\sum_{i=1}^k |p_i| < 1.$$

**Definition 1.2.** (Periodicity). A sequence  $\{x_n\}_{n=-k}^\infty$  is said to be periodic with period  $p$  if  $x_{n+p} = x_n$  for all  $n \geq -k$ .

**Definition 1.3.** The equilibrium point  $\bar{x}$  is said to be hyperbolic if  $|f'(\bar{x})| \neq 1$ . If  $|f'(\bar{x})| = 1$ ,  $x$  is non hyperbolic.

**2. The Difference Equation**  $x_{n+1} = \frac{x_n x_{n-8}}{x_{n-7} + x_n x_{n-7} x_{n-8}}$

In this part we give the solutions of

$$x_{n+1} = \frac{x_n x_{n-8}}{x_{n-7} + x_n x_{n-7} x_{n-8}}, \quad n \in \mathbb{N}_0, \quad (3)$$

where the initials are arbitrary real numbers.

**Theorem 3.** Let  $\{x_n\}_{n=-8}^\infty$  be a solution of Eq. 3. Then for  $n \in \mathbb{N}_0$

$$\begin{aligned} x_{16n+1} &= \frac{aj \prod_{i=0}^{n-1} (1 + (16i + 9)aj)}{h \prod_{i=0}^n (1 + (16i + 1)aj)}, \\ x_{16n+2} &= \frac{aj \prod_{i=0}^{n-1} (1 + (16i + 10)aj)}{g \prod_{i=0}^n (1 + (16i + 2)aj)}, \\ x_{16n+3} &= \frac{aj \prod_{i=0}^{n-1} (1 + (16i + 11)aj)}{f \prod_{i=0}^n (1 + (16i + 3)aj)}, \\ x_{16n+4} &= \frac{aj \prod_{i=0}^{n-1} (1 + (16i + 12)aj)}{e \prod_{i=0}^n (1 + (16i + 4)aj)}, \\ x_{16n+5} &= \frac{aj \prod_{i=0}^{n-1} (1 + (16i + 13)aj)}{d \prod_{i=0}^n (1 + (16i + 5)aj)}, \\ x_{16n+6} &= \frac{aj \prod_{i=0}^{n-1} (1 + (16i + 14)aj)}{c \prod_{i=0}^n (1 + (16i + 6)aj)}, \\ x_{16n+7} &= \frac{aj \prod_{i=0}^{n-1} (1 + (16i + 15)aj)}{b \prod_{i=0}^n (1 + (16i + 7)aj)}, \\ x_{16n+8} &= \frac{j \prod_{i=0}^{n-1} (1 + (16i + 16)aj)}{\prod_{i=0}^n (1 + (16i + 8)aj)}, \\ x_{16n+9} &= \frac{h \prod_{i=0}^n (1 + (16i + 1)aj)}{\prod_{i=0}^n (1 + (16i + 9)aj)}, \\ x_{16n+10} &= \frac{g \prod_{i=0}^n (1 + (16i + 2)aj)}{\prod_{i=0}^n (1 + (16i + 10)aj)}, \\ x_{16n+11} &= \frac{f \prod_{i=0}^n (1 + (16i + 3)aj)}{\prod_{i=0}^n (1 + (16i + 11)aj)}, \\ x_{16n+12} &= \frac{e \prod_{i=0}^n (1 + (16i + 4)aj)}{\prod_{i=0}^n (1 + (16i + 12)aj)}, \\ x_{16n+13} &= \frac{d \prod_{i=0}^n (1 + (16i + 5)aj)}{\prod_{i=0}^n (1 + (16i + 13)aj)}, \\ x_{16n+14} &= \frac{c \prod_{i=0}^n (1 + (16i + 6)aj)}{\prod_{i=0}^n (1 + (16i + 14)aj)}, \\ x_{16n+15} &= \frac{b \prod_{i=0}^n (1 + (16i + 7)aj)}{\prod_{i=0}^n (1 + (16i + 15)aj)}, \\ x_{16n+16} &= \frac{a \prod_{i=0}^n (1 + (16i + 8)aj)}{\prod_{i=0}^n (1 + (16i + 16)aj)}. \end{aligned}$$

where,

$$\begin{aligned} x_{-8} &= j, & x_{-7} &= h, & x_{-6} &= g, & x_{-5} &= f, \\ x_{-4} &= e, & x_{-3} &= d, & x_{-2} &= c, & x_{-1} &= b, \\ x_0 &= a. \end{aligned} \quad (4)$$

**Proof** Suppose that  $n > 0$  and that our assumption holds for  $n - 1$ . That is,

$$\begin{aligned} x_{16n-15} &= \frac{aj \prod_{i=0}^{n-2} (1 + (16i + 9)aj)}{h \prod_{i=0}^{n-1} (1 + (16i + 1)aj)}, \\ x_{16n-14} &= \frac{aj \prod_{i=0}^{n-2} (1 + (16i + 10)aj)}{g \prod_{i=0}^{n-1} (1 + (16i + 2)aj)}, \\ x_{16n-13} &= \frac{aj \prod_{i=0}^{n-2} (1 + (16i + 11)aj)}{f \prod_{i=0}^{n-1} (1 + (16i + 3)aj)}, \\ x_{16n-12} &= \frac{aj \prod_{i=0}^{n-2} (1 + (16i + 12)aj)}{e \prod_{i=0}^{n-1} (1 + (16i + 4)aj)}, \\ x_{16n-11} &= \frac{aj \prod_{i=0}^{n-2} (1 + (16i + 13)aj)}{d \prod_{i=0}^{n-1} (1 + (16i + 5)aj)}, \\ x_{16n-10} &= \frac{aj \prod_{i=0}^{n-2} (1 + (16i + 14)aj)}{c \prod_{i=0}^{n-1} (1 + (16i + 6)aj)}, \\ x_{16n-9} &= \frac{aj \prod_{i=0}^{n-2} (1 + (16i + 15)aj)}{b \prod_{i=0}^{n-1} (1 + (16i + 7)aj)}, \\ x_{16n-8} &= \frac{j \prod_{i=0}^{n-2} (1 + (16i + 16)aj)}{\prod_{i=0}^{n-1} (1 + (16i + 8)aj)}, \\ x_{16n-7} &= \frac{h \prod_{i=0}^{n-1} (1 + (16i + 1)aj)}{\prod_{i=0}^{n-1} (1 + (16i + 9)aj)}, \\ x_{16n-6} &= \frac{g \prod_{i=0}^{n-1} (1 + (16i + 2)aj)}{\prod_{i=0}^{n-1} (1 + (16i + 10)aj)}, \\ x_{16n-5} &= \frac{f \prod_{i=0}^{n-1} (1 + (16i + 3)aj)}{\prod_{i=0}^{n-1} (1 + (16i + 11)aj)}, \\ x_{16n-4} &= \frac{e \prod_{i=0}^{n-1} (1 + (16i + 4)aj)}{\prod_{i=0}^{n-1} (1 + (16i + 12)aj)}, \\ x_{16n-3} &= \frac{d \prod_{i=0}^{n-1} (1 + (16i + 5)aj)}{\prod_{i=0}^{n-1} (1 + (16i + 13)aj)}, \\ x_{16n-2} &= \frac{c \prod_{i=0}^{n-1} (1 + (16i + 6)aj)}{\prod_{i=0}^{n-1} (1 + (16i + 14)aj)}, \\ x_{16n-1} &= \frac{b \prod_{i=0}^{n-1} (1 + (16i + 7)aj)}{\prod_{i=0}^{n-1} (1 + (16i + 15)aj)}, \\ x_{16n} &= \frac{a \prod_{i=0}^{n-1} (1 + (16i + 8)aj)}{\prod_{i=0}^{n-1} (1 + (16i + 16)aj)}. \end{aligned}$$

where,  $x_{-8}, \dots, x_0$  defines as in 4 Now, it follows from Equation 3 that

$$x_{16n+1} = \frac{x_{16n}x_{16n-8}}{x_{16n-7} + x_{16n}x_{16n-7}x_{16n-8}}. \quad (5)$$

If the found values are substituted in the equation 5, we have

$$x_{16n+1} = \frac{aj \prod_{i=0}^{n-1} (1 + (16i + 9)aj)}{h \prod_{i=0}^n (1 + (16i + 1)aj)}.$$

Other relations can also be obtained in a similar way, and thus the proof is complete.

**Theorem 4.** Equation 3 has a unique equilibrium  $\bar{x} = 0$  and it is not locally asymptotically stable.

**Proof**

We have

$$\bar{x} = \frac{\bar{x}^2}{\bar{x}(1 + \bar{x}^2)}.$$

Then

$$1 + \bar{x}^2 = 1, \quad \bar{x}^2 = 0.$$

Thus the equilibrium of Equation 3 is  $\bar{x} = 0$ .

Define the function  $F$  by

$$F(\alpha, \beta, \gamma) = \frac{\alpha\gamma}{\beta(1 + \alpha\gamma)}.$$

Then it follows that,

$$F_\alpha(\alpha, \beta, \gamma) = \frac{\gamma}{\beta(1 + \alpha\gamma)^2}; \quad F_\beta(\alpha, \beta, \gamma) = -\frac{\alpha\gamma}{\beta^2(1 + \alpha\gamma)};$$

$$F_\gamma(\alpha, \beta, \gamma) = \frac{\alpha}{\beta(1 + \alpha\gamma)^2};$$

we see that,

$$F_\alpha(\bar{x}, \bar{x}, \bar{x}) = 1; \quad F_\beta(\bar{x}, \bar{x}, \bar{x}) = -1; \quad F_\gamma(\bar{x}, \bar{x}, \bar{x}) = 1$$

By using Theorem 1, the proof is completed.

**Example 1.** Assume that

$$x_{-8} = 6.5, \quad x_{-7} = 5.5, \quad x_{-6} = 24, \quad x_{-5} = 23, \quad x_{-4} = 22, \\ x_{-3} = 21, \quad x_{-2} = 5, \quad x_{-1} = 4, \quad x_0 = 3.$$

See figure 1.

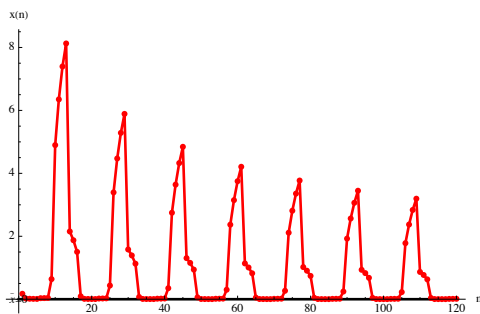


Figure 1

**Example 2.** Assume that,

$$x_{-8} = 7.5, \quad x_{-7} = 3.5, \quad x_{-6} = 20, \quad x_{-5} = 21, \quad x_{-4} = 19, \\ x_{-3} = 18, \quad x_{-2} = 6, \quad x_{-1} = 5, \quad x_0 = 2.5$$

See figure 2.

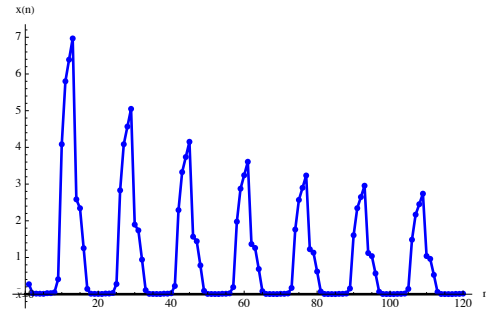


Figure 2

**3. The Equation**  $x_{n+1} = \frac{x_n x_{n-8}}{x_{n-7} - x_n x_{n-7} x_{n-8}}$

We deal with the difference equation

$$x_{n+1} = \frac{x_n x_{n-8}}{x_{n-7} - x_n x_{n-7} x_{n-8}}, \quad n \in \mathbb{N}_0. \quad (6)$$

where the initials are arbitrary real numbers.

**Theorem 5.** Let  $\{x_n\}_{n=-8}^\infty$  be a solution of Equation 6 Then for  $n \in \mathbb{N}_0$

$$x_{16n+1} = \frac{aj \prod_{i=0}^{n-1} (1 - (16i + 9)aj)}{h \prod_{i=0}^n (1 - (16i + 1)aj)}, \\ x_{16n+2} = \frac{aj \prod_{i=0}^{n-1} (1 - (16i + 10)aj)}{g \prod_{i=0}^n (1 - (16i + 2)aj)}, \\ x_{16n+3} = \frac{aj \prod_{i=0}^{n-1} (1 - (16i + 11)aj)}{f \prod_{i=0}^n (1 - (16i + 3)aj)}, \\ x_{16n+4} = \frac{aj \prod_{i=0}^{n-1} (1 - (16i + 12)aj)}{e \prod_{i=0}^n (1 - (16i + 4)aj)}, \\ x_{16n+5} = \frac{aj \prod_{i=0}^{n-1} (1 - (16i + 13)aj)}{d \prod_{i=0}^n (1 - (16i + 5)aj)}, \\ x_{16n+6} = \frac{aj \prod_{i=0}^{n-1} (1 - (16i + 14)aj)}{c \prod_{i=0}^n (1 - (16i + 6)aj)}, \\ x_{16n+7} = \frac{aj \prod_{i=0}^{n-1} (1 - (16i + 15)aj)}{b \prod_{i=0}^n (1 - (16i + 7)aj)}, \\ x_{16n+8} = \frac{j \prod_{i=0}^{n-1} (1 - (16i + 16)aj)}{\prod_{i=0}^n (1 - (16i + 8)aj)},$$

$$\begin{aligned}
 x_{16n+9} &= \frac{h \prod_{i=0}^n (1 - (16i + 1)aj)}{\prod_{i=0}^n (1 - (16i + 9)aj)}, \\
 x_{16n+10} &= \frac{g \prod_{i=0}^n (1 - (16i + 2)aj)}{\prod_{i=0}^n (1 - (16i + 10)aj)}, \\
 x_{16n+11} &= \frac{f \prod_{i=0}^n (1 - (16i + 3)aj)}{\prod_{i=0}^n (1 - (16i + 11)aj)}, \\
 x_{16n+12} &= \frac{e \prod_{i=0}^n (1 - (16i + 4)aj)}{\prod_{i=0}^n (1 - (16i + 12)aj)}, \\
 x_{16n+13} &= \frac{d \prod_{i=0}^n (1 - (16i + 5)aj)}{\prod_{i=0}^n (1 - (16i + 13)aj)}, \\
 x_{16n+14} &= \frac{c \prod_{i=0}^n (1 - (16i + 6)aj)}{\prod_{i=0}^n (1 - (16i + 14)aj)}, \\
 x_{16n+15} &= \frac{b \prod_{i=0}^n (1 - (16i + 7)aj)}{\prod_{i=0}^n (1 - (16i + 15)aj)}, \\
 x_{16n+16} &= \frac{a \prod_{i=0}^n (1 - (16i + 8)aj)}{\prod_{i=0}^n (1 - (16i + 16)aj)}.
 \end{aligned}$$

holds.

**Proof** The proof is similar to the proof of Theorem 3 and therefore it will be omitted.

**Theorem 6.** Equation 6 has a unique equilibrium  $\bar{x} = 0$ , and it is not locally asymptotically stable.

**Proof** The proof is similar to the proof Theorem 4 and there it will be omitted.

For confirming the outcomes of this section, we take into consideration mathematical instances which stand for various kind of solutions to (3).

**Example 3.** The solution in given by Figure 3 when,

$$\begin{aligned}
 x_{-8} = 6, \quad x_{-7} = 6.5, \quad x_{-6} = 11, \quad x_{-5} = 19, \quad x_{-4} = 13, \\
 x_{-3} = 10, \quad x_{-2} = 11, \quad x_{-1} = 8, \quad x_0 = 9.5
 \end{aligned}$$

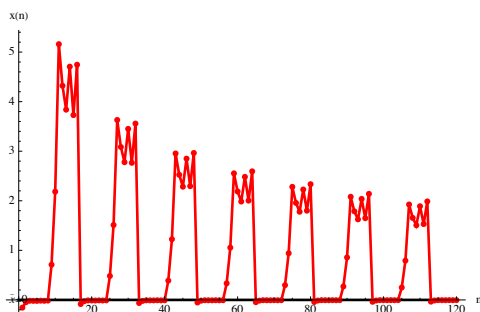


Figure 3

**Example 4.** The solution is given by Figure 4 when,

$$\begin{aligned}
 x_{-8} = 6.8, \quad x_{-7} = 6, \quad x_{-6} = 13, \quad x_{-5} = 17, \quad x_{-4} = 16, \\
 x_{-3} = 21, \quad x_{-2} = 19, \quad x_{-1} = 17, \quad x_0 = 10.5
 \end{aligned}$$

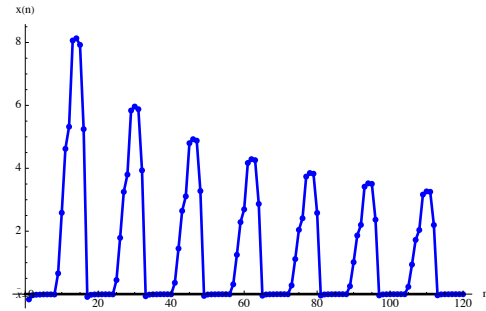


Figure 4

**4. The Equation**  $x_{n+1} = \frac{x_n x_{n-8}}{-x_{n-7} + x_n x_{n-7} x_{n-8}}$

We deal with the difference equation

$$x_{n+1} = \frac{x_n x_{n-8}}{-x_{n-7} + x_n x_{n-7} x_{n-8}}, \quad n \in \mathbb{N}_0. \quad (7)$$

where the initials are arbitrary real numbers.

**Theorem 7.** Let  $\{x_n\}_{n=-8}^\infty$  be a solution of difference equation 7. Then solutions are 16 period.

$$\left\{ \begin{aligned}
 x_{16n+1} &= \frac{aj}{h(-1+aj)}, x_{16n+2} = \frac{aj}{g}, x_{16n+3} = \frac{aj}{f(-1+aj)}, \\
 x_{16n+4} &= \frac{aj}{e}, x_{16n+5} = \frac{aj}{d(-1+aj)}, x_{16n+6} = \frac{aj}{c}, \\
 x_{16n+7} &= \frac{aj}{b(-1+aj)}, x_{16n+8} = j, x_{16n+9} = h, x_{16n+10} = g, \\
 x_{16n+11} &= f, x_{16n+12} = e, x_{16n+13} = d, x_{16n+14} = c, \\
 x_{16n+15} &= b, x_{16n+16} = a \end{aligned} \right\}.$$

**Proof** Suppose that  $n > 0$  and that our assumption holds for  $n - 1$ . Then

$$\begin{aligned}
 x_{16n-15} &= \frac{aj}{h(-1+aj)}, x_{16n-14} = \frac{aj}{g}, x_{16n-13} = \frac{aj}{f(-1+aj)}, \\
 x_{16n-12} &= \frac{aj}{e}, x_{16n-11} = \frac{aj}{d(-1+aj)}, x_{16n-10} = \frac{aj}{c}, \\
 x_{16n-9} &= \frac{aj}{b(-1+aj)}, x_{16n-8} = j, x_{16n-7} = h, x_{16n-6} = g, \\
 x_{16n-5} &= f, x_{16n-4} = e, x_{16n-3} = d, x_{16n-2} = c, \\
 x_{16n-1} &= b, x_{16n} = a.
 \end{aligned}$$

Now, it follows from 7 that

$$x_{16n+1} = \frac{x_{16n} x_{16n-8}}{-x_{16n-7} + x_{16n} x_{16n-7} x_{16n-8}} \quad (8)$$

If the found values are substituted in the Eq. 8, we have

$$x_{16n+1} = \frac{aj}{h(-1+aj)}.$$

We can prove other relations similarly.

**Theorem 8.** Equation 7 has a unique equilibrium points which are  $0, \pm\sqrt{2}$ , and these equilibrium points are not locally asymptotically stable.

**Proof** The proof is similar to the proof Theorem 4 and there it will be omitted.

**Example 5.** The solution in given by Figure 5 when,

$$x_{-8} = 7.5, \quad x_{-7} = 9, \quad x_{-6} = 13, \quad x_{-5} = 11, \quad x_{-4} = 15, \\ x_{-3} = 13.5, \quad x_{-2} = 19, \quad x_{-1} = 12, \quad x_0 = 14.$$

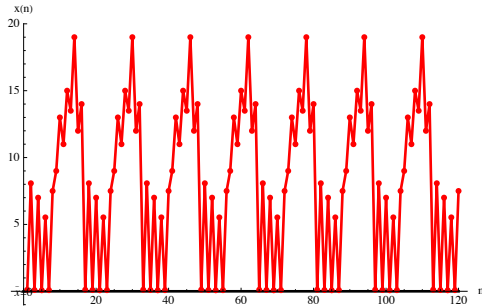


Figure 5

**Example 6.** The solution in given by Figure 6 when,

$$x_{-8} = 1.2, \quad x_{-7} = 1.5, \quad x_{-6} = 1.3, \quad x_{-5} = 1.6, \\ x_{-3} = 1.25, \quad x_{-2} = 1.45, \quad x_{-1} = 1.465, \quad x_0 = 1.245$$

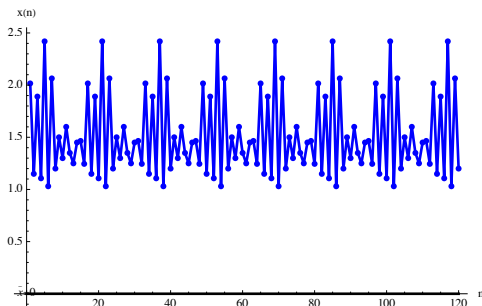


Figure 6

**5. The Equation** 
$$x_{n+1} = \frac{x_n x_{n-8}}{-x_{n-7} - x_n x_{n-7} x_{n-8}}$$
 
$$x_{n+1} = \frac{x_n x_{n-8}}{-x_{n-7} - x_n x_{n-7} x_{n-8}}, \quad n \in \mathbb{N}_0, \quad (9)$$

where the initials are arbitrary real numbers.  $x_0, x_{-8} \neq -1$ .

**Theorem 9.** Let  $\{x_n\}_{n=-8}^{\infty}$  be a solution of difference equation 9.

$$\left\{ \frac{-aj}{h(1+aj)}, \frac{aj}{g}, \frac{aj}{-f(1+aj)}, \frac{aj}{e}, \frac{-aj}{d(1+aj)}, \frac{aj}{c}, \right. \\ \left. \frac{-aj}{b(1+aj)}, j, h, g, f, e, d, c, b, a \right\}.$$

where equilibriums  $x_0, x_{-8} \neq -1$ . The solutions are obtained with 16 periods.

**Proof** The proof is the same as the proof of Theorem 7 and hence is omitted.

**Theorem 10.** Equation 6 has a unique equilibrium points which are  $0, \pm\sqrt{-2}$ , and these equilibrium points are not locally asymptotically stable.

**Proof** The proof is similar to the proof Theorem 4 and there it will be omitted.

**Example 7.** See Fig. 7 for the initials

$$x_{-8} = 6.1, \quad x_{-7} = 9.3, \quad x_{-6} = 13, \quad x_{-5} = 11, \quad x_{-4} = 15, \\ x_{-3} = 13.5, \quad x_{-2} = 19, \quad x_{-1} = 12, \quad x_0 = 14.$$

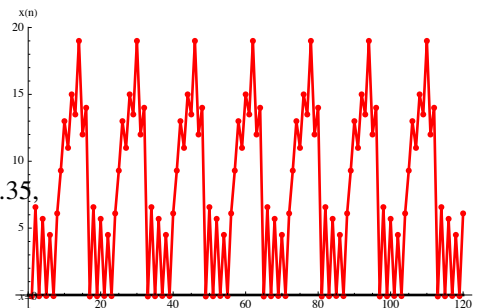


Figure 7

**Example 8.** We consider

$$x_{-8} = 6.1, \quad x_{-7} = 9.3, \quad x_{-6} = 13, \quad x_{-5} = 11, \\ x_{-4} = 15.2, \quad x_{-3} = 13.5, \quad x_{-2} = 19.2, \quad x_{-1} = 12.2, \\ x_0 = 16.$$

See figure 8

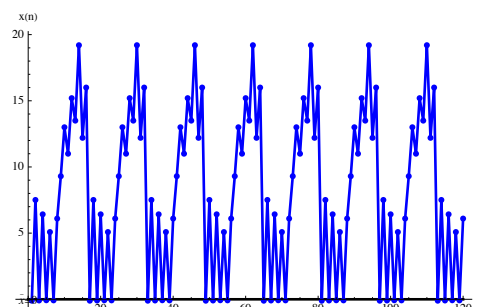


Figure 8

## 6. Conclusion

We investigate the dynamics of the difference equation expressed as

$$x_{n+1} = \frac{x_n x_{n-8}}{\pm x_{n-7} \pm x_n x_{n-7} x_{n-8}}$$

where the initial values are positive real numbers. Our analysis includes a discussion on local stability. Additionally, we obtain solutions for specific cases and provide numerical examples to further illustrate our findings.

## References

- [1] Abdelrahman M.A.E, Moaaz O., "On the New Class of The Nonlinear Rational Difference Equations," *Electronic Journal of Mathematical Analysis and Applications*, 6 (1), 117-125, (2018).
- [2] Ahmed A.E.S., Iričanin B., Kosmala W., Stević S., Smarda Z., "Note on constructing a family of solvable sine-type difference equations," *Advances in Difference Equations*, 2021(1), 1-11, (2021).
- [3] Agarwal R.P., "Difference Equations and Inequalities," Marcel Dekker, New York, 1992, 2nd edition, 2000.
- [4] Agarwal R.P. and Elsayed E.M., "On the solution of fourth-order rational recursive sequence," *Advanced Studies in Contemporary Mathematics*, 20(4), 525-545 (2010).
- [5] H.S. Alayachi, M.S.M. Noorani, A.Q. Khan, M.B. Almatrafi, Analytic Solutions and Stability of Sixth Order Difference Equations, *Mathematical Problems in Engineering*, 2020, Article ID 1230979, 12-23 (2020).
- [6] Alopeili M., "Dynamics of a rational difference equation," *Applied Mathematics and Computation*, 176(2), 768-774, (2006).
- [7] Almaslokh, A. and Qian, C., "Global attractivity of a higher order nonlinear difference equation with unimodal terms," *Opuscula Mathematica*, 43(2), 131-143 (2023).
- [8] M.B. Almatrafi, M.M. Alzubaidi, Analysis of the Qualitative Behaviour of an Eighth-Order Fractional Difference Equation, *Open Journal of Discrete Applied Mathematics*, 2, No. 1, 41-47 (2019).
- [9] Almatrafi, M.B. and Alzubaidi, M.M., Qualitative analysis for two fractional difference equations. *Nonlinear Engineering*, 9(1), 265-272 (2020).
- [10] Amleh A.M., Grove G.A., Ladas G., Georgiou, D.A., "On the recursive sequence  $y_{n+1} = \alpha + \frac{y_{n-1}}{y_n}$ ," *J. of Math. Anal. App.* 233, 790-798 (1999).
- [11] DeVault R., Ladas G., Schultz S.W., "On the recursive sequence  $x_{n+1} = \frac{A}{x_n} + \frac{1}{x_{n-2}}$ ," *Proc. Amer. Math. Soc.* 126 (11) 3257-3261 (1998).
- [12] S. Elaydi, An introduction to difference equations, 3rd Ed., Springer, USA, (2005).
- [13] Elsayed E.M., "On The Difference Equation  $x_{n+1} = \frac{x_{n-5}}{-1+x_{n-2}x_{n-5}}$ ," *Inter. J. Contemp. Math. Sci.*, 3 (33) 1657-1664, (2008).
- [14] Gibbons C.H., Kulenovic M.R.S., Ladas G., "On the recursive sequence  $\frac{\alpha+\beta x_{n-1}}{\chi+\beta x_{m-1}}$ ," *Math. Sci. Res. Hot-Line*, 4(2), 1-11 (2000).
- [15] Ibrahim T.F., Khan A.Q., Ibrahim, A., Qualitative behavior of a nonlinear generalized recursive sequence with delay, *Mathematical Problems in Engineering*, (2021).
- [16] Ibrahim, T. F., Şimşek, D., Oğul, B. The Solution and Dynamic Behaviour of Difference Equations of Twenty-First Order, *Manas Journal of Engineering*, 11(1), 159-165, (2023).
- [17] O. Karpenko, O. Stanzhytskyi, The relation between the existence of bounded solutions of differential equations and the corresponding difference equations, *Journal of Difference Equations and Applications*, 19, No. 12, 1967-1982 (2013). <https://doi.org/10.1080/10236198.2013.794795>
- [18] M. Bohner, O. Karpenko, O. Stanzhytskyi, Oscillation of solutions of second-order linear differential equations and corresponding difference equations, *Journal of Difference Equations and Applications*, 20, No. 7, 1112-1126 (2014). <https://doi.org/10.1080/10236198.2014.893297>
- [19] Khan A.Q., El-Metwally H., Global dynamics, boundedness, and semicycle analysis of a difference equation, *Discrete Dynamics in Nature and Society*, (2021).
- [20] Khyat, T., Kulenovic, M.R. and Pilav, E. The invariant curve caused by Neimark-Sacker bifurcation of a perturbed Beverton-Holt difference equation, *International Journal of Difference Equations*, 12(2), 267-280 (2017).
- [21] Kocic V.L., Ladas G., "Global behavior of nonlinear difference equations of higher order with applications," volume 256 of *Mathematics and its Applications*, Kluwer Academic Publishers Group, Dordrecht, 1993.
- [22] Kostrov, Y. and Kudlak, Z. On a second-order rational difference equation with a quadratic term. *International Journal of Difference Equations*, 11(2), 179-202 (2016).
- [23] Kulenovic M.R.S., Ladas G., Sizer W.S., "On the recursive sequence  $\frac{\alpha x_n + \beta x_{n-1}}{\chi x_n + \beta x_{n-1}}$ ," *Math. Sci. Res. Hot-Line*, 2(5), 1-16 (1998).
- [24] Kulenovic M.R.S., Ladas G., "Dynamics of second order rational difference equations" Chapman & Hall/CRC, Boca Raton, FL, 2002. With open problems and conjectures.
- [25] Oğul, B., Şimşek, D., Ögünmez, H., and Kurbanlı, A.S. Dynamical behavior of rational difference equation  $x_{n+1} = x_n - 17 \pm 1 \pm x_n - 2 x_n - 5 x_n - 8 x_n - 11 x_n - 14 x_n - 17$ , *Boletín de la Sociedad Matemática Mexicana*, 27(2), 49 (2021).
- [26] Oğul, B., Şimşek, D., Kurbanlı, A. S., Ögünmez, H., Dynamical Behavior of Rational Difference Equation  $x_{n+1} = x_n - 15 \pm 1 \pm x_n - 3 x_n - 7 x_n - 11 x_n - 15$ , *Differential Equations and Dynamical Systems*, 1-16 (2021).
- [27] Oğul, B., and Simsek, D. Dynamical behavior of one rational fifth-order difference equation. *Carpathian Mathematical Publications*, 15(1), 43-51 (2023).
- [28] Sanbo, A., Elsayed, E.M., Some properties of the solutions of the difference equation  $x_{n+1} = \alpha x_n +$

- $(bx_n x_{n-4}) / (cx_{n-3} + dx_{n-4})$ , *Open Journal of Discrete Applied Mathematics*, **2**, No. 2, 31–47 (2019).
- [29] Simsek, D., Oğul, B., Abdullayev, F., Dynamical behavior of solution of fifteenth-order rational difference equation, *Filomat*, 24(3), 997-1008 (2024)
- [30] Yalcinkaya İ., Çalışkan V., Tollu D.T., "On a nonlinear fuzzy difference equation," *Communications Faculty of Sciences University of Ankara Series A1 Mathematics and Statistics*, 71(1), 68-78, (2022).

# A modelling of the natural logarithm and Mercator series as 5<sup>th</sup>, 6<sup>th</sup>, 7<sup>th</sup> order Bézier curve in plane

Şeyda Kılıçoğlu<sup>1</sup>, Semra Yurttançıkılmaz<sup>2,\*</sup>

<sup>1</sup> Başkent University, Ankara, Türkiye, seyda@baskent.edu.tr, ORCID: 0000-0001-6712-3687

<sup>2</sup> Atatürk University, Erzurum, Türkiye, semrakaya@atauni.edu.tr, ORCID: 0000-0003-0252-1574

## ABSTRACT

In this study first, natural logarithm function  $f(x) = \ln x$  with base  $e$  has been examined as polynomial function of 5<sup>th</sup>, 6<sup>th</sup>, 7<sup>th</sup> order Bézier curve. By modelling matrix representation of 5<sup>th</sup>, 6<sup>th</sup>, 7<sup>th</sup> order Bézier curve we have found the control points in plane. Further, Mercator series for the curves  $\ln(1+x)$  and  $\ln(1-x)$  have been written too as the polynomial functions as 5<sup>th</sup>, 6<sup>th</sup>, 7<sup>th</sup> order Bézier curve in plane based on the control points with matrix form in  $E^2$ . Finally, the curve  $\ln(1-x^2)$  has been expressed as 5<sup>th</sup>, 6<sup>th</sup>, 7<sup>th</sup> order Bézier curve, examined the control points and given matrix forms.

## ARTICLE INFO

### Research article

Received: 29.04.2024

Accepted: 03.12.2024

### Keywords:

Natural logarithm,  
Mercator series,  
5<sup>th</sup> order Bézier curve,  
6<sup>th</sup> order Bézier curve,  
7<sup>th</sup> order Bézier curve.

\*Corresponding author

## 1. Introduction

Bézier curves are named after Pierre Bézier, a French engineer who used them in the 1960s for designing automobiles at Renault. They are widely used in computer graphics software like Adobe Illustrator, Photoshop, and in programming libraries such as SVG (Scalable Vector Graphics) and OpenGL for creating smooth curves in digital designs and animations. In 3D animation, Bézier curves are commonly used to define paths that objects follow through space. This is often used for creating smooth and natural-looking motion. Overall, Bézier curves are a powerful tool in 3D animation for defining both the overall path of movement and the interpolation between keyframes, helping animators create lifelike and fluid animations.

Bézier curves have been the focus of attention of many researchers due to their properties. Some of the publications that attracted our attention and examined while preparing our study are as follows: In [3], Marsh showed geometric applications for computer graphics and CAD, and also emphasized the importance of Bézier and B-spline curves in this regard. In [6], H. Hagen investigated Bézier curves with curvature and torsion continuity. In [5] and [7], Bézier curves

and Bézier surfaces were examined by H. Zhang, F. Jieqing and S. Michael. In [4], G. Farin used Bézier curves for CAD and also studied the equivalence conditions of control points and their application to planar Bézier curves. In [8], [9], [10] and [12] it has been examined cubic Bézier curves, their involutes, Bertrand and Mannheim mate of a cubic Bézier curve by using matrix representation in  $E^3$ , respectively. In [11] and [13], it has been researched matrix representation of Bézier curves and 5<sup>th</sup> order Bézier curve and their derivatives, respectively. In [14] and [15], it has been investigated Bézier curves and 5<sup>th</sup> order Bézier Curve in three dimensional Euclidean space. In [16],[17],[18] and [19], approaches to various curves (circular helix, sine wave, cosine curve and exponential curves, respectively) with various order Bézier curves were examined.

In simplest form, a Bézier curve is defined by a set of control points. A linear Bézier curve, for example, is defined by two points, while a quadratic Bézier curve is defined by three points, and a cubic Bézier curve is defined by four points.

Generally, it can be defined  $n^{\text{th}}$  order Bézier curve by  $n + 1$  control points  $P_0, P_1, \dots, P_n$  with the parametrization

$$\mathbf{B}(t) = \sum_{i=0}^n \binom{n}{i} t^i (1-t)^{n-i} [P_i].$$

For more detail see in [4], [5], [6], [7]. As is well known, Taylor series  $f(x) = \sum_{n=0}^{\infty} f^{(n)}(a) \frac{(x-a)^n}{n!}$  of a function is an infinite sum of the functions derivatives at a single point  $a$ , also a Maclaurin series  $f(x) = \sum_{n=0}^{\infty} f^{(n)}(0) \frac{x^n}{n!}$  is a Taylor series where  $a = 0$ .

In this study we will focus on the natural logarithm with base  $e$ , for 5<sup>th</sup>, 6<sup>th</sup>, 7<sup>th</sup> order Bézier curves. For more detail see [2], [8]. We need to write the coefficients matrix of any 5<sup>th</sup> order Bézier curve. It is clear that the coefficients matrix on matrix representation is 5<sup>th</sup>, 6<sup>th</sup>, 7<sup>th</sup> order Bézier curves as in the following (see [11]):

The coefficients matrix of any 5<sup>th</sup> order Bézier curve is

$$[B^5] = \begin{bmatrix} -1 & 5 & -10 & 10 & -5 & 1 \\ 5 & -20 & 30 & -20 & 5 & 0 \\ -10 & 30 & -30 & 10 & 0 & 0 \\ 10 & -20 & 10 & 0 & 0 & 0 \\ -5 & 5 & 0 & 0 & 0 & 0 \\ 1 & 0 & 0 & 0 & 0 & 0 \end{bmatrix}$$

The coefficients matrix of any 6<sup>th</sup> order Bézier curve is

$$[B^6] = \begin{bmatrix} 1 & -6 & 15 & -20 & 15 & -6 & 1 \\ -6 & 30 & -60 & 60 & -30 & 6 & 0 \\ 15 & -60 & 90 & -60 & 15 & 0 & 0 \\ -20 & 60 & -60 & 20 & 0 & 0 & 0 \\ 15 & -30 & 15 & 0 & 0 & 0 & 0 \\ -6 & 6 & 0 & 0 & 0 & 0 & 0 \\ 1 & 0 & 0 & 0 & 0 & 0 & 0 \end{bmatrix}$$

The coefficients matrix of any 7<sup>th</sup> order Bézier curve is

$$[B^7] = \begin{bmatrix} -1 & 7 & -21 & 35 & -35 & 21 & -7 & 1 \\ 7 & -42 & 105 & -140 & 105 & -42 & 7 & 0 \\ -21 & 105 & -210 & 210 & -105 & 21 & 0 & 0 \\ 35 & -140 & 210 & -140 & 35 & 0 & 0 & 0 \\ -35 & 105 & -105 & 35 & 0 & 0 & 0 & 0 \\ 21 & -42 & 21 & 0 & 0 & 0 & 0 & 0 \\ -7 & 7 & 0 & 0 & 0 & 0 & 0 & 0 \\ 1 & 0 & 0 & 0 & 0 & 0 & 0 & 0 \end{bmatrix}$$

## 2. The curve $\ln x$ as a 5<sup>th</sup>, 6<sup>th</sup>, 7<sup>th</sup> order Bézier curve

The natural logarithm is used in many areas of mathematics, science, and engineering, particularly in calculus, probability theory, and the natural sciences. It has applications in areas such as exponential growth and decay, compound interest, and solving differential equations. The natural logarithm of a number is its logarithm to the base of the mathematical constant  $e$ , which is an irrational and transcendental number. We cannot find the Maclaurin series for  $\ln(x)$ . Hence the natural logarithm of  $x$  is generally written as  $f(x) = \ln x$  with Taylor series for centered at  $x = 1$  is

$$\ln x = \sum_{k=1}^{\infty} (-1)^{k+1} \frac{(x-1)^k}{k}, \quad \text{if } 0 < x \leq 2$$

$$\ln x = (x-1) - \frac{(x-1)^2}{2} + \frac{(x-1)^3}{3} - \frac{(x-1)^4}{4} + \frac{(x-1)^5}{5} - \frac{(x-1)^6}{6} + \frac{(x-1)^7}{7} - \dots$$

**Proposition 1:** The matrix representation of the curve  $f(x) = \ln x$  as a 7<sup>th</sup> order Bézier curve has the control points  $P_0, P_1, P_2, P_3, P_4, P_5, P_6$ , and  $P_7$

$$\begin{bmatrix} P_0 \\ P_1 \\ P_2 \\ P_3 \\ P_4 \\ P_5 \\ P_6 \\ P_7 \end{bmatrix} = \begin{bmatrix} 0 & \frac{363}{140} \\ 1 & \frac{503}{140} \\ \frac{7}{7} & \frac{140}{140} \\ 2 & \frac{573}{140} \\ \frac{7}{7} & \frac{140}{140} \\ 3 & \frac{1859}{140} \\ \frac{7}{7} & \frac{420}{140} \\ 4 & \frac{491}{140} \\ \frac{7}{7} & \frac{105}{140} \\ 5 & \frac{512}{140} \\ \frac{7}{7} & \frac{105}{140} \\ 6 & \frac{353}{140} \\ \frac{7}{7} & \frac{70}{140} \\ 1 & \frac{363}{70} \end{bmatrix}$$

**Proof.** The function  $f(x) = \ln x$  has 7<sup>th</sup> degree Taylor series expansion centered  $x = 1$

$$\ln x = \frac{1}{7}x^7 - \frac{7}{6}x^6 + \frac{21}{5}x^5 - \frac{35}{4}x^4 + \frac{35}{3}x^3 - \frac{21}{2}x^2 + 7x - \frac{363}{140}$$

It can be written as in parametric form and a 7<sup>th</sup> degree polynomial function

$$(t, \ln t) = (t, \frac{1}{7}t^7 - \frac{7}{6}t^6 + \frac{21}{5}t^5 - \frac{35}{4}t^4 + \frac{35}{3}t^3 - \frac{21}{2}t^2 + 7t - \frac{363}{140})$$

It has been already known that the matrix representation of  $\alpha(t) = (t, a_7t^7 + a_6t^6 + \dots + a_1t + a_0)$  is the following matrix equation,

$$\begin{bmatrix} t^7 \\ t^6 \\ t^5 \\ t^4 \\ t^3 \\ t^2 \\ t \\ 1 \end{bmatrix}^T = \begin{bmatrix} 0 & \frac{1}{7} \\ 0 & -\frac{7}{6} \\ 0 & \frac{21}{5} \\ 0 & -\frac{35}{4} \\ 0 & \frac{35}{3} \\ 0 & -\frac{21}{2} \\ 1 & 7 \\ 0 & \frac{363}{140} \end{bmatrix} \begin{bmatrix} P_0 \\ P_1 \\ P_2 \\ P_3 \\ P_4 \\ P_5 \\ P_6 \\ P_7 \end{bmatrix}$$

**Proposition 2:** The matrix representation of the curve  $f(x) = \ln x$  as a 6<sup>th</sup> order Bézier curve has the control points that  $P_0, P_1, P_2, P_3, P_4, P_5, P_6$  are

$$\begin{bmatrix} P_0 \\ P_1 \\ P_2 \\ P_3 \\ P_4 \\ P_5 \\ P_6 \end{bmatrix} = \begin{bmatrix} 0 & -\frac{49}{20} \\ \frac{1}{6} & -\frac{20}{29} \\ 1 & -\frac{19}{20} \\ \frac{2}{3} & -\frac{20}{20} \\ 1 & -\frac{37}{20} \\ \frac{2}{2} & -\frac{60}{60} \\ \frac{2}{2} & -\frac{11}{11} \\ \frac{2}{3} & -\frac{30}{30} \\ \frac{5}{6} & -\frac{1}{6} \\ \frac{1}{6} & -\frac{6}{6} \\ 1 & 0 \end{bmatrix}$$

$$\begin{bmatrix} P_0 \\ P_1 \\ P_2 \\ P_3 \\ P_4 \\ P_5 \\ P_6 \end{bmatrix} = \begin{bmatrix} 0 & -\frac{49}{20} \\ \frac{1}{5} & -\frac{5}{4} \\ \frac{2}{5} & -\frac{4}{5} \\ \frac{3}{5} & -\frac{13}{5} \\ \frac{4}{5} & -\frac{30}{7} \\ \frac{5}{5} & -\frac{30}{30} \\ 1 & \frac{1}{6} \end{bmatrix}$$

**Proof.** The function  $f(x) = \ln x$  has 6<sup>th</sup> degree Taylor series expansion centered  $x = 1$ .

$$\ln x = -\frac{1}{6}x^6 + \frac{6}{5}x^5 - \frac{15}{4}x^4 + \frac{20}{3}x^3 - \frac{15}{2}x^2 + 6x - \frac{49}{20}, \quad \text{if } 0 < x \leq 2$$

it can be written as in parametric form and a 6<sup>th</sup> degree polynomial function

$$\alpha(t) = (t, \ln t) = \left( t, -\frac{1}{6}t^6 + \frac{6}{5}t^5 - \frac{15}{4}t^4 + \frac{20}{3}t^3 - \frac{15}{2}t^2 + 6t - \frac{49}{20} \right)$$

It has been already known that the matrix representation of  $\alpha(t) = (t, a_6t^6 + \dots + a_0)$  is as in the following equation

$$\begin{bmatrix} t^6 \\ t^5 \\ t^4 \\ t^3 \\ t^2 \\ t \\ 1 \end{bmatrix}^T \begin{bmatrix} 0 & -\frac{1}{6} \\ 0 & \frac{6}{5} \\ 0 & -\frac{15}{4} \\ 0 & \frac{20}{3} \\ 0 & -\frac{15}{2} \\ 1 & 6 \\ 0 & -\frac{49}{20} \end{bmatrix} = \begin{bmatrix} t^6 \\ t^5 \\ t^4 \\ t^3 \\ t^2 \\ t \\ 1 \end{bmatrix}^T [B^6] \begin{bmatrix} P_0 \\ P_1 \\ P_2 \\ P_3 \\ P_4 \\ P_5 \\ P_6 \end{bmatrix}$$

**Proposition 3:** The matrix representation of the curve  $f(x) = \ln x$  as a 5<sup>th</sup> order Bézier curve has the control points  $P_0, P_1, P_2, P_3, P_4, P_5$ , where  $P_0, P_1, P_2, P_3, P_4, P_5$  are

**Proof.** The function  $f(x) = \ln(x)$  has 5<sup>th</sup> degree Taylor series expansion is

$$\ln x = \frac{6}{5}x^5 - \frac{15}{4}x^4 + \frac{20}{3}x^3 - \frac{15}{2}x^2 + 6x - \frac{49}{20}$$

it can be written as in parametric form and a 5<sup>th</sup> degree polynomial function

$$(t, \ln t) = \left( t, \frac{6}{5}t^5 - \frac{15}{4}t^4 + \frac{20}{3}t^3 - \frac{15}{2}t^2 + 6t - \frac{49}{20} \right)$$

Hence we get the following equation

$$\begin{bmatrix} t^5 \\ t^4 \\ t^3 \\ t^2 \\ t \\ 1 \end{bmatrix}^T \begin{bmatrix} 0 & \frac{6}{5} \\ 0 & -\frac{15}{4} \\ 0 & \frac{20}{3} \\ 0 & -\frac{15}{2} \\ 1 & 6 \\ 0 & -\frac{49}{20} \end{bmatrix} = \begin{bmatrix} t^5 \\ t^4 \\ t^3 \\ t^2 \\ t \\ 1 \end{bmatrix}^T [B^5] \begin{bmatrix} P_0 \\ P_1 \\ P_2 \\ P_3 \\ P_4 \\ P_5 \end{bmatrix}$$

### 3. Mercator Series as a 5<sup>th</sup>, 6<sup>th</sup>, 7<sup>th</sup> order Bézier curve

The series known in mathematics as the Mercator series or Newton-Mercator series are actually the Taylor series for the natural logarithms with of  $(1+x)$  and  $(1-x)$  that are generally written as

$$\begin{aligned} \ln(1+x) &= \sum_{k=1}^{\infty} (-1)^{k+1} \frac{x^k}{k} \\ &= x - \frac{x^2}{2} + \frac{x^3}{3} - \frac{x^4}{4} + \frac{x^5}{5} - \frac{x^6}{6} + \frac{x^7}{7} \dots, \quad \text{if } -1 < x \leq 1 \end{aligned}$$

$$\begin{aligned} \ln(1-x) &= -\sum_{k=1}^{\infty} \frac{x^k}{k} \\ &= -x - \frac{x^2}{2} - \frac{x^3}{3} - \frac{x^4}{4} - \frac{x^5}{5} - \frac{x^6}{6} - \frac{x^7}{7} \dots, \quad \text{if } -1 < x \leq 1 \end{aligned}$$

Although the series were first discovered by Johannes Hudde and Isaac Newton, they were independently published by Nicholas Mercator in his 1668 treatise named Logarithmotechnia [1].

**3.1. The curve  $\ln(1 + x)$  as a 5<sup>th</sup>, 6<sup>th</sup>, 7<sup>th</sup> order Bézier curve**

**Proposition 4:** The matrix representation of the curve  $f(x) = \ln(1 + x)$  as a 7<sup>th</sup> order Bézier curve has the control points  $P_0, P_1, P_2, P_3, P_4, P_5, P_6, P_7$  as follows

$$\begin{bmatrix} P_0 \\ P_1 \\ P_2 \\ P_3 \\ P_4 \\ P_5 \\ P_6 \\ P_7 \end{bmatrix} = \begin{bmatrix} 0 & 0 \\ 1 & 1 \\ \frac{7}{7} & \frac{7}{7} \\ 2 & \frac{11}{7} \\ 3 & \frac{42}{11} \\ \frac{7}{7} & \frac{30}{11} \\ 4 & \frac{193}{30} \\ \frac{7}{7} & \frac{420}{193} \\ 5 & \frac{229}{420} \\ \frac{7}{7} & \frac{420}{229} \\ 6 & \frac{37}{420} \\ \frac{7}{7} & \frac{60}{319} \\ 1 & \frac{319}{420} \end{bmatrix}$$

**Proof.** Function  $f(x) = \ln(1 + x)$  has 7<sup>th</sup> degree Maclaurin series expansion is

$$\ln(1 + x) = x - \frac{x^2}{2} + \frac{x^3}{3} - \frac{x^4}{4} + \frac{x^5}{5} - \frac{x^6}{6} + \frac{x^7}{7}, \quad (-1 < x \leq 1)$$

it can be written as in parametric form and a 7<sup>th</sup> degree polynomial function

$$(t, \ln(1 + t)) = (t, t - \frac{t^2}{2} + \frac{t^3}{3} - \frac{t^4}{4} + \frac{t^5}{5} - \frac{t^6}{6} + \frac{t^7}{7}).$$

It has been already known that the matrix representation of  $\alpha(t) = (t, a_7t^7 + a_6t^6 + \dots + a_0)$  is as in the following equation

$$\begin{bmatrix} t^7 \\ t^6 \\ t^5 \\ t^4 \\ t^3 \\ t^2 \\ t \\ 1 \end{bmatrix}^T \begin{bmatrix} 0 & \frac{1}{7} \\ 0 & -\frac{1}{6} \\ 1 & \frac{1}{5} \\ 0 & -\frac{1}{4} \\ 0 & \frac{1}{3} \\ 0 & -\frac{1}{2} \\ 1 & 1 \\ 0 & 0 \end{bmatrix} = \begin{bmatrix} t^7 \\ t^6 \\ t^5 \\ t^4 \\ t^3 \\ t^2 \\ t \\ 1 \end{bmatrix}^T [B^7] \begin{bmatrix} P_0 \\ P_1 \\ P_2 \\ P_3 \\ P_4 \\ P_5 \\ P_6 \\ P_7 \end{bmatrix}$$

**Proposition 5:** The matrix representation of the curve  $f(x) = \ln(1 + x)$  as a 6<sup>th</sup> order Bézier curve has the control points  $P_0, P_1, P_2, P_3, P_4, P_5, P_6$  as follows

$$\begin{bmatrix} P_0 \\ P_1 \\ P_2 \\ P_3 \\ P_4 \\ P_5 \\ P_6 \end{bmatrix} = \begin{bmatrix} 0 & 0 \\ 1 & \frac{1}{6} \\ \frac{6}{3} & \frac{10}{3} \\ 1 & \frac{5}{5} \\ 2 & \frac{12}{31} \\ 2 & \frac{31}{60} \\ 3 & \frac{37}{60} \\ 5 & \frac{37}{60} \\ 6 & \frac{37}{60} \\ 1 & \frac{37}{60} \end{bmatrix}$$

**Proof.** Function  $f(x) = \ln(1 + x)$  has 6<sup>th</sup> degree Maclaurin series expansion is

$$\ln(1 + x) = x - \frac{x^2}{2} + \frac{x^3}{3} - \frac{x^4}{4} + \frac{x^5}{5} - \frac{x^6}{6}, \quad (-1 < x \leq 1)$$

it can be written as in parametric form and a 6<sup>th</sup> degree polynomial function

$$(t, \ln(1 + t)) = (t, t - \frac{t^2}{2} + \frac{t^3}{3} - \frac{t^4}{4} + \frac{t^5}{5} - \frac{t^6}{6}).$$

It has been already known that the matrix representation of  $\alpha(t) = (t, a_6t^6 + \dots + a_0)$  is as in the following equation

$$\begin{bmatrix} t^6 \\ t^5 \\ t^4 \\ t^3 \\ t^2 \\ t \\ 1 \end{bmatrix}^T \begin{bmatrix} 0 & -\frac{1}{6} \\ 0 & \frac{1}{5} \\ 0 & -\frac{1}{4} \\ 0 & \frac{1}{3} \\ 0 & -\frac{1}{2} \\ 1 & 1 \\ 0 & 0 \end{bmatrix} = \begin{bmatrix} t^6 \\ t^5 \\ t^4 \\ t^3 \\ t^2 \\ t \\ 1 \end{bmatrix}^T [B^6] \begin{bmatrix} P_0 \\ P_1 \\ P_2 \\ P_3 \\ P_4 \\ P_5 \\ P_6 \end{bmatrix}$$

**Proposition 6:** The matrix representation of the curve  $f(x) = \ln(1 + x)$  as a 5<sup>th</sup> order Bézier curve has the control points  $P_0, P_1, P_2, P_3, P_4, P_5$  as follows

$$\begin{bmatrix} P_0 \\ P_1 \\ P_2 \\ P_3 \\ P_4 \\ P_5 \end{bmatrix} = \begin{bmatrix} 0 & 0 \\ 1 & \frac{1}{5} \\ \frac{5}{2} & \frac{7}{5} \\ 2 & \frac{20}{29} \\ 3 & \frac{29}{60} \\ \frac{5}{5} & \frac{60}{7} \\ 4 & \frac{7}{12} \\ \frac{5}{5} & \frac{47}{60} \\ 1 & \frac{47}{60} \end{bmatrix}$$

**Proof.** Function  $f(x) = \ln(1 + x)$  has 5<sup>th</sup> degree Maclaurin series expansion is

$$\ln(1 + x) = x - \frac{x^2}{2} + \frac{x^3}{3} - \frac{x^4}{4} + \frac{x^5}{5}, \quad (-1 < x \leq 1)$$

it can be written as in parametric form and a 5<sup>th</sup> degree polynomial function

$$(t, \ln(1 + t)) = (t, t - \frac{t^2}{2} + \frac{t^3}{3} - \frac{t^4}{4} + \frac{t^5}{5}).$$

It has been already known that the matrix representation of  $\alpha(t) = (t, a_5t^5 + \dots + a_0)$  is as in the following equation

$$\begin{bmatrix} t^5 \\ t^4 \\ t^3 \\ t^2 \\ t \\ 1 \end{bmatrix}^T \begin{bmatrix} 0 & \frac{1}{5} \\ 0 & -\frac{1}{4} \\ 0 & \frac{1}{3} \\ 0 & -\frac{1}{2} \\ 1 & 1 \\ 0 & 0 \end{bmatrix} = \begin{bmatrix} t^5 \\ t^4 \\ t^3 \\ t \\ 1 \end{bmatrix}^T [B^5] \begin{bmatrix} P_0 \\ P_1 \\ P_2 \\ P_3 \\ P_4 \\ P_5 \end{bmatrix}.$$

### 3.2. The curve $\ln(1 - x)$ as a 5<sup>th</sup>, 6<sup>th</sup>, 7<sup>th</sup> order Bézier curve

**Proposition 7:** The matrix representation of the curve  $f(x) = \ln(1 - x)$  as a 7<sup>th</sup> order Bézier curve has the control points  $P_0, P_1, P_2, P_3, P_4, P_5, P_6, P_7$  as follows

$$\begin{bmatrix} P_0 \\ P_1 \\ P_2 \\ P_3 \\ P_4 \\ P_5 \\ P_6 \\ P_7 \end{bmatrix} = \begin{bmatrix} 0 & 0 \\ \frac{1}{7} & -\frac{1}{7} \\ \frac{2}{7} & -\frac{13}{7} \\ \frac{3}{7} & -\frac{42}{107} \\ \frac{4}{7} & -\frac{210}{319} \\ \frac{5}{7} & -\frac{420}{140} \\ \frac{6}{7} & -\frac{140}{223} \\ \frac{7}{7} & -\frac{140}{363} \\ 1 & -\frac{140}{140} \end{bmatrix}.$$

**Proof.** Function  $f(x) = \ln(1 - x)$  has 7<sup>th</sup> degree Maclaurin series expansion is

$$\ln(1 - x) = -x - \frac{x^2}{2} - \frac{x^3}{3} - \frac{x^4}{4} - \frac{x^5}{5} - \frac{x^6}{6} - \frac{x^7}{7}, \quad (-1 < x \leq 1)$$

it can be written as in parametric form and a 7<sup>th</sup> degree polynomial function

$$(t, \ln(1 - t)) = (t, -t - \frac{t^2}{2} - \frac{t^3}{3} - \frac{t^4}{4} - \frac{t^5}{5} - \frac{t^6}{6} - \frac{t^7}{7}).$$

Hence we get the following matrix equation

$$\begin{bmatrix} t^7 \\ t^6 \\ t^5 \\ t^4 \\ t^3 \\ t^2 \\ t \\ 1 \end{bmatrix}^T \begin{bmatrix} 0 & -\frac{1}{7} \\ 0 & -\frac{1}{6} \\ 0 & -\frac{1}{5} \\ 0 & -\frac{1}{4} \\ 0 & -\frac{1}{3} \\ 0 & -\frac{1}{2} \\ 1 & -1 \\ 0 & 0 \end{bmatrix} = \begin{bmatrix} t^7 \\ t^6 \\ t^5 \\ t^4 \\ t^3 \\ t^2 \\ t \\ 1 \end{bmatrix}^T [B^7] \begin{bmatrix} P_0 \\ P_1 \\ P_2 \\ P_3 \\ P_4 \\ P_5 \\ P_6 \\ P_7 \end{bmatrix}.$$

**Proposition 8:** The matrix representation of the curve  $f(x) = \ln(1 - x)$  as a 6<sup>th</sup> order Bézier curve has the control points  $P_0, P_1, P_2, P_3, P_4, P_5, P_6$  as follows

$$\begin{bmatrix} P_0 \\ P_1 \\ P_2 \\ P_3 \\ P_4 \\ P_5 \\ P_6 \end{bmatrix} = \begin{bmatrix} 0 & 0 \\ \frac{1}{6} & -\frac{1}{6} \\ \frac{1}{3} & -\frac{11}{30} \\ \frac{1}{2} & -\frac{37}{60} \\ \frac{2}{3} & -\frac{19}{20} \\ \frac{5}{6} & -\frac{29}{20} \\ 1 & -\frac{49}{20} \end{bmatrix}.$$

**Proof.** Function  $f(x) = \ln(1 - x)$  has 6<sup>th</sup> degree Maclaurin series expansion is

$$\ln(1 - x) = -x - \frac{x^2}{2} - \frac{x^3}{3} - \frac{x^4}{4} - \frac{x^5}{5} - \frac{x^6}{6}, \quad (-1 < x \leq 1)$$

it can be written as in parametric form and a 6<sup>th</sup> degree polynomial function

$$(t, \ln(1 - t)) = (t, -t - \frac{t^2}{2} - \frac{t^3}{3} - \frac{t^4}{4} - \frac{t^5}{5} - \frac{t^6}{6}).$$

Hence we get the following matrix equation

$$\begin{bmatrix} t^6 \\ t^5 \\ t^4 \\ t^3 \\ t^2 \\ t \\ 1 \end{bmatrix}^T \begin{bmatrix} 0 & -\frac{1}{6} \\ 0 & -\frac{1}{5} \\ 0 & -\frac{1}{4} \\ 0 & -\frac{1}{3} \\ 0 & -\frac{1}{2} \\ 1 & -1 \\ 0 & 0 \end{bmatrix} = \begin{bmatrix} t^6 \\ t^5 \\ t^4 \\ t^3 \\ t^2 \\ t \\ 1 \end{bmatrix}^T [B^6] \begin{bmatrix} P_0 \\ P_1 \\ P_2 \\ P_3 \\ P_4 \\ P_5 \\ P_6 \end{bmatrix}.$$

**Proposition 9:** The matrix representation of the curve  $f(x) = \ln(1 - x)$  as a 5<sup>th</sup> order Bézier curve has the control points  $P_0, P_1, P_2, P_3, P_4, P_5$  as follows

$$\begin{bmatrix} P_0 \\ P_1 \\ P_2 \\ P_3 \\ P_4 \\ P_5 \end{bmatrix} = \begin{bmatrix} 0 & 0 \\ 1 & -\frac{1}{5} \\ 2 & \frac{9}{5} \\ 3 & -\frac{20}{47} \\ 4 & \frac{60}{77} \\ 5 & -\frac{60}{137} \\ 1 & -\frac{60}{60} \end{bmatrix}$$

**Proof.** Function  $f(x) = \ln(1 - x)$  has 5<sup>th</sup> degree Maclaurin series expansion is

$$\ln(1 - x) = -x - \frac{x^2}{2} - \frac{x^3}{3} - \frac{x^4}{4} - \frac{x^5}{5}, \quad (-1 < x \leq 1)$$

it can be written as in parametric form and a 5<sup>th</sup> degree polynomial function

$$(t, \ln(1 - t)) = (t, -t - \frac{t^2}{2} - \frac{t^3}{3} - \frac{t^4}{4} - \frac{t^5}{5}).$$

Hence we get the following matrix equation

$$\begin{bmatrix} t^5 \\ t^4 \\ t^3 \\ t^2 \\ t \\ 1 \end{bmatrix}^T \begin{bmatrix} 0 & -\frac{1}{5} \\ 0 & -\frac{1}{4} \\ 0 & -\frac{1}{3} \\ 0 & -\frac{1}{2} \\ 1 & -1 \\ 0 & 0 \end{bmatrix} = \begin{bmatrix} t^5 \\ t^4 \\ t^3 \\ t^2 \\ t \\ 1 \end{bmatrix}^T [B^5] \begin{bmatrix} P_0 \\ P_1 \\ P_2 \\ P_3 \\ P_4 \\ P_5 \end{bmatrix}$$

### 3.3. The curve $\ln(1 - x^2)$ as a 4<sup>th</sup> and 6<sup>th</sup> order Bézier curve

**Proposition 10:** The matrix representation of the curve  $f(x) = \ln(1 - x^2)$  as a 6<sup>th</sup> order Bézier curve has the control points  $P_0, P_1, P_2, P_3, P_4, P_5, P_6$  as follows

$$\begin{bmatrix} P_0 \\ P_1 \\ P_2 \\ P_3 \\ P_4 \\ P_5 \\ P_6 \end{bmatrix} = \begin{bmatrix} 0 & 0 \\ 1 & 0 \\ 6 & \frac{1}{15} \\ 3 & -\frac{1}{15} \\ 2 & -\frac{1}{5} \\ 2 & -\frac{13}{30} \\ 3 & -\frac{5}{6} \\ 5 & -\frac{5}{6} \\ 6 & -\frac{11}{6} \\ 1 & -\frac{11}{6} \end{bmatrix}$$

**Proof.** We have already known that  $f(x) = \ln(1 - x^2) = \ln[(1 - x)(1 + x)]$ . Hence we get

$$\begin{aligned} \ln(1 - x^2) &= \left(x - \frac{x^2}{2} + \frac{x^3}{3} - \frac{x^4}{4} + \frac{x^5}{5} - \frac{x^6}{6} + \frac{x^7}{7}\right) \\ &+ \left(-x - \frac{x^2}{2} - \frac{x^3}{3} - \frac{x^4}{4} - \frac{x^5}{5} - \frac{x^6}{6} - \frac{x^7}{7}\right) \\ &= -\frac{1}{3}x^6 - \frac{1}{2}x^4 - x^2 \end{aligned}$$

Also it can be written as in parametric form and a 6<sup>th</sup> degree polynomial function  $(t, \ln(1 - t^2)) = (t, -\frac{1}{3}t^6 - \frac{1}{2}t^4 - t^2)$ . Hence we get the following matrix equation

$$\begin{bmatrix} t^6 \\ t^5 \\ t^4 \\ t^3 \\ t^2 \\ t \\ 1 \end{bmatrix}^T \begin{bmatrix} 0 & -\frac{1}{3} \\ 0 & 0 \\ 0 & -\frac{1}{2} \\ 0 & 0 \\ 0 & 0 \\ 1 & 0 \\ 0 & 0 \end{bmatrix} = \begin{bmatrix} t^6 \\ t^5 \\ t^4 \\ t^3 \\ t^2 \\ t \\ 1 \end{bmatrix}^T [B^6] \begin{bmatrix} P_0 \\ P_1 \\ P_2 \\ P_3 \\ P_4 \\ P_5 \\ P_6 \end{bmatrix}$$

**Proposition 11:** The matrix representation of the curve  $f(x) = \ln(1 - x^2)$  as a 4<sup>th</sup> order Bézier curve has control points  $P_0, P_1, P_2, P_3, P_4$  as follows

$$\begin{bmatrix} P_0 \\ P_1 \\ P_2 \\ P_3 \\ P_4 \end{bmatrix} = \begin{bmatrix} 0 & 0 \\ 1 & 0 \\ 4 & -\frac{1}{6} \\ 2 & -\frac{1}{3} \\ 4 & -\frac{1}{2} \\ 1 & -\frac{3}{2} \end{bmatrix}$$

**Proof.** Since  $f(x) = \ln(1 - x^2) = (x - \frac{x^2}{2} + \frac{x^3}{3} - \frac{x^4}{4} + \frac{x^5}{5}) + (-x - \frac{x^2}{2} - \frac{x^3}{3} - \frac{x^4}{4} - \frac{x^5}{5}) = -\frac{1}{2}x^4 - x^2$ ,

it can be written as in parametric form and a 4<sup>th</sup> degree polynomial function  $(t, \ln(1 - t^2)) = (t, -\frac{1}{2}t^4 - t^2)$

$$\begin{bmatrix} t^4 \\ t^3 \\ t^2 \\ t \\ 1 \end{bmatrix}^T \begin{bmatrix} 0 & -\frac{1}{2} \\ 0 & 0 \\ 0 & -1 \\ 1 & 0 \\ 0 & 0 \end{bmatrix} = \begin{bmatrix} t^4 \\ t^3 \\ t^2 \\ t \\ 1 \end{bmatrix}^T [B^4] \begin{bmatrix} P_0 \\ P_1 \\ P_2 \\ P_3 \\ P_4 \end{bmatrix}$$

Solving the above equation give us the control points, where  $[B^4]$  is the 4<sup>th</sup> order Bézier curves matrix in  $\mathbf{E}^2$ .

## References

- [1]. Vermij, Rienk. "Bijdrage tot de bio-bibliografie van Johannes Hudde". GEWINA / TGGNWT (in Dutch). 18 (1), (2012), 25–35.
- [2]. "Derivatives of a Bézier Curve" <https://pages.mtu.edu/126shene/COURSES/cs362n/NOTES/spline/Bézier/Bézier-der.html>.
- [3]. Marsh D., Applied Geometry for Computer Graphics and CAD. Springer Science and Business Media, 2006.
- [4]. Farin G., Curves and Surfaces for Computer-Aided Geometric Design. Academic Press, 1996.
- [5]. Zhang H. and Jieqing F., Bézier Curves and Surfaces (2). State Key Lab of CAD&CG Zhejiang University, 2006.
- [6]. Hagen H., Bézier-curves with curvature and torsion continuity, Rocky Mountain J. Math., 16(3), (1986), 629-638.
- [7]. Michael S., Bézier curves and surfaces, Lecture 8, Floater Oslo Oct., 2003.
- [8]. Kılıçoğlu Ş., Şenyurt S., On the cubic Bézier curves in  $E^3$ , Ordu University Journal of Science and Technology, 9(2), (2019), 83-97.
- [9]. Kılıçoğlu Ş., Şenyurt S., On the Involute of the Cubic Bézier Curve by Using Matrix Representation in  $E^3$ , European Journal of Pure and Applied Mathematics, 13(2), (2020), 216-226.
- [10]. Kılıçoğlu Ş., Şenyurt S., On the Bertrand mate of a cubic Bézier curve by using matrix representation in  $E^3$ , 18<sup>th</sup> International Geometry Sym., Malatya, Turkey, 2021.
- [11]. Kılıçoğlu Ş., Şenyurt S., On the matrix representation of Bézier curves and derivatives in  $E^3$ , Sigma J. Engineering and Natural Sci, 41(5), (2023), 992-998.
- [12]. Kılıçoğlu Ş., Şenyurt S., On the Mannheim partner of a cubic Bézier curve in  $E^3$ , International Journal of Maps in Mathematics, 5(2), (2022), 182-197.
- [13]. Kılıçoğlu Ş., Şenyurt S., On the Matrix Representation of 5<sup>th</sup> order Bézier Curve and Derivatives, Commun.Fac.Sci.Univ.Ank.Ser. A1 Math. Stat., 71(1), (2022), 133–152.
- [14]. Kılıçoğlu Ş., Şenyurt S., How to find Bézier curves in  $E^3$ , Communications in Advanced Mathematical Sciences, 5(1), (2022), 12-24.
- [15]. Kılıçoğlu Ş., Şenyurt S., An examination on to find 5<sup>th</sup> order Bézier curve in  $E^3$ , Journal of New Theory, 37, (2021), 35-44.
- [16]. Kılıçoğlu Ş., On Approximation of Helix 3<sup>rd</sup>, 5<sup>th</sup> and 7<sup>th</sup> Order Bézier Curves in  $E^3$ , Thermal Science, Vol. 26(2), (2022), 525-538.
- [17]. Kılıçoğlu Ş., On Approximation sine wave with the 5<sup>th</sup> and 7<sup>th</sup> order Bézier paths in plane, Thermal Science, Vol. 26(2), (2022), 539-550.
- [18]. Kılıçoğlu Ş., Yurttaçıkırmaz S., How to Approximate Cosine Curve with 4<sup>th</sup> and 6<sup>th</sup> order Bézier Curve in Plane, Thermal Science, Vol. 26(2), (2022), 559-570.
- [19]. Kılıçoğlu Ş., Yurttaçıkırmaz S., A Modelling on the Exponential Curves as Cubic, 5<sup>th</sup> and 7<sup>th</sup> Bézier Curve in Plane, Communications in Advanced Mathematical Sciences, 6(2), (2023), 67-77.

# A Modified Key Generation Algorithm to Rebalanced-RSA and RPower-RSA

İsrafil Okumuş<sup>1</sup>, Ercan Çelik<sup>2,\*</sup>

<sup>1</sup> Erzincan Binali Yıldırım University, Erzincan, Türkiye, [iokumus@erzincan.edu.tr](mailto:iokumus@erzincan.edu.tr), ORCID: 0000-0003-1193-3984

<sup>2</sup> Kyrgyz-Turkish Manas University, Bishkek, Kyrgyz Republic, [ercan.celik@manas.edu.kg](mailto:ercan.celik@manas.edu.kg), ORCID: 0000-0001-5971-7653

## ABSTRACT

This paper presents a novel key generation algorithm for Rebalanced-RSA and RPower-RSA that accelerates encryption and decryption processes by utilizing smaller modular exponents. Subsequently, two of these variants are modified by altering the key generation process. A theoretical analysis of all variants, including the proposed modifications, demonstrates that these key generation algorithms improve the encryption process compared to the original variants, and since the encryption key size and one of the decryption key sizes are approximately equal in length, they achieve a more balanced computational effort between encryption and decryption.

## ARTICLE INFO

### Research article

Received: 29.07.2024

Accepted: 03.12.2024

### Keywords:

RSA,  
Variation of RSA,  
Rebalanced-RSA,  
RPower-RSA,  
Key Generation  
Algorithm

\*Corresponding author

## 1. Introduction

In cryptography, there are two types of cryptosystems: secret-key and public-key. Secret-key cryptosystems use a single key, referred to as the secret key, for both encryption and decryption processes. In contrast, public-key cryptosystems utilize two distinct keys: a public key and a private key. The public key is used for the encryption, while the private key is used for the decryption process. This allows secure communication over an insecure communication channel without the need to share the private key. Therefore, public key cryptosystems are widely used for information security and digital signatures worldwide.

The RSA algorithm and its variants have played a significant role in modern cryptography, providing a foundation for secure communication and data protection. The RSA cryptosystem, first introduced by Rivest, Shamir, and Adleman [1], is one of the most widely recognized public-key cryptosystems. Many researchers have proposed various variants to enhance the efficiency of RSA [2]. Most of these efforts focus on reducing computational cost to shorten the duration of encryption or decryption.

The variants enhance decryption efficiency by speeding up the process through the use of the Chinese Remainder Theorem or the selection of shorter decryption keys.

Quisquater and Couvreur [3] proposed an RSA variant known as CRT-RSA, which utilizes the Chinese Remainder Theorem (CRT) to accelerate the decryption process. Fiat [4] introduced Batch RSA, a variant that employs a small public exponent for the same common modulus enabling the decryption of the two ciphertext at the cost of one. Wiener [5] suggested a key generation algorithm called Rebalanced-RSA, which uses small private keys to the decryption speed of CRT-RSA,

Collins et al. [6] introduced MultiPrime-RSA, where the modulus  $n$  is modified using  $k$  primes instead of just two, as in CRT-RSA. Takagi [7] proposed MultiPower-RSA, which defines the common modulus  $n: = p^k q$  and uses the Hensel-Lifting method for decryption [17]. Paixão and Filho [8] introduced an efficient variant called Rprime RSA, which combines MultiPrime-RSA and Rebalanced-RSA to improve the efficiency of MultiPrime-RSA. Grag and Verma [9] further combined Rebalanced-RSA and MultiPower-RSA to create a variant called RPower-RSA.

The Rebalanced-RSA, RPrime-RSA, and RPower-RSA variants expedite the decryption process by utilizing shorter decryption keys. However, these algorithms increase the encryption time by generating larger-sized encryption keys. This is the primary motivation for modifying these algorithms is to improve encryption performance, making them more efficient in terms of computational costs. This paper focuses on proposing a novel key generation algorithm tailored for Rebalanced-RSA and RPower-RSA variants. Initially, a concise overview of Standard RSA and its efficiency-enhancing variants is provided.

## 2. The RSA Cryptosystem

The RSA cryptosystem, like other asymmetric encryption algorithms, consists of three fundamental components: key generation, encryption, and decryption. An overview of the original RSA scheme, commonly referred to as standard RSA, follows the general procedure for key generation in the following order:

Firstly, two distinct large strong prime numbers [10],  $p$  and  $q$  of equal bit lengths are chosen, and  $n := pq$  and  $\varphi := (p - 1)(q - 1)$  are computed. Second, a random integer  $e$  is selected such that  $1 < e < \varphi$  and  $\gcd(e, \varphi) = 1$ . Finally, the integer  $d$  is computed such that  $d := e^{-1} \bmod \varphi$  using the Extended Euclidean Algorithm. The integer  $n$  serves as the common modulus, the public key  $e$  is used for encryption, and the private key  $d$  is used for decryption. The formula (1.1) is used to encrypt the plaintext  $M \in Z_n$ .

$$C := M^e \bmod n \quad (1.1)$$

The formula (1.2) gives the decrypted text from the ciphertext  $C$ .

$$M := C^d \bmod n \quad (1.2)$$

It's easy to see that the cost of both encryption and decryption processes depends roughly on the bit size of the keys and the modulus since it includes operations of modular exponentiation. [11-13]. For example, Fast Modular Exponentiation algorithm uses  $(\log e)^2 \log n$  bit operations to find  $a^e \bmod n$  [22].

To significantly speed up RSA encryption, one may try to use a much smaller public key. In this case, However, various threat assumptions are presented by Coppersmith [14].

Similarly, to speed up RSA decryption one may try to use a much smaller private key. However, Wiener [5] showed that when  $d < \frac{1}{3} \sqrt[4]{n}$  public modulus  $n$  can be factored easily. Later, Boneh and Durfee [15] presented a vulnerability called short private key exponent attack, and suggested an increase in this bound up to  $d < n^{0.292}$ .

## 3. Overview of RSA Variants and Their Improvements

All variants of RSA primarily aim to reduce the computational cost and shorten the encryption or decryption times of the RSA cryptosystem. We can classify these developed variants by categorizing into two classes [16,19]. The first class uses the Chinese Remainder Theorem (CRT) to enhance the speed of the RSA. The algorithms in this class include CRT-RSA, MultiPrime-RSA, and MultiPower-RSA. The second class speeds up the encryption process by adjusting the key size used in the algorithms from the first class. The variants in this class include Rebalanced-RSA, RPrime-RSA, and RPower-RSA. In all variants, the encryption process resembles the standard RSA.

### 3.1. CRT-based RSA variants

To speed up the RSA decryption, the key generation process has been modified in this variants. The variants in this class improve the decryption process by implementing the Chinese Remainder Theorem (CRT) algorithm, which accelerates decryption compared to standard RSA. However, the encryption operations remains like that of standard RSA, resulting in encryption time being equivalent to that of standard RSA.

**CRT-RSA:** This variant of the RSA cryptosystem utilizes the CRT to accelerate of the RSA decryption. During key generation, the public key  $e$  is selected first, o speed up decryption, the private keys  $d_p$  and  $d_q$  are computed such that

$$\begin{aligned} d_p &:= e^{-1} \bmod (p - 1) \\ d_q &:= e^{-1} \bmod (q - 1) \end{aligned} \quad (3.1)$$

To determine the plaintext, in decryption process are used the CRT or the Garner algorithm as:

$$M := M_p + p[(M_q - M_p)p^{-1} \bmod q] \quad (3.2)$$

such that

$$C_p := C \bmod p \quad (3.3)$$

$$M_p := C_p^{d_p} \bmod p \quad (3.4)$$

$$C_q := C \bmod q \quad (3.5)$$

$$M_q := C_q^{d_q} \bmod q \quad (3.6)$$

Its decryption approximately about four times faster than the standard RSA in theoretically.

**MultiPrime-RSA:** In this variant are used  $k$  primes and the common modulus are calculated as  $n := p_1 \cdot p_2 \cdot \dots \cdot p_k$ . Similar to CRT-RSA, Like CRT-RSA, the key generation process involves selecting the public key  $e$  first, and the private keys are computed as  $d_{p_i} := e^{-1} \bmod (p_i - 1)$ . The decryption precess is an extension like CRT-RSA, to determine the plaintext  $M$  are computed as

$$M := \sum_{i=1}^k \left[ M_i \cdot \left( \frac{n}{p_i} \right) \cdot \left( \left( \frac{p_i}{n} \right) \bmod p_i \right) \right] \bmod n$$

such that  $C_{p_i} := C \bmod p_i$ ,  $M_i := C_{p_i}^{d_i} \bmod p_i$ . The speed of decryption is approximately about  $2k$  times faster than the standard RSA in theoretically.

**MultiPower-RSA:** In this variant, the common modulus is calculated as  $n := p^k q$ , where  $k \geq 2$  is an integer. When

generating keys, the public key  $e$  and private keys  $d_p$  and  $d_q$  are calculated like CRT-RSA. While decrypting the chipper text  $C$ , to begin with, the values of  $M_p$  and  $M_q$  are calculated and then the values of  $M_{p^k}$  and  $M_q$  are combined via CRT algorithm as

$$M = M_{p^k} + p^k \cdot [(M_q - M_{p^k}) \cdot p^{-k}] \bmod q \quad (3.7)$$

such that  $M_{p^k} \equiv M \bmod p^k$  which is can be calculated by using the Hensel-Lifting method was introduced by Takagi [17]. For example, it is calculated using the following formula (for  $k=2$ )

$$M_{p^2} = M_p + [(C - M_p^e \bmod p^2)(e^{-1} \bmod p)(C_p^{d_p^{-1}} \bmod p)] \bmod p^2 \quad (3.8)$$

This approach speeds up the decryption process by leveraging the power of the modulus about 3 times faster than CRT-RSA [6].

### 3.2. RSA variants using shorter decryption keys

The algorithms in this class shorten the decryption process by selecting shorter decryption keys in CRT-based RSA variants, but, it is important to note that the encryption process becomes more time-consuming compared to both the standrad RSA and the algorithm in the first class.

**Rebalanced-RSA:** To shorten the time of decryption process CRT-RSA. Initially, when generating keys, private keys  $d_p$  and  $d_q$  are chosen short size, satisfying  $\gcd(d_p, p-1) = \gcd(d_q, q-1) = 1$ . The integer  $d$  is computed using the Garner algorithm, such that:

$$d = d_q + (q-1) \cdot [(d_q - d_p) \cdot (p-1)^{-1}] \bmod (q-1)$$

to obtain the public key as  $e = d^{-1} \bmod \varphi$ .

In this algorithm, the encryption and decryption process are like standard RSA. The private keys are chosen to be shorter in size, which speeds up the decryption process and the decryption time is significantly faster. However, since the bit size of the encryption key is approximately equal to the bit size of  $\varphi$ , the encryption time increases compared to standard RSA.

**Rprime-RSA (Rebalanced MultiPrime-RSA):** for  $n := p_1 \cdot p_2 \dots p_k$  ( $k$  primes) the private key generation is similar to Rebalanced-RSA to further improve the decryption speed of MultiPrime-RSA and the decryption process is considered as MultiPrime-RSA. To shorten the decryption are chosen short private keys  $d_i$ . The integer  $d$  is calculated with CRT such that  $d := d_{p_i} \bmod (p_i - 1)$  to get  $e := d^{-1} \bmod \varphi$ . Note that, we can calculate the private key as  $d_{k-1}$  by applying Garner algorithm successively as follows:

$$d_1 = d_{p_1} + (p_1 - 1)[(d_{p_2} - d_{p_1})(p_1 - 1)^{-1} \bmod (p_2 - 1)]$$

$$d_2 = d_1 + (p_1 - 1)(p_2 - 1)[(d_{p_3} - d_1)(p_1 - 1)(p_2 - 1)^{-1} \bmod (p_3 - 1)]$$

$$d_3 = d_2 + \prod_{i=1}^3 (p_i - 1) \left[ (d_{p_4} - d_2) \left( \prod_{i=1}^3 (p_i - 1) \right)^{-1} \bmod (p_4 - 1) \right]$$

...

$$d_{k-1} = d_{k-2} + \prod_{i=1}^{k-2} (p_i - 1) \left[ (d_{p_{k-2}} - d_{k-2}) \left( \prod_{i=1}^{k-2} (p_i - 1) \right)^{-1} \bmod (p_{k-2} - 1) \right]$$

Its decryption process is approximately 8 times faster than the CRT-RSA and about 27 times faster than the standard RSA theoretically (for 2048 bits) [8]. However, like Rebalanced-RSA the encryption time increases compared to MultiPrime-RSA.

**RPower-RSA (Rebalanced MultiPower-RSA):** Similarly, in RPrime-RSA, the key generation process is modified to enhance the decryption performance of MultiPower-RSA. The private key generation is like that of Rebalanced-RSA, when generating keys, firstly, private keys  $d_p$  and  $d_q$  are chosen and the public key is calculated as  $e = d^{-1} \bmod \lambda$  such that  $\lambda = (p-1)(q-1)$  and the integer  $d$  is calculated with the CRT.

The decryption process is the same as MultiPower-RSA, and it achives a speed gain of approximately 56 times over the RSA cryptosystem [18].

## 4. A Modified Key Generation Algorithm for Rebalanced-RSA and RPower-RSA

In this section, we present two new modified key generation algorithms for Rebalanced-RSA and RPower-RSA to minimize the gap between encryption and decryption times. The encryption and decryption operations are performed in the same way as in the variants under consideration.

In standard RSA, key generation begins with selecting an integer  $e$ , followed by computing  $d$ . In CRT-RSA,  $e$  is selected first, and then  $d_p$  and  $d_q$  are computed. Rebalanced-RSA, on the other hand, reverses the process:  $d_p$  and  $d_q$  are chosen first, followed by the computation of  $e$ . The modified Rebalanced-RSA algorithm changes this sequence slightly, starting with the selection of  $d_p$ , then computing  $e$ , and finally  $d_q$ . This adjustment ensures that the bit size of  $e$  and one of the decryption keys is approximately equal, balancing encryption and decryption times. A similar approach is applied to RPower-RSA, achieving comparable improvements.

### 4.1. Modified key generation algorithm for Rebalanced-RSA

To achieve the encryption and decryption times close for Rebalanced-RSA we first select  $d_p$  with a very short bit size such that  $\gcd(d_p, p-1) = 1$ . Then, the integer  $e$  and  $d_q$  are



The encryption and decryption times in Rebalanced-RSA and RPower-RSA are generally longer than in standard RSA due to the increased bit size of the public key exponent  $e$ , which is equal to the bit size of  $\varphi$ . However, the key generation algorithms presented in Section 4 address this by modifying the bit sizes of the keys. In the proposed method, the bit size of  $e$  is approximately equal to the bit size of  $p$ , resulting in a shorter encryption time compared to the original variants. Additionally, the bit size of one decryption key is approximately equal to the bit size of  $q$ , leading to encryption and decryption times that are closer to each other. In the modified key generation algorithm for Rebalanced-RSA, the bit size of  $e$  being roughly equal to the bit size of  $p$  significantly reduces the encryption time compared to the

original Rebalanced-RSA. Likewise, the bit size of one decryption key being approximately equal to  $q$  ensures encryption and decryption times are well-balanced. In the modified RPower-RSA key generation algorithm, the same principle is applied. Furthermore, when computing  $M_{pk}$ , the exponent  $e$  is used, enhancing the efficiency of the encryption process compared to the original RPower-RSA. These modifications collectively improve the overall performance of both encryption and decryption operations.

To compare RSA and its variants with the two new key generation algorithms presented in this paper, a table containing the key lengths was created for  $n = 1024$  bit size.

**Table 5. 1:** Key Length of Algorithms(bit size)

| Algorithms                        | Primes                    | Public key | Private key(s)            |
|-----------------------------------|---------------------------|------------|---------------------------|
| RSA                               | $p = q = 512$             | $e = 16$   | $d = 1024$                |
| CRT-RSA                           | $p = q = 512$             | $e = 16$   | $dp = dq = 512$           |
| MultiPrime-RSA (for $k=4$ primes) | $p1 = p2 = p3 = p4 = 256$ | $e = 16$   | $d1 = d2 = d3 = d4 = 256$ |
| MultiPower-RSA (for $p^3q$ )      | $p = q = 256$             | $e = 16$   | $dp = dq = 256$           |
| ReBalanced-RSA                    | $p = q = 512$             | $e = 1024$ | $dp = dq = 16$            |
| Modified Rebalanced-RSA           | $p = q = 512$             | $e = 512$  | $dp = 16, dq = 512$       |
| Rprime-RSA                        | $p1 = p2 = p3 = p4 = 256$ | $e = 1024$ | $d1 = d2 = d3 = d4 = 16$  |
| Rpower-RSA (for $p^3q$ )          | $p = q = 256$             | $e = 512$  | $dp = dq = 16$            |
| Modified Rpower-RSA (for $p^3q$ ) | $p = q = 256$             | $e = 256$  | $dp = 16, dq = 256$       |

As shown in Table 5.1, in the new algorithms, when one of the private keys is selected to be very short, the size of the public key is reduced. Additionally, the bit size of the other private key is approximately equal to the bit size of  $e$  in this scheme. As a result, the encryption and decryption times will be closer to each other.

## 6. Conclusion

In this paper, we propose two novel key generation algorithms as modifications to Rebalanced-RSA and RPower-RSA. The first proposed algorithm reduces the encryption time compared to Rebalanced-RSA, while maintaining a balance between encryption and decryption times, ensuring a more efficient computational effort. Similarly, the second proposed algorithm reduces the encryption time relative to RPower-RSA, with encryption and decryption times remaining approximately equal, thereby demonstrating improved efficiency and a well-balanced computational performance. Also, when calculating the number  $M_{p^2}$  in eq. (3.8) for  $k = 2$ , the number  $e$  is used as the exponent. So, the modified RPrime key generating algorithm further improves encryption process compared to original RPower-RSA.

## REFERENCES

- [1] R. L. Rivest, A. Shamir and L. Adleman, "A method for obtaining digital signatures and public key cryptosystem," Communications of the ACM, vol. 21, no. 2, pp. 120-126, 1978.
- [2] D. Boneh and H. Shacham, "Fast Variants of RSA," CryptoBytes, vol. 5, no. 1, pp. 1-9, 2002.
- [3] J. J. Quisquater and C. Couvreur, "Fast decipherment algorithm for RSA public-key cryptosystem," Electronics Letters, vol. 18, no. 21, pp. 905-907, 1982.
- [4] A. Fiat, "Batch RSA," Journal of Cryptography, vol. 10, no. 2, pp. 175-195, 1995.
- [5] M. J. Wiener, "Cryptanalysis of sort RSA secret exponents," IEEE Transactions on Information Theory, vol. 36, pp. 553-558, 1990.
- [6] T. Collins, D. Hopkins, S. Langford and M. Sabin, "Public Key Cryptographic Apparatus and Method". Us Patent #5,848,159, Jan. 1997.

- [7] T. Takagi, "Fast RSA-Type Cryptosystem modulo  $p^kq$ ," *Advances in Cryptography - CRYPTO'98* Springer, vol. 1462, pp. 318-326, 1998.
- [8] C. A. M. Paixao and D. L. G. Filho, "An efficient variant of the RSA cryptosystem," 2005.
- [9] S. Verma and D. Garg, "Improvement in RSA Cryptosystem," *Journal of Advances Information Technology*, vol. 2, no. 3, 2011.
- [10] J. Gordon, "Strong RSA keys," *Electronics Letters*, vol. 20, no. 12, pp. 514-516, 1984.
- [11] D. M. Gordon, "A Survey of Fast Exponentiation Methods," *Journal of algorithms*, vol. 27, no. 1, pp. 129-146, 1998.
- [12] Ç. K. Koç, "High-Speed RSA Implementation," *RSA Laboratories*, Redwood City, CA 94065-1031, 1994.
- [13] P. L. Montgomery, "Modular multiplication without trial division," *Mathematics of Computation*, vol. 44, no. 170, pp. 519-521, 1985.
- [14] D. Coppersmith, "Small Solutions to Polynomial Equations and Low Exponent RSA Vulnerabilities," *Journal of Cryptology*, vol. 10, pp. 233-260, 1997.
- [15] D. Boneh and G. Durfee, "Cryptanalysis of RSA with Private Key  $d$  less than  $N^{0.292}$ ," *IEEE Transactions on Information Theory*, vol. 46, no. 4, pp. 1339-1349, 2000.
- [16] İ. Okumuş and E. Çelik, "Classification of factors that affect the speed of the RSA cryptosystem," in *Georgian Mathematical Union Third International Conference*, Batumi, GEORGIA, 2012, September 2-9.
- [17] T. Takagi, "A Fast RSA\_Type Public-Key Primitive Modulo  $pkq$  Using Hensel Lifting," *IEICE TRANSACTIONS on Fundamentals of Electronics, Communications and Computer Sciences*, Vols. E87-A, no. 1, pp. 94-101, 2004.
- [18] D. Garg and S. Verma, "Improvement over Public Key Cryptographic Algorithm," in *2009 IEEE International Advance Computing Conference (IACC 2009)*, Patiala, 2009.
- [19] İ. Okumuş, *The Factors Affecting of RSA Cryptosystem*, Ataturk University: Ph. D. Thesis, 2012.
- [20] A. Shamir, "RSA for paranoids," *CryptoBytes (The technical Newsletter of RSA Laboratories)*, vol. 1, pp. 1-4, 1995.
- [21] G. Horng, "Identification Scheme Based on Shamir's 'RSA for Paranoids,'" *Electronic Letters*, vol. 35, no. 22, pp. 1941-1942, 1999.
- [22] Kenneth H. Rosen, *"Discrete Mathematics Applications"*, Eighth Edition, New York, NY : McGraw-Hill, 2019.

# Investigation of growth and survival of some pathogens in koumiss

Fatih Ramazan İstanbullugil<sup>1,\*</sup>, Mustafa Atasever<sup>2</sup>

<sup>1</sup> Kyrgyz-Turkish Manas University, Faculty of Veterinary Medicine, Department of Food Hygiene and Technology, KG-720038 Bishkek - KYRGYZ REPUBLIC, fatih.ramazan@manas.edu.kg, ORCID: 0000-0001-9610-2797

<sup>2</sup> Ataturk University, Faculty of Veterinary Medicine, Department of Food Hygiene and Technology, TR-25070 Erzurum - TÜRKİYE, email, ORCID: 0000-0002-1627-5565

\*This manuscript is derived from the PhD thesis of the first author.

## ABSTRACT

The aim of this study was to investigate the growth and survival of *Escherichia coli* O157:H7, *Listeria monocytogenes* and *Staphylococcus aureus* in koumiss produced from raw mare's milk during the fermentation process. *E. coli* O157:H7 (Group 1), *L. monocytogenes* (Group 2) and *S. aureus* (Group 3) were added to the raw mare's milk that would be used to produce koumiss and a combination of all three pathogens (Group 4) was inoculated. These microorganisms were introduced at 10<sup>6</sup> CFU/mL concentration into the raw mare's milk, which served as the base for koumiss production. During fermentation, microbiological and chemical analyses were carried out by taking one sample from each group at the 1st, 5th and 24th hours and at the 2nd, 3rd, 4th and 5th days. As a result of analyses, pH, dry matter, and protein content declined, while titration acidity and alcohol content increased. A positive correlation was found between the bacterial count and the utilized pathogenic microorganisms. Conversely, a negative correlation was observed with the count of yeast molds. Remarkably, the counts of *E. coli* O157:H7, *L. monocytogenes*, and *S. aureus* reduced starting from the fifth hour of fermentation and diminished to undetectable levels by the second day. This decline in pathogenic microorganisms below detectable thresholds during the fermentation process was linked to the rise in titration acidity and alcohol content and the decrease in pH.

## ARTICLE INFO

### Research article

Received: 06.08.2024

Accepted: 08.12.2024

### Keywords:

*E. coli* O157:H7, koumiss, mare's milk, *L. monocytogenes*, *S. aureus*.

\*Corresponding author

## 1. Introduction

Fermented foods play a crucial role as nutritional sources in societies residing in developing regions across the globe. Additionally, traditional fermented products serve as abundant reservoirs of diverse bioactive compounds [1]. Various fermented milk products are prevalent worldwide, including koumiss, kefir, shubat, yakult, acidophilus, bifidus, and others. Incorporating probiotic flora into fermented dairy items contributes to the desired texture and flavor as well as having positive physiological effects [2]. Lactic acid bacteria in these foods have a significantly impact on consumer health, inhibiting pathogenic bacteria and generating antibacterial effects [3].

Koumiss has been a popular beverage in Kyrgyzstan, Kazakhstan, Mongolia, and among the Turkic, Mongolian, and Caucasian peoples of Russia, including the Altay, Bashkortostan, Buryatia, Dagestan, Kabardino-Balkaria,

Kalmykia, Karachaevo-Cherkessia, Tatarstan, Tyva, Chuvashia, and Saha (Yakutia) regions [4]. Koumiss, a fermented product, is an example of an alcoholic acid product traditionally derived from mare's milk fermentation [5-7]. The term "koumiss" is spelled similarly in multiple languages, such as kumiss, kuymiss, kymyz, qymyz, qimiz, and kumiz [8]. Notably, distinct terminology like chigo, chigee, airag, and kumiss is utilized in Mongolia [1,9]. Researchers have found that certain types of bacteria, including *Lactobacillus*, *Lactococcus*, *Acetobacter*, *Streptococcus*, *Serratia*, and *Leuconostoc*, as well as fungi, such as *Kazachstania*, *Kluyveromyces*, *Trichosporonaceae*, *Pichia*, and *Candida*, are most common in the traditional fermentation process [10].

Typically, koumiss contains approximately 0.7–1.8% lactic acid, 0.6–2.5% ethyl alcohol, and 0.5–0.9% carbon dioxide [11]. The concentrations of acid and alcohol in koumiss exhibit variations based on factors such as fermentation duration and incubation temperature during its production [6,12]. Throughout history to the present day, koumiss has been employed to address various health issues [13-16]. These include anorexia, pulmonary tuberculosis, gastritis, typhoid, paratyphoid, dysentery, constipation, diarrhea, anemia, indigestion, and fatigue [17]. Including mare's milk in the human diet has experienced rapid growth in numerous European countries such as Germany, France, Belgium, Austria, Croatia, and the Netherlands [18].

The nutrients in the milk blend create an optimal milieu for the growth and proliferation of microorganisms. Milk originating from a healthy animal's udder remains devoid of microorganisms. Nevertheless, milk is susceptible to contamination throughout the milking procedure, whether transportation or direct contact with the animal [19]. It has been demonstrated that the presence of lactic acid bacteria in fermented products, such as koumiss, not only serves to preserve these products but also enhances their probiotic potential, thereby conferring health benefits that include improved gut microbiota balance and immune system modulation [20].

The goal of this study was to find out how well pathogenic microorganisms like *Escherichia coli* O157:H7, *Listeria monocytogenes*, and *Staphylococcus aureus* could grow and stay alive during the fermentation process in koumiss, which is a traditional fermented product made from mare's milk.

## 2. Materials and Methods

The study sourced mare's milk from family farms in Kyrgyzstan, specifically in Bishkek, and utilized koumiss samples to obtain a starter culture. The production of koumiss was conducted using wooden barrels. As for the pathogens, *Escherichia coli* O157:H7 (ATCC 43894), *Listeria monocytogenes* (ATCC 7644), and *Staphylococcus aureus* (NCTC 10654) were employed in the research.

### Inoculum preparation and inoculation

In the nutrient broth medium, *L. monocytogenes* was subjected to a 24-h incubation at 30°C, while *S. aureus* and *E. coli* O157:H7 were incubated at 35°C for the same duration. After growth, the bacterial strain underwent centrifugation at 3000 rpm for 5 min, facilitating the removal of the supernatant. The resultant pellet was rinsed using 9 ml of ¼ Ringer's solution and subjected to an additional centrifugation cycle. Following this centrifugation, the supernatant was once again collected, and the pellet was dispersed by adding 9 ml of ¼ Ringer's solution. This procedure yields the initial solution. To determine the count of pathogenic microorganisms, dilutions were conducted up to 10<sup>-6</sup> dilutions, and the microbial count in the solution within the tube was quantified. After 24 h of storage at 4°C, the pellet underwent further dilution to 10<sup>-6</sup>

dilutions, and its count was determined. A direct correlation was established between the microbial counts derived from these measurements. Utilizing the acquired data, an inoculation strain averaging 10<sup>6</sup> CFU/mL was prepared for introduction into experimental milk [21]. This inoculation was done at 25°C, mirroring the fermentation conditions of the mare's milk [11].

### Experimental production of koumiss

Following microbiological and chemical assessments koumiss derived from mare's milk was employed as a starter culture in the experimental production of koumiss [22]. Koumiss starter culture was introduced to the mare's milk in a proportion of 20%, the mixture homogenized using a blending apparatus, and subsequently incubated at 25°C for up to 5 days. The wooden barrel was intermittently stirred during this incubation period using an appropriate stirring device. For the research, all three pathogenic microorganisms were initially introduced separately and subsequently, in combination, into raw mare's milk. The initial concentration of pathogens inoculated into the experimental groups stood at 10<sup>6</sup> CFU/mL. The categorization was as follows: Group 1 represented *E. coli* O157:H7, Group 2 signified *L. monocytogenes*, Group 3 denoted *S. aureus*, and Group 4 comprised all three pathogens in simultaneous interaction. Microbiological and chemical analyses punctuated the fermentation course through sample collection at distinct intervals, including the 1st, 5th, and 24th hours, as well as the 2nd, 3rd, 4th, and 5th days.

### Microbiological analyses

The mare's milk and koumiss, produced using traditional methods, were meticulously blended. Samples of 1 ml each were collected under aseptic conditions, and decimal dilutions (up to 10<sup>-7</sup>) were meticulously prepared. These samples were subsequently incubated and subjected to a double serial plating method using petri dishes, with the pour plate technique employed.

For the enumeration of Total Mesophilic Aerobic Colonies (TMAB), Plate Count Agar (PCA) (Merck 1.05463) was utilized. The agar was inoculated and then incubated at 32°C for 48 to 72 h, after which the colonies were counted. In the case of total psychrophilic aerobic colonies (TPAB), PCA agar (Merck 1.05463) was employed. This medium was cultivated and incubated at 7°C for 7 days, and subsequent colony enumeration was performed [23]. For the enumeration of *Enterobacteriaceae* spp., Violet Red Bile Dextrose Agar (VRBD) agar (Merck 1.10275) was used. The agar was inoculated and incubated at 37°C for 24 h, followed by colony counting. Yeast and Mold enumeration involved using Yeast Extract Glucose Chloramphenicol Agar (YGC) agar (Merck 1.16000). This medium was cultivated and incubated at 22°C for 5 days, after which colony counting was carried out [23]. DeMan, Rogosa, and Sharpe (MRS) agar (Merck 1.10660) were used for enumeration of *Lactobacillus* spp. The agar was

plated and incubated at 30°C for 72 hours, followed by colony counting [24]. Regarding *E. coli* O157:H7, Sorbitol MacConkey Agar (SMAC) agar (Merck 1.09202) supplemented with Cefixime Tellurite Selective (Oxoid, SR 0172 E) was utilized. The agar was cultivated, and the colonies were counted after incubation at 35°C for 24 h [24]. Furthermore, samples were procured from the breeding colonies for additional testing. Indole, Methyl Red, Voges Proskauer, and Citrate (IMVIC) tests were administered [25].

For the enumeration of *L. monocytogenes*, Palcam Agar Selective Supplement (Merck 1.12122) was inoculated onto Palcam Agar (Merck 1.11755) medium. Following incubation at 35°C for 24 to 48 h, colonies displaying a distinctive brown-olive color with a black zone were enumerated [23]. Additional testing, including Gram staining, oxidase testing, catalase testing, and  $\beta$ -hemolysis testing, was conducted on samples obtained from the growing colonies [26].

After inoculating *S. aureus* onto Baird-Parker agar (Merck 1.05406) and adding egg yolk tellurite emulsion (Merck 1.03785), we incubated the culture at 37°C for 48 hours. Distinctive bright black colonies measuring 1–3 mm in diameter were identified and quantified [24].

Samples were collected from actively growing colonies and subjected to the streak plate technique. These samples were then inoculated onto a pre-prepared blood agar medium. After inoculation, the plates were incubated at 37°C for 24 h. The appearance of clear zones surrounding the colonies on the blood agar was used to evaluate the occurrence of  $\beta$  hemolysis. After this, Gram staining, oxidase, and catalase testing were conducted on the colonies cultivated in the blood agar [26].

### Chemical analysis

The pH analysis of the mare's milk and koumiss was executed using a pH meter (Thermo Scientific Orion 3-star benchtop,

USA). The assessment of total acidity was conducted through the lactic acid percentage method. Nitrogen content (%) was gauged employing the micro-Kjeldahl method. Determination of dry matter content was executed gravimetrically. The determination of ash content involved quantifying the residual inorganic components in the samples after moisture evaporation and incineration of organic constituents [27].

Following the guidelines outlined by the Gosudarstvennyy Standard (GOST), the quantification of alcohol content in koumiss was conducted using the method specified in GOST 3629-47. This approach was also employed for determining the ethyl alcohol content in dairy products such as kefir and koumiss [28].

### Statistical analysis

Bacterial counts were transformed into log<sub>10</sub> CFU/mL using the SPSS software package. Subsequently, alterations in the population of pathogenic microorganisms were juxtaposed against the temporal progression of the experiments. Within this framework, the data underwent analysis of variance (ANOVA) testing based on the x-time model, with a thorough assessment of intervariable interactions. Duncan's multiple comparison test delineated variations between significant means. The statistical significance of the analysis results was evaluated at significance levels of  $p < 0.05$  and  $p < 0.01$ .

### 3. Results

The physicochemical and microbiological characteristics of raw mare's milk, utilized in the production of koumiss, along with koumiss utilized as a starter culture and experimental koumiss samples, were subjected to investigation. Table 1 displays the physicochemical properties of the raw mare's milk and the koumiss employed in this study.

**Table 1.** Phytochemical characteristics of the raw mare's milk and the koumiss used in the study. (n=10)

| Parameters                | Mare's milk |       |            | Koumiss |       |            |
|---------------------------|-------------|-------|------------|---------|-------|------------|
|                           | min         | max   | mean±SD    | min     | max   | mean±SD    |
| ph                        | 6.37        | 7.18  | 6.84±0.30  | 3.80    | 4.57  | 4.04±0.23  |
| Titratable acidity (% LA) | 0.07        | 0.09  | 0.08±0.01  | 0.93    | 1.08  | 0.99±0.06  |
| Dry matter (%)            | 10.72       | 11.28 | 10.95±0.17 | 9.80    | 10.63 | 10.28±0.27 |
| Protein (%)               | 2.14        | 2.52  | 2.38±0.13  | 2.09    | 2.18  | 2.12±0.03  |
| Ash (%)                   | 0.30        | 0.37  | 0.33±0.02  | 0.23    | 0.36  | 0.29±0.04  |
| Alcohol (%)               | -           | -     | -          | 0.60    | 1.20  | 0.80±0.17  |

Meanwhile, Table 2 presents the microbiological properties of the raw mare's milk and the koumiss utilized in the experimental procedures. Table 3 illustrates the microbiological transformations observed in the experimental

koumiss samples throughout the incubation period, while Table 4 outlines the resultant physicochemical alterations.

**Table 2.** Microbiological properties of raw mare's milk and koumiss used in the experiments.(n=10)

| Microorganism                 | Number of Microorganisms (log10 CFU/mL) |           |
|-------------------------------|---|-----------|
|                               | Mare's milk                             | Koumiss   |
| TMAB                          | 4.71±0.30                               | 6.88±0.58 |
| <i>Enterobacteriaceae spp</i> | 1.07±1.54                               | ND        |
| Yeast Mold                    | 0.40±0.66                               | 6.42±0.53 |
| TPAB                          | 4.08±0.30                               | 5.71±0.45 |
| <i>Lactobacillus spp.</i>     | 1.50±1.60                               | 7.10±0.36 |

ND: Not Detected

**Table 3.** Microbiological changes during fermentation in experimentally produced koumiss samples (log10 CFU/mL).

| Groups     | Microorganism            | Times                   |                        |                        |                         |                         |                         |                         |
|------------|--------------------------|-------------------------|------------------------|------------------------|-------------------------|-------------------------|-------------------------|-------------------------|
|            |                          | 1. hour                 | 5. hour                | 24. hour               | 2.day                   | 3.day                   | 4.day                   | 5.day                   |
| 1. group   | <i>E. coli O157:H7</i>   | 6.60±0.30 <sup>a</sup>  | 5.46±0.40 <sup>b</sup> | 2.00±2.23 <sup>c</sup> | <1.0                    | <1.0                    | <1.0                    | <1.0                    |
|            | TMAB                     | 6.94±0.36 <sup>b</sup>  | 7.08±0.34 <sup>b</sup> | 7.74±0.53 <sup>a</sup> | 4.29±0.50 <sup>d</sup>  | 6.70±0.72 <sup>bc</sup> | 6.39±0.34 <sup>c</sup>  | 6.37±0.34 <sup>c</sup>  |
|            | TPAM                     | 6.52±0.36 <sup>b</sup>  | 6.45±0.47 <sup>b</sup> | 7.06±0.64 <sup>a</sup> | 4.08±0.33 <sup>d</sup>  | 6.26±0.48 <sup>b</sup>  | 5.26±0.36 <sup>c</sup>  | 5.24±0.42 <sup>c</sup>  |
|            | <i>Lactobacillus spp</i> | 5.90±0.47 <sup>a</sup>  | 7.00±0.44 <sup>b</sup> | 7.40±0.35 <sup>a</sup> | 5.62±0.38 <sup>a</sup>  | 6.76±0.34 <sup>b</sup>  | 5.51±0.44 <sup>a</sup>  | 5.62±0.39 <sup>a</sup>  |
|            | Yeast Mold               | 5.57±0.39 <sup>c</sup>  | 5.03±0.43 <sup>d</sup> | 6.06±0.46 <sup>b</sup> | 5.24±0.23 <sup>cd</sup> | 6.72±0.47 <sup>a</sup>  | 6.32±0.32 <sup>b</sup>  | 6.39±0.34 <sup>ab</sup> |
| 2. group   | <i>L. monocytogenes</i>  | 6.44±0.34 <sup>a</sup>  | 5.22±0.52 <sup>b</sup> | 3.19±2.23 <sup>c</sup> | <1.0                    | <1.0                    | <1.0                    | <1.0                    |
|            | TMAB                     | 6.86±0.36 <sup>ab</sup> | 7.18±0.36 <sup>a</sup> | 7.17±0.29 <sup>a</sup> | 4.45±0.64 <sup>d</sup>  | 6.49±0.41 <sup>bc</sup> | 6.19±0.56 <sup>c</sup>  | 6.39±0.39 <sup>c</sup>  |
|            | TPAM                     | 6.42±0.36 <sup>ab</sup> | 6.13±0.32 <sup>b</sup> | 6.63±0.36 <sup>a</sup> | 4.05±0.37 <sup>d</sup>  | 6.22±0.46 <sup>b</sup>  | 5.26±0.40 <sup>c</sup>  | 5.23±0.43 <sup>c</sup>  |
|            | <i>Lactobacillus spp</i> | 6.29±0.37 <sup>b</sup>  | 6.65±0.36 <sup>a</sup> | 6.66±0.25 <sup>a</sup> | 5.53±0.41 <sup>c</sup>  | 6.72±0.29 <sup>a</sup>  | 5.46±0.47 <sup>c</sup>  | 5.48±0.47 <sup>c</sup>  |
|            | Yeast Mold               | 5.54±0.42 <sup>c</sup>  | 5.07±0.52 <sup>d</sup> | 6.09±0.34 <sup>b</sup> | 5.25±0.40 <sup>c</sup>  | 6.58±0.59 <sup>a</sup>  | 6.32±0.41 <sup>ab</sup> | 6.36±0.42 <sup>ab</sup> |
| 3. group   | <i>S. aureus</i>         | 6.38±0.37 <sup>a</sup>  | 5.33±0.35 <sup>b</sup> | 5.26±0.40 <sup>b</sup> | <1.0                    | <1.0                    | <1.0                    | <1.0                    |
|            | TMAB                     | 6.89±0.35 <sup>ab</sup> | 7.21±0.43 <sup>a</sup> | 7.24±0.26 <sup>a</sup> | 5.80±0.37 <sup>c</sup>  | 6.72±0.76 <sup>bc</sup> | 6.22±0.60 <sup>dc</sup> | 6.36±0.41 <sup>cd</sup> |
|            | TAMP                     | 6.51±0.36 <sup>ab</sup> | 6.22±0.38 <sup>b</sup> | 6.78±0.32 <sup>a</sup> | 5.08±0.44 <sup>c</sup>  | 6.31±0.48 <sup>b</sup>  | 5.25±0.44 <sup>c</sup>  | 5.23±0.44 <sup>c</sup>  |
|            | <i>Lactobacillus spp</i> | 6.30±0.30 <sup>b</sup>  | 6.78±0.35 <sup>a</sup> | 7.03±0.31 <sup>a</sup> | 5.61±0.38 <sup>c</sup>  | 6.79±0.51 <sup>a</sup>  | 5.42±0.34 <sup>c</sup>  | 5.53±0.36 <sup>c</sup>  |
|            | Yeast Mold               | 5.57±0.42 <sup>b</sup>  | 5.06±0.38 <sup>c</sup> | 6.03±0.32 <sup>a</sup> | 5.20±0.28 <sup>bc</sup> | 6.46±0.83 <sup>a</sup>  | 6.32±0.36 <sup>a</sup>  | 6.36±0.45 <sup>a</sup>  |
| 4. group   | <i>E. coli O157:H7</i>   | 6.48±0.37 <sup>a</sup>  | 5.72±0.36 <sup>a</sup> | 1.48±2.03 <sup>b</sup> | <1.0                    | <1.0                    | <1.0                    | <1.0                    |
|            | <i>L. monocytogenes</i>  | 6.38±0.34 <sup>a</sup>  | 5.17±0.53 <sup>b</sup> | 3.05±1.71 <sup>c</sup> | <1.0                    | <1.0                    | <1.0                    | <1.0                    |
|            | <i>S. aureus</i>         | 6.39±0.32 <sup>a</sup>  | 5.80±0.41 <sup>b</sup> | 5.55±0.42 <sup>b</sup> | <1.0                    | <1.0                    | <1.0                    | <1.0                    |
|            | TMAB                     | 9.29±0.13 <sup>a</sup>  | 9.01±0.40 <sup>a</sup> | 8.33±0.3 <sup>b</sup>  | 6.44±0.35 <sup>c</sup>  | 6.47±0.40 <sup>c</sup>  | 6.32±0.63 <sup>c</sup>  | 6.49±0.32 <sup>c</sup>  |
|            | TAMP                     | 8.22±0.11 <sup>a</sup>  | 8.46±0.49 <sup>a</sup> | 8.03±0.09 <sup>a</sup> | 5.36±0.42 <sup>c</sup>  | 6.27±0.39 <sup>b</sup>  | 5.30±0.30 <sup>c</sup>  | 5.19±0.43 <sup>c</sup>  |
|            | <i>Lactobacillus spp</i> | 5.98±0.13 <sup>b</sup>  | 6.81±0.42 <sup>a</sup> | 7.05±0.14 <sup>a</sup> | 5.67±0.29 <sup>bc</sup> | 6.73±0.45 <sup>a</sup>  | 5.35±0.33 <sup>c</sup>  | 5.50±0.47 <sup>c</sup>  |
| Yeast Mold | 4.75±0.49 <sup>e</sup>   | 4.67±0.38 <sup>e</sup>  | 5.77±0.38 <sup>c</sup> | 5.27±0.29 <sup>d</sup> | 6.53±0.31 <sup>a</sup>  | 6.01±0.26 <sup>bc</sup> | 6.29±0.38 <sup>ab</sup> |                         |

a, b, c, d, e: Differences between means with different letters in the same row are statistically significant. (p&lt;0.05)

**Table 4.** Physico-chemical changes during fermentation in experimentally prepared koumiss samples.

| Groups                           | Parameters                       | Times                   |                         |                         |                         |                         |                         |                         |
|----------------------------------|----------------------------------|-------------------------|-------------------------|-------------------------|-------------------------|-------------------------|-------------------------|-------------------------|
|                                  |                                  | 1.hour                  | 5. hour                 | 24 hour                 | 2. day                  | 3. day                  | 4. day                  | 5. day                  |
| 1.group                          | pH                               | 5.03±0.48 <sup>a</sup>  | 4.76±0.41 <sup>b</sup>  | 3.95±0.17 <sup>c</sup>  | 3.70±0.04 <sup>d</sup>  | 3.74±0.08 <sup>cd</sup> | 3.69±0.05 <sup>d</sup>  | 3.68±0.06 <sup>d</sup>  |
|                                  | <b>Titrateable acidity (%LA)</b> | 0.38±0.01 <sup>g</sup>  | 0.67±0.05 <sup>f</sup>  | 1.54±0.03 <sup>e</sup>  | 1.66±0.18 <sup>d</sup>  | 2.05±0.03 <sup>c</sup>  | 2.44±0.03 <sup>b</sup>  | 2.57±0.03 <sup>a</sup>  |
|                                  | <b>Dry matter (%)</b>            | 10.90±0.18 <sup>a</sup> | 10.91±0.25 <sup>a</sup> | 10.51±0.26 <sup>b</sup> | 10.43±0.29 <sup>b</sup> | 10.43±0.31 <sup>b</sup> | 10.42±0.26 <sup>b</sup> | 10.41±0.27 <sup>b</sup> |
|                                  | <b>Protein (%)</b>               | 2.39±0.14 <sup>a</sup>  | 2.38±0.14 <sup>a</sup>  | 2.12±0.02 <sup>b</sup>  | 2.12±0.05 <sup>b</sup>  | 2.12±0.02 <sup>b</sup>  | 2.12±0.03 <sup>b</sup>  | 2.08±0.05 <sup>b</sup>  |
|                                  | <b>Ash (%)</b>                   | 0.30±0.05 <sup>a</sup>  | 0.30±0.05 <sup>a</sup>  | 0.30±0.05 <sup>a</sup>  | 0.29±0.03 <sup>a</sup>  | 0.29±0.03 <sup>a</sup>  | 0.30±0.04 <sup>a</sup>  | 0.30±0.02 <sup>a</sup>  |
|                                  | <b>Alcohol (%)</b>               | 0.30±0.06 <sup>f</sup>  | 0.51±0.10 <sup>e</sup>  | 1.77±0.21 <sup>d</sup>  | 1.82±0.15 <sup>bc</sup> | 1.95±0.15 <sup>c</sup>  | 2.90±0.14 <sup>b</sup>  | 3.05±0.13 <sup>a</sup>  |
|                                  | 2.group                          | pH                      | 5.05±0.56 <sup>a</sup>  | 4.83±0.35 <sup>a</sup>  | 3.90±0.09 <sup>b</sup>  | 3.71±0.04 <sup>b</sup>  | 3.73±0.05 <sup>b</sup>  | 3.69±0.02 <sup>b</sup>  |
| <b>Titrateable acidity (%LA)</b> |                                  | 0.38±0.01 <sup>g</sup>  | 0.67±0.03 <sup>f</sup>  | 1.52±0.03 <sup>e</sup>  | 1.69±0.04 <sup>d</sup>  | 2.05±0.04 <sup>c</sup>  | 2.45±0.03 <sup>b</sup>  | 2.56±0.02 <sup>a</sup>  |
| <b>Dry matter (%)</b>            |                                  | 10.71±0.29 <sup>a</sup> | 10.85±0.24 <sup>a</sup> | 10.41±0.27 <sup>b</sup> | 10.46±0.27 <sup>b</sup> | 10.45±0.28 <sup>b</sup> | 10.42±0.19 <sup>b</sup> | 10.41±0.23 <sup>b</sup> |
| <b>Protein (%)</b>               |                                  | 2.36±0.13 <sup>a</sup>  | 2.41±0.13 <sup>a</sup>  | 2.12±0.02 <sup>b</sup>  | 2.09±0.03 <sup>b</sup>  | 2.12±0.03 <sup>b</sup>  | 2.11±0.01 <sup>b</sup>  | 2.11±0.02 <sup>b</sup>  |
| <b>Alcohol (%)</b>               |                                  | 0.30±0.04 <sup>f</sup>  | 0.54±0.05 <sup>e</sup>  | 1.77±0.12 <sup>d</sup>  | 1.83±0.12 <sup>d</sup>  | 1.96±0.11 <sup>c</sup>  | 2.93±0.09 <sup>b</sup>  | 3.08±0.11 <sup>a</sup>  |
| <b>Ash (%)</b>                   |                                  | 0.31±0.04 <sup>a</sup>  | 0.31±0.04 <sup>a</sup>  | 0.30±0.04 <sup>a</sup>  | 0.30±0.02 <sup>a</sup>  | 0.30±0.03 <sup>a</sup>  | 0.29±0.03 <sup>a</sup>  | 0.30±0.03 <sup>a</sup>  |
| 3.group                          |                                  | pH                      | 5.03±0.52 <sup>a</sup>  | 4.80±0.35 <sup>b</sup>  | 3.94±0.11 <sup>c</sup>  | 3.71±0.03 <sup>cd</sup> | 3.73±0.06 <sup>cd</sup> | 3.69±0.03 <sup>d</sup>  |
|                                  | <b>Titrateable acidity (%LA)</b> | 0.38±0.01 <sup>g</sup>  | 0.66±0.03 <sup>f</sup>  | 1.53±0.04 <sup>e</sup>  | 1.65±0.17 <sup>d</sup>  | 2.04±0.03 <sup>c</sup>  | 2.44±0.02 <sup>b</sup>  | 2.58±0.02 <sup>a</sup>  |
|                                  | <b>Dry matter (%)</b>            | 10.79±0.25 <sup>a</sup> | 10.87±0.26 <sup>a</sup> | 10.41±0.28 <sup>b</sup> | 10.46±0.27 <sup>b</sup> | 10.43±0.26 <sup>b</sup> | 10.44±0.23 <sup>b</sup> | 10.39±0.27 <sup>b</sup> |
|                                  | <b>Protein (%)</b>               | 2.35±0.15 <sup>b</sup>  | 2.44±0.10 <sup>a</sup>  | 2.13±0.02 <sup>c</sup>  | 2.11±0.04 <sup>c</sup>  | 2.12±0.03 <sup>c</sup>  | 2.12±0.02 <sup>c</sup>  | 2.09±0.04 <sup>c</sup>  |
|                                  | <b>Alcohol (%)</b>               | 0.30±0.04 <sup>f</sup>  | 0.54±0.08 <sup>e</sup>  | 1.77±0.15 <sup>d</sup>  | 1.82±0.15 <sup>d</sup>  | 1.98±0.10 <sup>c</sup>  | 2.93±0.09 <sup>b</sup>  | 3.06±0.10 <sup>a</sup>  |
|                                  | <b>Ash (%)</b>                   | 0.31±0.04 <sup>a</sup>  | 0.31±0.05 <sup>a</sup>  | 0.30±0.04 <sup>a</sup>  | 0.30±0.02 <sup>a</sup>  | 0.30±0.03 <sup>a</sup>  | 0.29±0.03 <sup>a</sup>  | 0.29±0.03 <sup>a</sup>  |
|                                  | 4.group                          | pH                      | 5.07±0.28 <sup>a</sup>  | 4.79±0.14 <sup>b</sup>  | 3.90±0.12 <sup>c</sup>  | 3.71±0.04 <sup>d</sup>  | 3.70±0.02 <sup>d</sup>  | 3.69±0.04 <sup>d</sup>  |
| <b>Titrateable acidity (%LA)</b> |                                  | 0.38±0.01 <sup>c</sup>  | 0.65±0.03 <sup>d</sup>  | 1.51±0.03 <sup>c</sup>  | 1.59±0.24 <sup>c</sup>  | 2.04±0.02 <sup>b</sup>  | 2.45±0.01 <sup>a</sup>  | 2.57±0.02 <sup>a</sup>  |
| <b>Dry matter (%)</b>            |                                  | 10.84±0.21 <sup>a</sup> | 10.90±0.19 <sup>a</sup> | 10.46±0.17 <sup>b</sup> | 10.28±0.26 <sup>b</sup> | 10.44±0.10 <sup>b</sup> | 10.41±0.22 <sup>b</sup> | 10.22±0.25 <sup>b</sup> |
| <b>Protein (%)</b>               |                                  | 2.40±0.11 <sup>b</sup>  | 2.48±0.03 <sup>a</sup>  | 2.11±0.02 <sup>c</sup>  | 2.10±0.03 <sup>c</sup>  | 2.12±0.03 <sup>c</sup>  | 2.12±0.02 <sup>c</sup>  | 2.09±0.02 <sup>c</sup>  |
| <b>Alcohol (%)</b>               |                                  | 0.31±0.05 <sup>g</sup>  | 0.59±0.04 <sup>f</sup>  | 1.86±0.14 <sup>e</sup>  | 1.73±0.13 <sup>d</sup>  | 2.02±0.08 <sup>c</sup>  | 2.92±0.08 <sup>b</sup>  | 3.09±0.10 <sup>a</sup>  |
| <b>Ash (%)</b>                   |                                  | 0.31±0.02 <sup>a</sup>  | 0.31±0.01 <sup>ab</sup> | 0.29±0.01 <sup>b</sup>  | 0.31±0.01 <sup>ab</sup> | 0.30±0.02 <sup>ab</sup> | 0.31±0.01 <sup>ab</sup> | 0.30±0.01 <sup>ab</sup> |

a, b, c, d: Differences between means with different letters in the same row are statistically significant. (p<0.05)

Table 5 illustrates the relationship between the microbiological and chemical attributes of koumiss within the experimental groups and the quantities of *E. coli O157:H7*. Among the koumiss samples, a positive correlation surfaced between the *E. coli O157:H7* count and the enumerations of *L. monocytogenes*, *S. aureus*, TMAB, TPAB, *Lactobacillus* spp., pH ratio, dry matter, and protein content. Conversely, a negative correlation was evident between the yeast mold count, alcohol content, and titratable acidity ( $p < 0.01$ ).

**Table 5.** Correlation of *E. coli O157:H7* numbers with microbiological and chemical properties of koumiss in experimental groups.

|                                 | r value  |          |
|---------------------------------|----------|----------|
|                                 | 1. Group | 4. Group |
| <i>Escherichia coli O157:H7</i> | 1        | 1        |
| <i>Listeria monocytogenes</i>   | -        | +0.936** |
| <i>Staphylococcus aureus</i>    | -        | +0.833** |
| TMAB                            | +0.389** | +0.865** |
| TPAB                            | +0.552** | +0.803** |
| <i>Lactobacillus</i> spp        | +0.246*  | +0.273   |
| Yeast mold count                | -0.510** | -0.778** |
| pH                              | +0.840** | +0.963** |
| Titratable acidity (%LA)        | -0.891** | -0.887** |
| Dry matter (%)                  | +0.610** | +0.709** |
| Alcohol (%)                     | -0.846** | -0.861** |
| Protein (%)                     | +0.765** | +0.877** |
| Ash (%)                         | -0.009   | +0.279   |

\* $p < 0.05$ , \*\* $p < 0.01$  significant

Table 6 provides an overview of the relationship between koumiss microbiological and chemical attributes within the experimental groups and the quantities of *L. monocytogenes*. In the koumiss samples, a positive correlation emerged between the count of *L. monocytogenes* and the enumerations of *E. coli O157:H7*, *S. aureus*, TMAB, TPAB, *Lactobacillus* spp., pH ratio, dry matter, ash content, and protein content. Conversely, a negative correlation was evident between the yeast mold count, alcohol content, and titratable acidity ( $p < 0.01$ ).

**Table 6.** Correlation of the number of *Listeria monocytogenes* to microbiological and chemical properties of koumiss in experimental groups.

|                                 | r value  |          |
|---------------------------------|----------|----------|
|                                 | 2.Group  | 4.Group  |
| <i>Escherichia coli O157:H7</i> | -        | +0.936** |
| <i>Listeria monocytogenes</i>   | 1        | 1        |
| <i>Staphylococcus aureus</i>    | -        | +0.913** |
| TMAB                            | +0.529** | +0.924** |
| TPAB                            | +0.546** | +0.868** |
| <i>Lactobacillus</i> spp        | +0.435** | +0.376*  |
| Yeast mold count                | -0.451** | -0.721** |
| pH                              | +837**   | +0.925** |
| Titratable acidity (%LA)        | -891**   | -0.893** |
| Dry matter (%)                  | +0.438** | +0.722** |
| Alcohol (%)                     | -0.853** | -0.856** |
| Protein (%)                     | +751**   | +0.824** |
| Ash (%)                         | +0.180** | +0.145   |

\* $p < 0.05$ , \*\* $p < 0.01$  significant

**Table 7.** Correlation of *Staphylococcus aureus* number to microbiological and chemical characteristics of koumiss in experimental groups.

|                                 | r value  |          |
|---------------------------------|----------|----------|
|                                 | 3.Group  | 4.Group  |
| <i>Escherichia coli O157:H7</i> | -        | +0.833** |
| <i>Listeria monocytogenes</i>   | -        | +0.913** |
| <i>Staphylococcus aureus</i>    | 1        | 1        |
| TMAB                            | +0.573** | +0.943** |
| TPAB                            | +0.632** | +0.930** |
| <i>Lactobacillus</i> spp.       | +0.537** | +0.499** |
| Yeast mold                      | -0.418** | -0.675** |
| pH                              | +0.771** | +0.818** |
| Titratable acidity (%LA)        | -0.884** | -0.872** |
| Dry matter (%)                  | +0.420** | +0.650** |
| Alcohol (%)                     | -0.832** | -0.818** |
| Protein (%)                     | +0.670** | +0.728** |
| Ash (%)                         | +0.099   | +0.040   |

\* $p < 0.05$ , \*\* $p < 0.01$  significant

The correlations between the microbiological and chemical attributes of koumiss within the experimental groups and the counts of *Staphylococcus aureus* are depicted in Table 7. Among the koumiss samples, a positive correlation surfaced between the quantity of *Staphylococcus aureus* and the quantities of *Escherichia coli O157:H7*, *Listeria monocytogenes*, TMAB, TPAB, *Lactobacillus* spp., pH ratio, dry matter, ash content, and protein content. Simultaneously, a negative correlation was apparent between the count of yeast molds, alcohol content, and titratable acidity ( $p < 0.01$ ).

#### 4. Discussion

Koumiss is a fermented product traditionally made from unpasteurized mare's milk. Research has investigated various physicochemical and microbiological properties of mare's milk and koumiss. It is believed that factors such as the season in which the milk is obtained, the animal breeds involved, the age of the mare, the lactation period, varied feed compositions, starter cultures, paddock, and milking conditions, as well as the incubation period and temperature, can all differ and influence the final product.

Several types of microorganisms were found in koumiss samples by Tegin [29]. These included TMAB counts ranging from  $5.16 \pm 0.009$  to  $7.05 \pm 0.011$  log<sub>10</sub> CFU/mL, yeast mold counts ranging from  $4.53 \pm 0.009$  to  $6.83 \pm 0.006$  log<sub>10</sub> CFU/mL, lactic acid bacteria count ranging from  $5.13 \pm 0.026$  to  $7.10 \pm 0.004$  log<sub>10</sub> CFU/mL, and staphylococci-micrococci group microorganisms ranging from  $0.77 \pm 0.249$  to  $4.17 \pm 0.044$  log<sub>10</sub> CFU/mL. The values noted by the researcher were consistent with those determined in this study for koumiss used as a starter culture. Out of the 25 samples used in Tegin's study, only one contained a coliform group microorganism detected at a level of  $1.26 \pm 0.089$  log<sub>10</sub> CFU/mL. In contrast, this study did not detect coliform group microorganisms using koumiss as a starter culture.

Chaves-López et al. [30] reported that Colombian koumiss

produced from cow's milk contained lactic acid bacteria at levels of 7.05–9.53 log<sub>10</sub> CFU/mL and yeast at levels of 6.26–8.65 log<sub>10</sub> CFU/mL. This study observed that the koumiss used as a starter culture had counts close to those of lactic acid bacteria and yeast mold. Similarly, Mu et al. [31] found yeast counts in Chinese koumiss samples to be in the range of 5–7 log<sub>10</sub> CFU/mL.

This study demonstrated a similar yeast mold count in koumiss used as a starter culture. During the experimental period, the pH of koumiss produced from mare's milk decreased steadily until the end of the 5th day of fermentation, when the analyses were conducted. This finding aligns with previous studies where a reduction in pH was a natural outcome of the fermentation process [22, 32-35]. It was observed that the growth of *Escherichia coli* O157:H7, *S. aureus*, and *L. monocytogenes* was significantly inhibited, particularly with a decrease in pH ( $p < 0.01$ ).

In the koumiss samples, there was a clear positive correlation between pH and the tested pathogenic microorganisms. This correlation showed that as the pH value decreased, the number of pathogenic microorganisms also decreased in all four groups. *E. coli* O157:H7 and *L. monocytogenes* also showed no growth in analyses performed on the second day. However, *S. aureus* showed no growth on the third day. The titratable acidity of the experimental koumiss samples increased at the end of the fermentation period. This finding was consistent with previous studies [22, 29, 32, 33, 36].

The increase in titratable acidity can be caused by Lacto-fermentation, which also showed a negative effect on *E. coli* O157:H7, *S. aureus* and *L. monocytogenes* numbers ( $p < 0.01$ ). There was a negative correlation between the titratable acidity and the pathogenic microorganisms. An increase in the titratable acidity decreased the number of pathogenic microorganisms in all groups. Also, fermentation time showed a clear ( $p < 0.05$ ) influence on protein content. This finding is consistent with the previous studies [22, 32, 33]. Proteolysis during fermentation may have caused the reduction in the protein content. Additionally, the study noted a decrease in the dry matter content after fermentation, which aligned with findings from various studies, including [22, 33, 36, 37]. The starter culture's fermentation caused this decrease in dry matter content.

The impact of fermentation time on ash content in experimentally produced koumiss samples from mare's milk was not deemed significant ( $p > 0.05$ ). Likewise, the effect of ash content on the tested pathogens did not yield statistical significance. The ash content recorded in this study is consistent with values reported by various researchers [37, 38].

Table 4 demonstrates a consistent rise in alcohol content throughout the incubation period of koumiss ( $p < 0.05$ ). This increase in alcohol content during koumiss fermentation is consistent with findings from multiple studies [12, 22, 34].

Notably, the reductionary impact of alcohol content on the tested pathogens was statistically significant across all four groups ( $p < 0.01$ ). The determined alcohol content in this study was 3.05±0.13 in the 1st group, 3.08±0.11 in the 2nd group, 3.06±0.10 in the 3rd group, and 3.09 in the 4th group. The variation in alcohol content outcomes among different studies may be predominantly attributed to varying incubation periods.

In the koumiss experimentally produced from mare's milk, the TMAB count closely aligned with the values reported by Tegin's study [29]. The impact of fermentation duration on the TMAB count within koumiss proved significant in this study ( $p < 0.05$ ). The reduction in TMAB count observed by the end of the second day is attributed to the suppression of certain microorganisms' growth within the starter cultures. This phenomenon is linked to increased titratable acidity, elevated alcohol content, and diminished pH. In all three groups, the analyses on the fourth and fifth days indicated a partial stabilization in the increase TMAB levels, first observed at the end of the third day. This augmentation in TMAB count on the third day is attributed to the growth and flourishing of dominant species resilient to variations in the physicochemical properties of koumiss.

The quantity of *Lactobacillus* spp. detected in this study corresponded with previous research [22,29,34]. Table 4 illustrates the count of *Lactobacillus* spp. across all four groups. However, it decreased on the second day, followed by an increase on the third day, only to decline on the fourth and fifth days. The growth and proliferation of dominant species could be the cause of this elevation in the *Lactobacillus* spp. count. These hardy species are adaptable to fluctuations in koumiss's physicochemical properties, taking the place of suppressed strains. Notably, studies have reported that *L. plantarum* strains isolated from koumiss exhibit antibacterial effects against *E. coli* and *L. innocua* [35]. Similarly, Zhang et al. [39]. noted that *L. casei* Zhang, obtained from koumiss, demonstrated antibacterial properties against *E. coli*, *Escherichia coli* O157:H7, and K88. Another study showed that *L. plantarum* LB-B1 pediocin, which was taken from koumiss, could stop the growth of *Listeria*, *Lactobacillus*, *Streptococcus*, *Enterococcus*, *Pediococcus*, and *Escherichia*, even stopping *L. monocytogenes* [40].

Yinfeng et al. [41] reported that starter cultures present in koumiss had an inhibitory effect on *Listeria* spp., *S. aureus*, and *E. coli* growth. Ren et al. [42] documented that oral administration of *L. paracasei*, isolated from koumiss to *E. coli*-infected diarrheal mice treated and prevented *E. coli*-induced diarrhea, suggesting that koumiss might enhance immunity by improving gut microbiota. Similarly, Sanam et al. [43] reported that *Lactobacilli* isolated from mare's milk inhibited *S. aureus*, *E. coli*, and *Bacillus cereus*. These outcomes parallel the findings of the present study. Furthermore, Yinfeng et al. [41] mentioned that nine strains of isolated *Lactococcus* and 12 strains of *Lactobacillus* from koumiss had inhibitory effects on *Listeria* spp. but lacked a

preventive effect on *E. coli* and *S. aureus*. While their observations regarding *Listeria* are consistent with the findings of this study, their claims of effects on *E. coli* and *S. aureus* do not align. The observed yeast and mold count in the experiments had a significant impact on the number of pathogenic microorganisms ( $p < 0.01$ ). A negative correlation was evident between the yeast mold count and the examined pathogenic microorganisms, suggesting that higher yeast mold counts correlated with decreased pathogenic microorganism counts across all four groups.

Chen et al. [44]. reported that *Saccharomyces cerevisiae* isolated from koumiss contained antibacterial compounds, which hindered *E. coli* O8 growth and replication by affecting its cell surface. Another study found that yeasts like *S. cerevisiae* and *Kluyveromyces marxianus* in koumiss starter cultures had antibacterial properties that kept mice from getting *E. coli* infections [45]. These findings resonate with the outcomes of the present study. Additionally, Yinfeng et al. [41] noted that four yeast strains isolated from koumiss had a preventive effect on *E. coli*, with two of these yeast strains also showing a preventive effect on *S. aureus*. However, they reported that the yeast strains had no inhibitory effect on *Listeria*.

## 5. Conclusion

The study involved inoculating raw mare's milk with *E. coli* O157:H7 ATCC 43894, *L. monocytogenes* ATCC 7644, and *S. aureus* NCTC 10654 at a  $10^6$  CFU/mL concentration. Experimental groups were established using a 20% proportion of koumiss as a starter culture and were then incubated at 25°C. A decline in the count of pathogenic microorganisms was observed at the 5th and 24th hours within the experimental groups. Over the 2nd, 3rd, 4th, and 5th days, the tested pathogenic microorganisms' counts dropped to undetectable levels. The study unveiled a positive correlation between the rate of pH reduction and the initial concentration of inoculated pathogenic microorganisms at  $10^6$  CFU/mL.

In contrast, a negative correlation was identified between titratable acidity and alcohol content. Notably, the reduction in pathogenic microorganism counts in koumiss samples during experimentation, followed by their subsequent decline to undetectable levels, was attributed to pH reduction, increased titratable acidity, and heightened alcohol content. Consequently, the research suggests that koumiss produced from raw mare's milk and incubated at 25°C could potentially harbor pathogenic microorganisms up until the second day. The study also indicated that raw mare's milk possessed favorable microbiological quality. However, considering that raw mare's milk is consumed for therapeutic purposes, it is imperative to recognize that neglecting hygiene practices during milking and using milk from diseased mares could lead to serious health issues and negatively impact public health. Likewise, sensitizing farmers to use utilize high-quality milk for koumiss production and providing education on hygiene and sanitation practices would be prudent. It is understood that

further comprehensive investigations are necessary to ensure standardized koumiss production and to determine its treatment and therapeutic attributes.

## REFERENCES

- [1]. Afzaal, M., Saeed, F., Anjum, F., Waris, N., Husaain, M., Ikram, A., Ateeq, H., & Suleria, H., Nutritional and ethnomedicinal scenario of koumiss: A concurrent review, *Food Science & Nutrition*, 911, (2021), 6421-6428.
- [2]. Yerlikaya, O., Starter cultures used in probiotic dairy product preparation and popular probiotic dairy drinks, *Food Science & Technology*, 34, (2014), 221-229.
- [3]. Widyastuti, Y., & Febrisiantosa, A., The role of lactic acid bacteria in milk fermentation, *Food & Nutrition Science*, 5, (2014), 435-442.
- [4]. Kirdar, S. S. (2021) Therapeutics Effects and Health Benefits of the Caucasus Koumiss: A Review. *Annual Research & Review in Biology*, 36 (11). pp. 47-56.
- [5]. Mazhitova, A. T., & Kulmyrzaev, A. A., Determination of amino acid profile of mare milk produced in the highlands of the Kyrgyz Republic during the milking season, *Journal of Dairy Science*, 99(4), (2016), 2480-2487.
- [6]. Rakhmanova, A., Wang, T., Xing, G., Ma, L., Hong, Y., Lu, Y., Xin, L., Xin, W., Zhu, Q., & Lü, X., Isolation and identification of microorganisms in Kazakhstan koumiss and their application in preparing cow-milk koumiss, *Journal of Dairy Science*, 104(1), (2021), 151-166.
- [7]. Yu, J., Xia, Y., Qiao, X., Jin, Z., Li, P., Wang, R., Wang, Y., & Shuang, Q., Analysis of flavor substances and microbial diversity in natural starter of koumiss in Xilin Gol pastoral area, *Science & Technology of Food Industry*, 42, (2021), 112-121.
- [8]. Dugan, F. M., Fermentative microorganisms in the prehistory of Europe, the steppes, and Indo-Iranian Asia and their contemporary use in traditional and probiotic beverages, *Fungi*, 2, (2009), 16-39.
- [9]. Ringø, E., Andersen, R., Sperstad, S., Zhou, Z., Ren, P., Breines, E., Hareide, E., Yttergård, G. J., Opsal, K., Johansen, H. M., Andreassen, A. K., Kousha, A., Godfroid, J., & Holzapfel, W., Bacterial community of koumiss from Mongolia investigated by culture and culture-independent methods, *Food Biotechnology*, 284, (2014), 333-353.
- [10]. Meng, Y., Chen, X., Sun, Z., Li, Y., Chen, D., Fang, S., & Chen, J., Exploring core microbiota responsible for the production of volatile flavor compounds during the traditional fermentation of koumiss, *LWT - Food Science and Technology*, 135, (2021), 110049.
- [11]. Tegin, R., & Gonulalan, Z., All aspects of koumiss the natural fermented product, *MANAS Journal of Engineering*, 2, (2014), 23-34.

- [12]. Karacil, M. S., & Tek, N. A., Fermented products produced in the world: Historical process and relationships with health, *Uludag University Journal of Agricultural Faculty*, 27, (2013), 163-173.
- [13]. Erdem, B., & Gundogdu, I., Koumiss treatment in the context of health tourism: A research in Kyrgyzstan, *International Journal of Medical Research & Health Sciences*, 7(11), (2018), 135-155.
- [14]. Erdem, B., & Gündoğdu, İ., An investigation on koumiss treatment in the context of health tourism: A literature review, *Turizam*, 22(3), (2018), 107-120.
- [15]. Сагынбаева, Б., Концепт "Кумыс" в кыргызском мировоззрении, *Наука, новые технологии и инновации Кыргызстана*, (2), (2017), 198-201.
- [16]. Li, Q., Zhang, C., Xilin, T., Ji, M., Meng, X., Zhao, Y., Siqin, B., Zhang, N., & Li, M., Effects of koumiss on intestinal immune modulation in immunosuppressed rats, *Frontiers in Nutrition*, 9, (2022), 765499.
- [17]. Yangilar, F., Oğuzhan, P., & Çelik, P., Koumiss, an unique drink, *Ege University Journal of Food Technology*, 6, (2013), 123-134.
- [18]. Avreljo, D., Baban, M., Mijic, P., Antunovic, Z., Ernoic, M., & Antunovic, B., Possibilities for production and consumption of mare's milk, *KRMIVA*, 51, (2010), 343-350.
- [19]. Metin M. Dairy Technology. 7th Edition. Ege University Press, Izmir, 2008.
- [20]. Kırdar, S.S., Tegin, R.A.A., (2022). Chapter 7. Koumiss-Areview of History, processing condition, functional properties and industrial application.144-168. In ed. Akkarishahabi, L. In *Contemporary Multidisciplinary technical research*.
- [21]. Baran A. 'The effect of brine concentration and ripening temperature on growth and toxin production of *Staphylococcus aureus* in white cheese' PhD thesis, Institute of Health Sciences, Department of Food Hygiene and Technology, Ataturk University, 2015.
- [22]. Küçükçetin A. 'Studies on the properties of the koumiss made from original mare's and whey powder added cow's and goat's' M. S. thesis, Institute of Science, Department of Food Engineering, Akdeniz University, 1999.
- [23]. Halkman A. K. & Sağdaş O. E. *Merck Microbiology Handbook*, 2nd Edition, Merck, 2011.
- [24]. Atlas, R. M., *Handbook of Microbiological Media For The Examination Of Food*, 2nd ed., CRC Press. 2006.
- [25]. National Microbiology Standards, IMVIC Tests, Standard No: B-TP-06, Ministry of Health, Republic of Turkey, 1-15. 2015.
- [26]. Erol İ. *Food Hygiene and Microbiology*, 1st Edition, Ankara: Pozitif Printing, 2007.
- [27]. Tekinşen O., Atasever M., Keles A., & Tekinsen K. *Milk, Yogurt, Butter, Cheese Production, and Quality Control*, 1st Edition, Selcuk University Press, 2002.
- [28]. GOST 3629-47, Milk products. Method of alcohol determination: ГОСТ 3629-47. Молочные продукты. Метод определения спирта.
- [29]. Tegin R. 'Investigation of some chemical and microbiological properties of koumiss produced in the Narin region' M.S thesis, Department of Food Engineering, Institute of Natural Sciences, Kyrgyzstan-Turkey Manas University, 2012.
- [30]. Chaves-López, C., Serio, A., Martuscelli, M., Paparella, A., Osorio-Cadavid, E., & Suzzi, G., Microbiological characteristics of kumis, a traditional fermented Colombian milk, with particular emphasis on enterococci population, *Food Microbiology*, 28, (2011), 1041-1047.
- [31]. Mu, Z., Yang, X., & Yuan, H., Detection and identification of wild yeast in koumiss, *Food Microbiology*, 31, (2012), 301-308.
- [32]. Akpınar A. 'Identification of lactic acid bacteria and yeasts isolated from koumiss with different origins and production of koumiss with goat milk' PhD thesis, Institute of Science and Technology, Department of Dairy Technology, Ege University, 2015.
- [33]. Küçükçetin A. 'Studies on the properties of the koumiss made from original mare's milk and modified bovine milk using membrane technologies' PhD thesis, Institute of Science, Department of Food Engineering, Akdeniz University, 2003.
- [34]. Küçükçetin, A., Yaygin, H., Hinrichs, J., & Kulozik, U., Adaptation of bovine milk towards mare's milk composition by means of membrane technology for koumiss manufacture, *International Dairy Journal*, 13, (2003), 945-951.
- [35]. Wang, H., Shi, J., Zhang, H., & Qi, W., A survey of some antifungal properties of lactic acid bacteria isolates from koumiss in China, *SDT*, 64, (2011), 585-590.
- [36]. Topuz O. K. 'Studies on the properties of the koumiss made from original mare's milk using traditional and different starter cultures' M.S. thesis, Institute of Natural Sciences, Department of Food Engineering, Akdeniz University, 2005.
- [37]. Kınık, Ö., Akalın, S., & Gönç, S., Kımız üretimi ve özellikleri üzerinde bir araştırma, *Gıda / The Journal Of Food*, 25, (2000), 379-384.
- [38]. Chen, Y., Wang, Z., Chen, X., Liu, Y., Zhang, H., & Sun, T., Identification of angiotensin I-converting enzyme inhibitory peptides from koumiss, a traditional fermented mare's milk, *Journal of Dairy Science*, 93, (2010), 884-892.
- [39]. Zhang, H. P., Zhang, Q. J., Ren, G. Q., & Bao, Q. H., The antagonism of *Lactobacillus casei* Zhang to pathogenic *Escherichia coli* in mice and the influence on the microbial

- population in the gut, *Microbiology-Beijing*, 3, (2007), 63-68.
- [40]. Xie, Y., An, H., Hao, Y., Qin, Q., Huang, Y., Luo, Y., & Zhang, L., Characterization of an anti-listeria bacteriocin produced by *Lactobacillus plantarum* LB-B1 isolated from koumiss, a traditionally fermented dairy product from China, *Food Control*, 22, (2011), 1027-1031.
- [41]. Yinfeng, H., Shaoying, L., Zhishen, M., Liyun, W., Jie, S., Jing, W., & Meixia, Z., Isolation, identification and anti-bacteria function of microorganisms from koumiss, *Transactions of the Chinese Society of Agricultural Engineering*, 2, (2002), 91-95.
- [42]. Ren, S., Wang, C., Chen, A., Bai, Z., Tian, Y., & Lv, W., *Lactobacillus paracasei* influences the gut-microbiota-targeted metabolic modulation of the immune status of diarrheal mice, *Food & Function*, 14, (2023), 4368-4379.
- [43]. Sanam, M. U., Detha, A. I., & Rohi, N. K., Detection of antibacterial activity of lactic acid bacteria, isolated from Sumba mare's milk, against *Bacillus cereus*, *Staphylococcus aureus*, and *Escherichia coli*, *Journal of Advanced Veterinary and Animal Research*, 9(1), (2022), 53.
- [44]. Chen, Y., Wang, C., Hou, W., Wang, X., Gali, B., Huasai, S., Yang, S., Wu, A., Zhao, Y., Wu, Y., & Chen, A., Effects of antibacterial compounds produced by *Saccharomyces cerevisiae* in koumiss on pathogenic *Escherichia coli* O8 and its cell surface characteristics, *Journal of Integrative Agriculture*, 16, (2017), 742-748.
- [45]. Chen, Y., Aorigele, C., Wang, C., Simujide, H., & Yang, S., Screening and extracting mycocin secreted by yeast isolated from koumiss and their antibacterial effect, *Journal of Food & Nutrition Research*, 3, (2015), 52-56.

## Detection and Identification of Stuttering Types Using Siamese Network

Venera Adanova<sup>1\*</sup>, Maksat Atagoziev<sup>2</sup>

<sup>1</sup> Department of Computer Engineering, TED University, Ankara, 06420, Türkiye, [venera.adanova@tedu.edu.tr](mailto:venera.adanova@tedu.edu.tr), ORCID: 0000-0001-7247-0288

<sup>2</sup> Department of Computer Engineering, OSTIM Technical University, Ankara, 06374, Türkiye, [maksat.atagoziev@ostimtechnik.edu.tr](mailto:maksat.atagoziev@ostimtechnik.edu.tr), ORCID: 0000-0001-7799-7636

### ABSTRACT

Stuttering is a complex speech disorder characterized by disruptions in the fluency of verbal expression, often leading to challenges in communication for those affected. Accurate identification and classification of stuttering types can greatly benefit persons who stutter (PWS), especially in an era where voice technologies are becoming increasingly ubiquitous and integrated into daily life. In this work, we adapt a simple yet effective Siamese network architecture, known for its capability to learn from paired speech segments, to extract novel features from audio speech data. Our approach leverages these features to enhance the detection and identification of stuttering events. For our experiments, we rely on a subset of the SEP-28k stuttering dataset, initially implementing a single-task model and gradually evolving it into a more sophisticated multi-task model. Our results demonstrate that transitioning the network from a single-task learner to a multi-task learner, coupled with the integration of auxiliary classification heads, significantly improves the identification of stuttering types, even with a relatively small dataset.

### ARTICLE INFO

#### Research article

Received: 25.08.2024

Accepted: 04.12.2024

**Keywords:** Stuttering, dysfluency detection, multi-task learning

\*Corresponding author

### 1. Introduction

Stuttering, a.k.a. stammering, is a complex speech disorder that negatively affects the communication ability of 1% of the population. Persons who stutter (PWS) often know what they want to say, however the speech is interrupted by involuntary pauses and word or sound repetitions. Identification of stuttering in a speech is a challenging problem involving multiple disciplines such as pathology, psychology, acoustics, and signal processing.

With the advance of machine and deep learning the research done on speech domain have dramatically developed. Thus, current Automatic Speech Recognition (ASR) systems have good accuracy leading to voice assistants such as Alexa, Siri or Google. However, these systems are built based on fluent speech, and they fail to recognize

speech accompanied with pauses and repetitions. Considering that voice technologies are becoming ubiquitous, if the developers continue assuming ideal speech scenarios, the future world seems to be the place where people with speech disorders will feel greatly deprived.

The studies on the stuttered speech have gained a speed recently as Apple released SEP28k stuttering dataset[14]. The data was collected from podcast where PWS are interviewed and is the first largest annotated dataset.

In this work, we perform our experiments on the subset of SEP28k dataset. We build a simple single task model which learns to differentiate between stuttering types, and then gradually convert the model into multi-task learner with multiple heads. We then observe improvements that these transformations bring into the classification task.

## 2. Related Work

Though speech recognition systems have evolved dramatically over the last decade, with the development of machine and deep learning, there is a scarce number of studies involving stuttering detection and identification. The majority of studies conducted on stuttering data aim to detect and identify the dysfluency types in audio recordings. These types of dysfluency are generally defined as: blocks, prolongations, sound/word/phrase repetitions, and interjections [14, 18]. Blocks are defined as involuntary pauses before words. Prolongations are elongated syllable, like *I am s[sss]ory*. Repetitions involve sound, word or phrase repetitions. For example, *I made [made] dinner* represents a word repetition. In order to avoid above defined stuttering types a person who stutters learns to use filler words like *um, uh, you know, etc.* These filler words are known as interjections. Note that the dysfluency types might be named differently in different studies.

### 2.1. Datasets

The main reason for the deficiency of studies in stuttered speech is the lack of data. Just like any speech related problem, detecting stuttering requires lots of data for accurate learning. Typically, works conducted on stuttering detection and identification are done based on some datasets, either in-house or public, and learn to classify between fluent and dysfluent speech (stuttering detection), and distinguish dysfluency types (identification).

The works that use in-house datasets [1, 8, 9, 11, 15] collect their own data, label them manually and report the stuttering detection and identification accuracy based on their own data. This type of dataset is very small and is not shared publicly.

There is only a handful number of publicly available stuttering datasets. The very first and also the smallest one is the UCLASS dataset [10]. It contains 457 audio recordings of monologues, conversations and readings, and only small amount of them has transcriptions. The dataset is not labeled according to dysfluency types.

The FluencyBank dataset [16] contains audio and video files with transcriptions for the interviews conducted for 32 adults and children who stutter. However, the dataset is not labeled.

The scarcity of labeled data led to the creation of synthetic dataset LibriStutter [12], which consists of 50 speakers (approximately 20 hours). The dataset was generated by injecting random stuttering to LibriSpeech dataset, which consists of fluent speech. The audio signals were segmented into four-second windows, and for every window either one of the stuttering events, as sound, word and phrase repetitions, prolongations, and interjections, were injected, or left untouched.

The largest dataset, *Stuttering Events in Podcasts* (SEP-28k) was released recently by [14]. SEP-28k is the first publicly available annotated dataset. It contains about 28000 3-second clips from podcast recordings. The SEP28k corpus also has 4144 3-second annotated clips from the FluencyBank dataset. [6] subsequently introduced an extended SEP-28k, which contains also the gender and speaker information. Along with the extended data they proposed a possible partitioning of data into train and test set.

[4] suggest their own dataset namely, Kassel State of Fluency (KSoF), which consists of 5500 clips of stuttered speech in German. The clips were labeled with the six stuttering event types: blocks, prolongations, sound/word/phrase repetitions, interjections and speech modifications. The last type is therapy specific and indicates whether the speaker's speech is modified after the therapy. The dataset also has some metadata, like the gender of a speaker, therapy status, type of microphone used, etc.

### 2.2. Stuttering Identification

One of the studies that aimed to identify all dysfluency types in stuttered speech was conducted by [13]. The work was based on UCLASS and LibriStutter datasets. They build a deep neural network, named FluentNet, consisting of Squeeze-and-Excitation Residual Network and bidirectional LSTM. The four-second long audio clips from the dataset are converted to spectrograms using Short Time Fourier Transform (STFT), and these spectrograms formed the inputs to FluentNet. Though the work demonstrates promising results it has some limitations. The results were reported for the small subset of speakers, probably because they needed to label the data manually first. Also, the work does not consider fluent speech and their models learn to classify between stuttering types only. The other limitation is that they trained a model for every dysfluency type leading to computationally expensive system due to large number of parameters.

As an alternative to the FluentNet, [17] proposed their own time delay neural network, called StutterNet. The model was trained and tested on UCLASS. The audio recordings for over 100 speakers were manually labeled as in [13]. Only core behaviors (prolongations, blocks, and repetitions) and fluent part of the speech were considered. Each audio recording was sliced into four-second clips and for each clip mel-frequency cepstral coefficients (MFCCs) were computed. The MFCC features are then fed to StutterNet as features. In contrast to the aforementioned approach a single model was trained for identification of all types of dysfluency and a slight improvement was observed.

In [7] KSoF is used for stuttering detection. Each audio

recording is sliced into three-second clips. For each clip the features are extracted from pretrained wav2vec 2.0 [3] network. Wav2vec network is learned on large amount of fluent speech, and takes raw data as an input and produces a feature vector describing each audio data. In [7] before using the wav2vec features the network was fine-tuned using SEP-28k dataset. The features obtained from the fine-tuned network are subsequently fed to SVM model for dysfluency identification purposes.

The work in [19] reports on the dysfluency identification results based on multi-task and adversarial learning using SEP-28k dataset. Each clip in the dataset was represented by 20 MFCC features. Instead of learning a single task in the network, a multi-task learning was used. A network consists of three parts. First part learns to classify between fluent and dysfluent speech, second part learns to classify between dysfluency types, and the third part is just an auxiliary part which prevents the network from overfitting and learns to classify between show names from which the clips were taken. All three parts share a single encoder, meaning that they share weight in the encoder part.

[2] proposed automatic detection and correction for three types of dysfluencies: repetitions, prolongations and long pauses, using signal processing methods. In this research MFCCs and Linear Predictive Coefficients (LPC) are used to extract the features. The downside of this approach is that it largely relies on empirical thresholds to detect dysfluency types. Thus, to detect repetitions the MFCC and LPC features of consecutive words are extracted and their correlation factor is computed. If the correlation is above a certain threshold then the words are considered to be similar, and one of the words is deleted.

Another two approaches [1, 8] also use empirical threshold to detect prolongations in speech. These studies deal with detection and correction of prolongations and repetitions. To correct the prolongations, amplitudes of the audio signal are compared against predefined threshold value, and the values below that threshold are deleted. To detect repeated words the audio signal is first converted to text, in the text format the repeated words are detected and deleted. Subsequently, the text is converted back to speech.

### 3. Dataset

In our work, we use a subset of SEP28k. The audio data was collected from eight podcast shows and every episode was divided into 3 second clips. The total number of clips in the dataset is 28177 (approx. 23.5 hours) and every clip was annotated by three annotators. The annotations for every clip have two types: stuttering and non stuttering. Stuttering types include *prolongation*, *block*, *interjection*, *sound/word repetition* and *no stuttered word*, where former five types represent dys-

fluency types and the last one is the fluent type. Non stuttering types include *unintelligible*, *natural pause*, *unsure*, *music* and *poor audio quality*. We are mainly interested in the stuttering types.

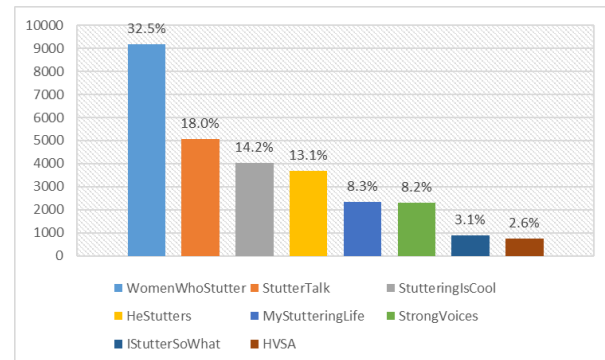


Figure 1: The distribution of podcast shows in the dataset. WomenWhoStutter and HeStutters have common host.

The SEP28k is a challenging dataset and these challenges come in three ways. First, it is highly imbalanced. More than half of the data contains fluent speech, and approximately 10% is given for a particular dysfluency type. Second, each clip might have several annotations. Thus, a single clip might contain both prolongation and block dysfluency types, while being also annotated by one of the annotators as a fluent speech. Lastly, it is also imbalanced in terms of speaker. Thus, host speech dominates 60% of the data. Also, the distribution of podcast shows is imbalanced as shown in Figure 1. The number of clips for one of the shows, Women Who Stutter, form 33% of overall clips. Considering that Women Who Stutter and He Stutters share the same host (Pamela Mertz), a large amount of clips is dominated by the speech of a single person.

As has been discussed previously, each clip in the dataset might have multiple labels. Typically, it is not clear how much the annotators should be trusted. For example, consider a clip where three annotators identify it as having prolongation, two annotators also note that some part of it has blocks, and one annotator states that it has no other disfluency. We do not know how much weight should be given to that single label. It might also be the case that each annotator votes for a different stuttering type, further increasing our confusion. All studies that have used this dataset have somehow neglected to mention their approach to dealing with these labels. We, on the other hand, decided to take a more cautious approach by constructing a smaller subset from SEP-28k, which we refer to as the confidence list. This list consists of clips that were consistently assigned a single type by all three annotators. However, the *interjection* type was never annotated alone, as it always co-occurs with the *no*

*stuttered word* type. Therefore, we also include clips where all three annotators selected both *no stuttered word* and *interjections*. Moreover, clips where all three annotators selected both *no stuttered word* and *natural pause* are also included. We also formed a confidence list for the FluencyBank dataset. However, only clips with disfluency types were included, as the percentage of fluent clips already constitutes a large portion of the dataset. In total, our dataset contains 3,901 clips, and the distribution of different types is illustrated in Fig. 2. It is important to note that the dataset is highly imbalanced, with 65% of the clips consisting of fluent speech.

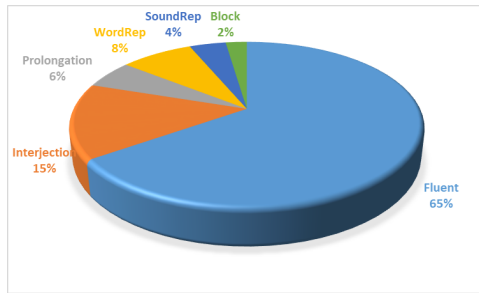


Figure 2: The distribution of stuttering types in our dataset. Observe that fluent data forms 65% of the dataset.

#### 4. Proposed Framework

Given the audio clips, we initially extract their Mel Frequency Cepstral Coefficients, MFCCs. The extracted MFCCs are further fed to our baseline model, training which we learn new embeddings (features) for the clips. The baseline model that we use to extract embeddings is the Siamese network with contrastive loss shown in Fig. 4(gray region). The choice of this network is not random, as we favor it because of its ability to learn well the data which consists of small number of representatives from each class. This is indeed the case for our data.

There are two inputs to the network and two identical subnetworks that share the weights. For each pair the two subnetworks produce embeddings which are then used to compute the Euclidean distance between a pair of inputs. The main goal of the network is not to learn to classify different stuttering types but to differentiate

between them.

The subnetwork consist of three blocks. Each block contains a convolutional layer followed by max pooling and dropout layers. The last layer does global averaging which returns the desired 64x1 dimensional vector. The details on input and output dimensions are illustrated in Fig. 3.

As a loss function for the baseline model we use contrastive loss which is defined as following:

$$L_{baseline} = y \cdot d^2 + (1 - y) \cdot \max(\text{margin} - d, 0)^2 \quad (1)$$

where,  $y$  is a true label, 1 if the audio pairs are of the same class, 0 otherwise, and  $d$  is the Euclidean distance between the outputs of twin network embeddings. Margin is 1.

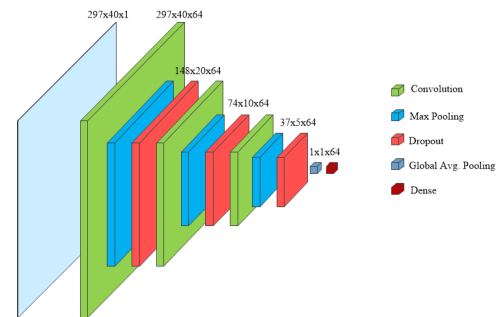


Figure 3: The architecture of our subnetwork.

Our baseline model does a single task learning (STL). During our experiments we extend the model to do multi task learning (MTL). Thus, we add a classification head to the model so that the model can also learn to classify between the six stuttering types. In our other experiment, we add another classification head, which also forces the network to differentiate between show types. These extension are shown in Fig. 4, where each of the classification heads is fed with the new features computed for the first input of the baseline model. For both of these classification heads we use sparse categorical crossentropy loss function. The addition of auxiliary tasks as this, are suggested in the literature [5, 19] for generalization and regularization purposes.

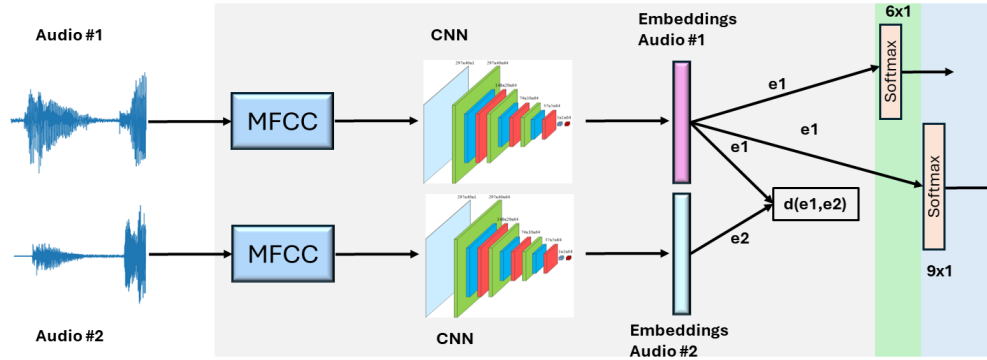


Figure 4: Proposed framework. The model within the gray box is the baseline model (BM). Then we add one classification head that learns to classify between six stuttering types (gray plus green regions) (BSM). The third model is formed by adding one more classification head to the second model (gray plus green plus blue regions), which also learns to classify shows (BSSM).

Hence, the overall loss of an MTL model is given by:

$$L = \lambda_{baseline} \cdot L_{baseline} + \lambda_{auxiliary} \cdot L_{auxiliary} \quad (2)$$

As was mentioned before, our model learns new features (embeddings) for the audio data, which are subsequently fed to machine learning models for classification purposes.

## 5. Experimental Results

### 5.1. Features

We first compute MFCC features for every audio clip, which are then fed to our model. All clips are read with the sampling frequency of 16000. The MFCC features are computed using *speechpy* library, with the frame length of 0.025, frame stride of 0.01 and number of filters of 40. For every 3 seconds long clip, using these parameters, we produce 297x40 features.

### 5.2. Data Augmentation

The data is highly imbalanced, so we produce new samples using augmentation techniques. The augmented data is used only during the training process. Since fluent speech already takes up to 65% of the data we only augmented the clips with dysfluency labels.

Data augmentation is done using *audiomentations* library. For every dysfluent clips in the training set we add Gaussian noise with min. amplitude of 0.001 and max. amplitude of 0.015, time stretch up/down to 25%, and shift pitch up/down 4 semitones.

### 5.3. Data Splitting

The data is divided into three: train, validation and test sets. The train set contains clips of 10 most frequent

speakers, plus the dysfluency clips from FluencyBank, which gives us overall 2434 clips. What is left is divided between validation and test sets. Thus validation set consist of 734 clips of next most frequent speakers, and the test set contains 733 clips of less frequent speakers.

### 5.4. Training

We train three different models: baseline model, baseline model with stuttering classification head, baseline model with stuttering classification and show classification head. We call them BM, BSM and BSSM (See Figure 4), respectively. The latter two are MTL models. For all three models we use Adam optimizer with *learning\_rate* = 0.001, batch size is 32 and the number of epochs is 20. For the first MTL model the weights of losses are equal, thus  $\lambda_{baseline} = 0.5$  and  $\lambda_{stuttering} = 0.5$ . For the second MTL model we pay less importance to the show classification head as it is used more like regularization, hence the weights are distributed as  $\lambda_{baseline} = 0.4$ ,  $\lambda_{stuttering} = 0.4$ ,  $\lambda_{show} = 0.2$ .

### 5.5. Experimental Results

After training the models, we extract new features for the data and perform classification on Support Vector Machine (SVM) and K-Nearest Neighbor (KNN). The SVM with polynomial kernel of degree 7, and the *C* parameter of 100 is found to be most optimal one for the validation set. For KNN model the *k* is 1 in all our results. All performance evaluations in this section are conducted on test data, which was not used during the training of either the feature extraction network or the SVM and KNN models.

Table 1 presents the results of the classification done using different model combinations. Observe that, when we switch to MTL models (BSM and BSSM) there is

a significant improvement in the f1-scores of different stuttering types. Although switching to BSSM does not introduce improvements to SVM model's classification performance, it has major impact on KNN model. Recall that, our data has only 2% of *block* dysfluency types. So the models find hard to learn it, hence, we observe such small number of detected block types.

Table 1: F1-score for stuttering classification. (P: Prolongation, B: Block, SR: Sound Repetition, WR: Word Repetition, I: Interjection, F: Fluent, BM: Baseline Model, BSM: Baseline with stuttering classification head, BSSM: BSM with show classification head).

| Model    | F1-Score |      |      |      |      |      |
|----------|----------|------|------|------|------|------|
|          | P        | B    | SR   | WR   | I    | F    |
| BM_SVM   | 0.14     | 0.03 | 0.08 | 0.06 | 0.11 | 0.72 |
| BM_KNN   | 0.10     | 0.00 | 0.11 | 0.09 | 0.14 | 0.66 |
| BSM_SVM  | 0.31     | 0.04 | 0.13 | 0.11 | 0.33 | 0.74 |
| BSM_KNN  | 0.21     | 0.08 | 0.12 | 0.11 | 0.29 | 0.64 |
| BSSM_SVM | 0.26     | 0.00 | 0.15 | 0.08 | 0.30 | 0.74 |
| BSSM_KNN | 0.36     | 0.04 | 0.11 | 0.10 | 0.34 | 0.68 |

The classification results for the case when only dysfluency types are considered is reported in Table 2. Observe that the *block* type classification accuracy improves in this case. While the baseline model learns the embeddings that differentiate between different stuttering types, adding stuttering classification head enforces the model to learn the embeddings that also represent the stuttering types themselves. Once again, we can observe the improvement in classification that bring the MTL models. The embedding computed using BSM model brings almost 100% improvement to *prolongation*, *block* and *sound repetition* types' f1-score, and almost 400% improvement for *word repetition* type in SVM, in contrast to BM model. The BSSM embedding brings significant improvements to KNN's classification performance.

Table 2: Results of classification dysfluency types only. (P: Prolongation, B: Block, SR: Sound Repetition, WR: Word Repetition, I: Interjection, BM: Baseline Model, BSM: Baseline with stuttering classification head, BSSM: BSM with show classification head).

| Model    | F1-Score |      |      |      |      |
|----------|----------|------|------|------|------|
|          | P        | B    | SR   | WR   | I    |
| BM_SVM   | 0.19     | 0.09 | 0.15 | 0.08 | 0.40 |
| BM_KNN   | 0.13     | 0.10 | 0.21 | 0.18 | 0.40 |
| BSM_SVM  | 0.35     | 0.21 | 0.27 | 0.27 | 0.61 |
| BSM_KNN  | 0.26     | 0.11 | 0.22 | 0.19 | 0.60 |
| BSSM_SVM | 0.39     | 0.12 | 0.21 | 0.27 | 0.59 |
| BSSM_KNN | 0.43     | 0.16 | 0.22 | 0.31 | 0.58 |

We combine the five dysfluency types into one group and

name the group as non fluent type and perform the binary classification. The f1-scores are illustrated in Table 3. It turns out that MTL models improve fluent data classification, while non fluent type has small improvement. Thus, BSM embeddings bring 55% improvement to fluent data classification in SVM, while it is 9.7% for non fluent data.

Table 3: F1-score for binary classification.

| Model    | F1-Score |            |
|----------|----------|------------|
|          | Fluent   | Non Fluent |
| BM_SVM   | 0.49     | 0.41       |
| BM_KNN   | 0.66     | 0.41       |
| BSM_SVM  | 0.76     | 0.44       |
| BSM_KNN  | 0.64     | 0.44       |
| BSSM_SVM | 0.73     | 0.45       |
| BSSM_KNN | 0.68     | 0.45       |

Table 4: Accuracy results for binary, dysfluency type only and total classification.

| Model    | Accuracy |            |       |
|----------|----------|------------|-------|
|          | Binary   | Dysfluency | Total |
| BM_SVM   | 0.45     | 0.25       | 0.52  |
| BM_KNN   | 0.56     | 0.25       | 0.45  |
| BSM_SVM  | 0.66     | 0.43       | 0.57  |
| BSM_KNN  | 0.56     | 0.35       | 0.47  |
| BSSM_SVM | 0.64     | 0.42       | 0.57  |
| BSSM_KNN | 0.59     | 0.40       | 0.51  |

The accuracy of classification results are reported in Table 4. The accuracy of binary classification do not change much for KNN. However, SVM achieves 47% improvement with the MTL models. We observe significant accuracy improvement for the dysfluency type classification (when only 5 dysfluent categoris considered) both in KNN and SVM. We observe that the total accuracy does not change while the dysfluency type classification improves.

## 6. Conclusion

Stuttering detection is a complex problem. The complexity increases with the scarcity of the data. The existing datasets are highly imbalanced which leads to the learned models that favor the majority class. Since the data size is too small it is usually impossible to build complex networks because of the overfitting. By constructing networks that learn multiple tasks we can regularize the weights of the network. In this work, we built and learnt rather simple network on small and highly imbalanced dataset. Our findings show that by converting the network from a single task learner to a multi task learner,

and adding some auxiliary classification heads, we can significantly improve the identification of stuttering types.

### Acknowledgements

This work is funded by TEDU BAP Grant No. T-22-B2010-90108.

### References

- [1] Amruth, V., Lavanya, K., Manoj, N., Umme, H., and Deepika, M. B. (2020). A novel approach for stutter speech recognition and correction. *International Journal for Research in Applied Science and Engineering Technology (IJRASET)*, 8:544–547.
- [2] Arjun, K. N., Karthik, S., Kamalnath, D., Chanda, P., and Tripath, S. (2020). Automatic correction of stutter in dysfluent speech. *Procedia Computer Science*, 171:1363–1370.
- [3] Baeovski, A., Zhou, Y., Mohamed, A., and Auli, M. (2020). wav2vec 2.0: A framework for self-supervised learning of speech representations. In *Advances in Neural Information Processing Systems*, pages 12449–12460.
- [4] Bayerl, S., von Gudenberg, A. W., Hönig, F., Nöth, E., and Riedhammer, K. (2022a). KSoF: The kassel state of fluency dataset – a therapy centered dataset of stuttering. In *Proceedings of the Language Resources and Evaluation Conference LREC*, pages 1780–1787. European Language Resources Association.
- [5] Bayerl, S. P., Gerczuk, M., Batliner, A., Bergler, C., Amiriparian, S., Schuller, B., Nöth, E., and Riedhammer, K. (2023). Classification of stuttering – the compare challenge and beyond. *Computer Speech & Language*, 81.
- [6] Bayerl, S. P., Wagner, D., Nöth, E., Bocklet, T., and Riedhammer, K. (2022b). The influence of dataset partitioning on dysfluency detection systems. In Sojka, P., Horák, A., Kopeček, I., and Pala, K., editors, *Text, Speech, and Dialogue*, pages 423–436. Cham. Springer International Publishing.
- [7] Bayerl, S. P., Wagner, D., Nöth, E., and Riedhammer, K. (2022c). Detecting dysfluencies in stuttering therapy using wav2vec 2.0. In *Interspeech 2022*. ISCA.
- [8] Dash, A., Subramani, N., Manjunath, T., Yaragarala, V., and Tripathi, S. (2018). Speech recognition and correction of a stuttered speech. In *2018 International Conference on Advances in Computing, Communications and Informatics (ICACCI)*, pages 1757–1760.
- [9] Heeman, P., Lunsford, R., McMillin, A., and Yaruss, J. S. (2016). Using clinician annotations to improve automatic speech recognition of stuttered speech. In *Interspeech*, pages 2651–2655.
- [10] Howell, P., Davis, S., and Bartrip, J. (2009). The UCLASS archive of stuttered speech. *Journal of Speech, Language, and Hearing Research*, 52:556–596.
- [11] Howell, P. and Sackin, S. (1995). Automatic recognition of repetitions and prolongations in stuttered speech. In *Proceedings of the First World Congress on Fluency Disorders*, pages 372–374.
- [12] Kourkounakis, T., Hajavi, A., and Etemad, A. (2020). Detecting multiple speech dysfluencies using a deep residual network with bidirectional long-short-term memory. In *IEEE International Conference on Acoustics, Speech and Signal Processing, ICASSP 2020*, pages 6089–6093.
- [13] Kourkounakis, T., Hajavi, A., and Etemad, A. (2021). Fluentnet: End-to-end detection of stuttered speech dysfluencies with deep learning. *IEEE/ACM Transactions on Audio, Speech, and Language Processing*, 29:2986–2999.
- [14] Lea, C., Mitra, V., Joshi, A., Kajarekar, S., and Bigham, J. P. (2021). Sep-28k: A dataset for stuttering event detection from podcasts with people who stutter. In *IEEE International Conference on Acoustics, Speech and Signal Processing, ICASSP 2021*, pages 6798–6802.
- [15] Nöth, E., Niemann, H., Haderlein, T., Decher, M., Eysholdt, U., Rosanowski, F., and Wittenberg, T. (2000). Automatic stuttering recognition using hidden markov models. In *INTERSPEECH*.
- [16] Ratner, N. B. and MacWhinney, B. (2018). Fluency bank: A new resource for fluency research and practice. *Journal of Fluency Disorders*, 56:69–80.
- [17] Shakeel, A. S., Md, S., Fabrice, H., and Slim, O. (2021). Stutternet: Stuttering detection using time delay neural network. In *2021 29th European Signal Processing Conference (EUSIPCO)*, pages 426–430.
- [18] Shakeel, A. S., Md, S., Fabrice, H., and Slim, O. (2022a). Machine learning for stuttering identification: Review, challenges and future directions. *Neurocomputing*, 514:385–402.
- [19] Shakeel, A. S., Md, S., Fabrice, H., and Slim, O. (2022b). Robust stuttering detection via multi-task and adversarial learning. In *European Signal Processing Conference (EUSIPCO)*.

# Hydrochar Production from Cigarette Butts and Tobacco for Dye Adsorption

Sevda Esmâ Darama<sup>1,\*</sup>, Semra Çoruh<sup>2</sup>, Selim Ceylan<sup>3</sup>, Elif Hatice Gürkan<sup>4</sup>

<sup>1</sup> Ondokuz Mayıs University, Environmental Engineering Department, Samsun, Turkey, sevda.akkaya@omu.edu.tr, ORCID: 0000-0002-6747-4679

<sup>2</sup> Ondokuz Mayıs University, Environmental Engineering Department, Samsun, Turkey, semcoruh@omu.edu.tr, ORCID: 0000-0002-8306-1890

<sup>3</sup> Ondokuz Mayıs University, Chemical Engineering Department, Samsun, Turkey, selim.ceylan@omu.edu.tr, ORCID: 0000-0001-7258-6205

<sup>4</sup> Ondokuz Mayıs University, Chemical Engineering Department, Samsun, Turkey, elif.gurkan@omu.edu.tr, ORCID: 0000-0003-3868-181X

## ABSTRACT

In this study, tobacco waste generated from cigarette and cigar production, as well as discarded cigarette butts resulting from cigarette use, were recycled and their use as adsorbent materials was investigated. For this purpose, both products underwent various thermal and chemical treatments and were converted into hydrochar form. Chemically activated hydrochar was used in dye removal experiments due to its high surface area and adsorbent properties. Malachite green was selected as the dye material for the project. Adsorption experiments were conducted at different initial concentrations, adsorbent doses, and contact times. In experiments on the removal of malachite green with butts and tobacco waste hydrochars, removal rates as high as 99% were obtained. As a result of adsorption experiments carried out with both hydrochars, it was observed that the adsorption fits the Langmuir isotherm model and the Pseudo-Second-Order kinetic model. Tobacco waste and discarded cigarette butts, which are cheap, readily available, and abundant, were found to be effective alternative adsorbents for malachite green removal.

## ARTICLE INFO

### Research article

Received: 28.09.2024

Accepted: 18.12.2024

### Keywords:

adsorption,  
chemical activation,  
discarded cigarette  
butts,  
hydrochar  
tobacco waste  
malachite green

\*Corresponding author

## 1. Introduction

Water pollution occurs from anthropogenic and industrial (batteries, metallurgy, mining, nuclear, tannery, textiles, etc.) effluents and domestic sewage, mining, and recreational activities [1]. Therefore, protecting water sources and quality is highly significant because of poses a severe risk to human or environmental health. The concurrent removal of these coexisting highly hazardous pollutants is difficult due to their toxicity and persistent environmental nature [2, 3]. Adsorption, chemical precipitation, coagulation, electro dialysis, exchange, ion exchange, phytoextraction, precipitation, reverse osmosis, solvent extraction, and ultrafiltration are used to remove wastewater contaminated by dye ions. Adsorption is the most effective, low-cost, eco-friendly, and highly selective method [4].

In recent years, hydrochar has been produced from waste biomass, mainly by thermochemical conversion methods,

and used as a biosorbent for organic and inorganic pollutants removal in wastewater [5].

Biomass can be used as an energy source by burning directly, or it can be converted into electrical energy, solid material (hydrochar), liquid fuel, or valuable chemicals by applying various thermo-chemical processes [6]. One of the best methods to convert biomass into different fuels is pyrolysis.

Pyrolysis is the thermal decomposition of materials at high temperatures in a limited or completely oxygen-free environment. It is usually used in the processing of organic substances [7]. Pyrolysis is a process that occurs at lower temperatures compared to gasification. Gasification is carried out at 800-1100°C, while pyrolysis is carried out at 400-700°C [8]. The inert gas used during pyrolysis is important for the removal of products from the environment. As a result of the pyrolysis process, three different forms of products are obtained; solid (biochar), liquid (biooil) and gas (syngas). Pyrolysis temperature and speed change the yield of the product obtained in different forms. Slow

pyrolysis is generally preferred for obtaining solid products, it is carried out at low temperatures and long reaction times. In obtaining solid products, 35% product efficiency is obtained with slow pyrolysis, 12% with fast pyrolysis and 5% with flash pyrolysis [9, 10]. In this study, the activation process was carried out with slow pyrolysis.

The activation process is used to increase the usability of hydrochars or biochars produced by various methods as adsorbents [11]. With chemical activation, the physico-chemical properties of the raw material are improved with acid, base and oxidation processes and their transformation into active carbon is ensured. Chemical activation processes are generally carried out by pyrolysis using HCl, HNO<sub>3</sub>, H<sub>2</sub>SO<sub>4</sub> and H<sub>3</sub>PO<sub>4</sub>, KOH, NaOH, K<sub>2</sub>CO<sub>3</sub>, H<sub>2</sub>O<sub>2</sub> and KMnO<sub>4</sub> chemicals [5, 12]. With chemical activation, generally cross-linked surface functional groups and activated carbons with high specific surface area and pores are obtained. It is known that the surface porosity and functional groups of activated carbons produced with alkaline chemical activation agents such as KOH, NaOH and K<sub>2</sub>CO<sub>3</sub> increase [13]. In this study, activation was carried out with KOH agent.

Cigarettes represent one of the most popular tobacco products being consumed worldwide. Tobacco and tobacco smoke contains more than 7,000 chemicals, over 70 of which are carcinogenic. Some carry health risks such as heart and/or lung disease. Globally, more than five trillion discarded cigarette butters year have been produced by smokers [14]. They include ash, unburned tobacco, and smoked filter. 95% of cigarette filters are made of cellulose acetate. Smoked filters contain no tobacco. It is packed tightly together to create a filter and is a plastic slow to degrade. The cigarette butt reduces risks associated with smoking by decreasing smoke toxicants. Cigarette butts may threaten humans and wildlife, including toxic chemicals [9].

Cigarette butts are non-biodegradable waste. But we know very little knowledge about their impacts on both human health and the environment. Discarded cigarette butts contain arsenic, benzene, cadmium, ethylene oxide, formaldehyde, nicotine, and dozens of other chemicals caused by tobacco and its residues [9]. 4.5 trillion cigarette butts are not disposed of correctly every year globally, generating 1.69 billion pounds of toxic waste and releasing thousands of chemicals into the air, water, and soil [15]. In recent years, various studies have come to the fore to reduce the toxic effect of cigarette butts and re-evaluate these wastes [16].

For this study, tobacco waste and discarded cigarette butt hydrochars were synthesized. The effects of dosage, initial concentration, and contact time in removing malachite green (MG) from aqueous solution were also assessed while evaluating the solution adsorption isotherms and kinetics. Relevant adsorption results obtained from the prepared hydrochars after chemical activation indicate the utility of the low-cost recycled material.

## 2. Materials and Methods

### 2.1 Materials

Tobacco wastes were obtained from British American Tobacco, Samsun, Turkey. The waste cigarette butts were collected from a range of residential areas by our means. The filters separated from waste discarded cigarette butts by peeling off the paper on the outside. A stock aqueous solution was prepared with powdered malachite green dye. It was diluted with pure water at calculated rates to be used in experiments.

### 2.2. Methods

#### *Hydrochar production*

There is no standard method for hydrochar production. It is basically the carbonization process of organic matter using temperature and water pressure in a closed reactor. In this study, average experimental conditions of similar studies in the literature were used for hydrochar production, activation process and adsorption conditions [8, 13]. 10 g tobacco and filter sample with 80mL pure water (Nuve ND4 Pure Water System) (1:8 ratio) were placed in a completely closed hydroreactor with a volume of 250mL, consisting of a separate steel outer and titanium-coated inner chamber. The reactor was kept in a muffle furnace at 250 °C for 5 hours. The reactor was cooled in a bucket full of cold water, and the obtained slurry was butted. Hydrochars were dried in a drying oven (Nuve EN400 Model) at 50 – 60°C for 24 hours.

#### *Hydrochar activation*

If the solid part is to be used as a result of the pyrolysis process, slow pyrolysis conditions are applied because the solid product yield in slow pyrolysis conditions is much higher than in fast pyrolysis [13, 17]. The produced hydrochars were activated by slow pyrolysis system using Potassium hydroxide (KOH) at a ratio of 1:4 (10g hydrochars:40g KOH). Pyrolysis was carried out at 5 °C/min in a 100 mL/min nitrogen gas flow at 600°C with a holding time of 1 hour. After pyrolysis, the samples were washed with 2M hydrochloric acid (HCl) in a vacuum filtration (Rocker 400 Vacuum Pump System) and then washed with distilled water until neutral. Pyrolysis conditions were determined by taking the average values of our previous experimental study results and similar studies in the literature [17, 18].

#### *Characterization Analysis*

Some characterization analyses were carried out to determine the suitability of natural and hydrochar butts and tobacco for use as an adsorbent. For this purpose, elemental analysis (LECO-Truespec Model) was performed to determine the elements it contained, Scanning Electron Microscope (SEM) (Jeol-JSM7001F Model) to determine microstructure and morphology, and Brunauer-Emmett-

Teller (BET) (Oantachrome-Autosorb IQ2 Model) analysis to measuring the specific surface area.

#### Batch adsorption experiments

In order to determine the optimum adsorption conditions in the removal of MG dye with waste cigarette butts hydrochar and tobacco hydrochar adsorbents, adsorption experiments are first carried out under different conditions (at various minimum and maximum values). Batch adsorption experiments; were carried out to understand the effects of dosage (0.33 - 16.66 g/L), initial concentration (30 - 800 mg/L), and adsorption time (1-120 min). All adsorption experiments were conducted at room temperature. The samples separated from the adsorbent after adsorption were measured to determine their final concentrations in a spectrophotometer (Thermo Aquamate Model) at a wavelength of 617nm. The spectrophotometer was calibrated at a wavelength of 617 nm using standard MG aqueous solutions with concentrations of 2, 4, 8, 16, 32, and 64 mg/L. The calibration curve equation obtained was ( $y = 0.1082x + 0.0408$ ), with a  $R^2$  value of 0,99. The absorbance values recorded during the sample measurements were substituted for “y” in the equation, and the corresponding “x” values were calculated to determine the MG concentrations of the samples in mg/L.

All experiments were conducted in duplicate, and the average values of the results were used.

#### Isotherm and kinetic models

In order to understand the adsorption mechanism, adsorption experimental results are generally examined in terms of their fitting with adsorption kinetic and isotherm models. In this study, the results were applied to Langmuir, Freundlich and Dubinin-Radushkevich (D-R) isotherm models and Pseudo-first-order, Pseudo-second-order and Intraparticle kinetic models.

### 3. Results and Discussion

#### 3.1 Characterization Analysis

##### Elemental analysis

The elemental analysis results of tobacco and butt hydrochar produced in the study are given in Table 1. Elemental analysis indicates that both samples have high carbon content. The elemental analysis results of hydrochars have values close to similar studies in the literature. 44.20-62.73% carbon, 1.49-6.96% hydrogen, 6.85-4.13% nitrogen [16, 19]. Similar results were found in different studies on the raw and hydrochar of tobacco leaf residues [18, 19]. The variation in results for the same materials may result from different conditions of the pyrolysis processes. The elemental analysis indicated the lower nitrogen compounds because the bio-oil part produced during pyrolysis has the most nitrogen compounds. Moreover, there are also losses due to volatile compounds. In the literature, studies conducted with tobacco and tobacco products indicate that the main gases released are water, CH<sub>4</sub>, hydrocarbons, CO<sub>2</sub>, CO, carbonyl and hydroxyl [14, 20].

**Table 1.** Elemental analysis of tobacco and butt hydrochar

| Sample                          | Carbon (%) | Hydrogen (%) | Nitrogen (%) |
|---------------------------------|------------|--------------|--------------|
| Waste cigarette butts hydrochar | 49.45      | 2.71         | 0.65         |
| Tobacco hydrochar               | 33.63      | 2.54         | 1.82         |

##### Scanning electron microscope (SEM)

SEM images at x500 were used to analyze the surface morphologies of tobacco and cigarette butt hydrochar. (Fig. 1a and b). The SEM image of the butt hydrochar shows a rigid amorphous and porous structure with smaller microstructures (Fig. 1a). It was observed that the pore level

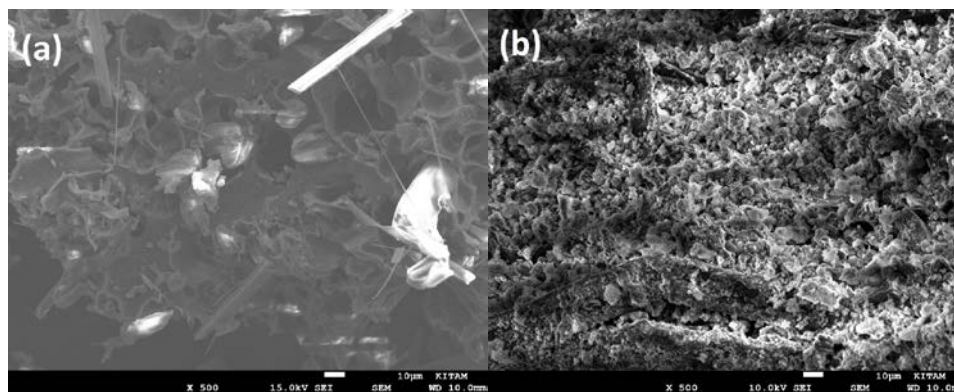


**Figure 1.** SEM image of butt hydrochar (a) and tobacco hydrochar (b).

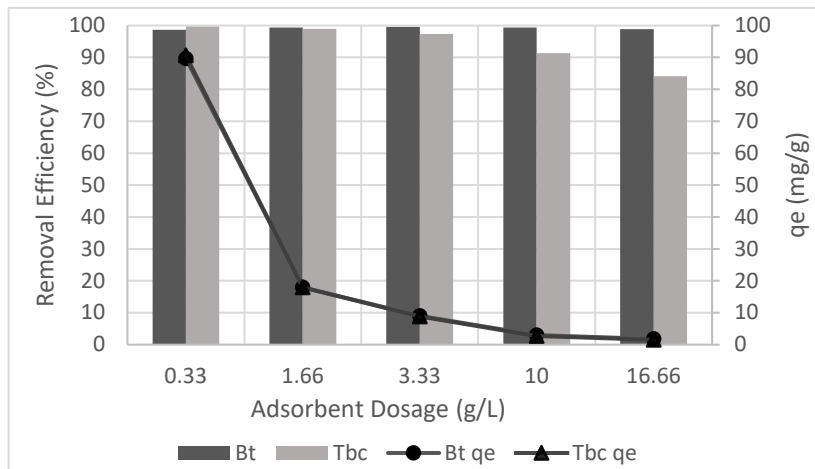
was high in the sem images of tobacco hydrochar (Fig. 1b). The larger pores and voids are observed in the butt hydrochar compared to the tobacco hydrochar. This may be due to the collection of particles found in the smoke passing through the butt [21]. The microsphere structure of both samples given in Figure 1 shows condensation, decarboxylation, decomposition, dehydration or polymerization, and aromatization of cellulosic components during hydrothermal carbonization, as indicated in the study by Sevilla et al. [21]

gas flow at 150°C and vacuum application for 14 hours. As a result, the BET surface area for butt and tobacco hydrochar is 8.4m<sup>2</sup>/g and 1.8m<sup>2</sup>/g respectively. Although these results seem low for natural adsorbents, they are similar to studies conducted with the same materials in the literature [20, 22].

**3.2 Batch adsorption experiments**

*Effect of adsorbent dosage*

The effect of adsorbent dose on adsorption efficiency was



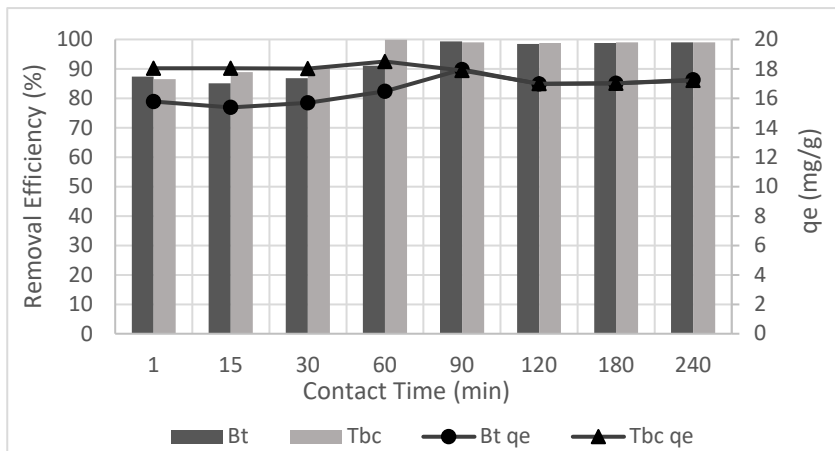
\*Bt: Butt, Tbc: Tobacco

**Figure 2.** Effects of adsorbent dosage for butt and tobacco hydrochars.

*Brunauer-Emmett-Teller (BET)*

The surface area analysis by BET was also performed. BET surface area measurements were performed under nitrogen

studied using a different amount of adsorbent (0.33, 1.66, 3.33, 9.99, 16.66 g/L). Other batch adsorption experiment conditions are 30 mL volume, 30 mg/L initial concentration, 200 rpm, 90 min. contact time. In Figure 2, malachite green



\*Bt: Butt, Tbc: Tobacco

**Figure 3.** Effects of contact time for butt and tobacco hydrochars.

removal efficiencies and adsorption capacity ( $q_e$ ) values versus adsorbent dose are given.

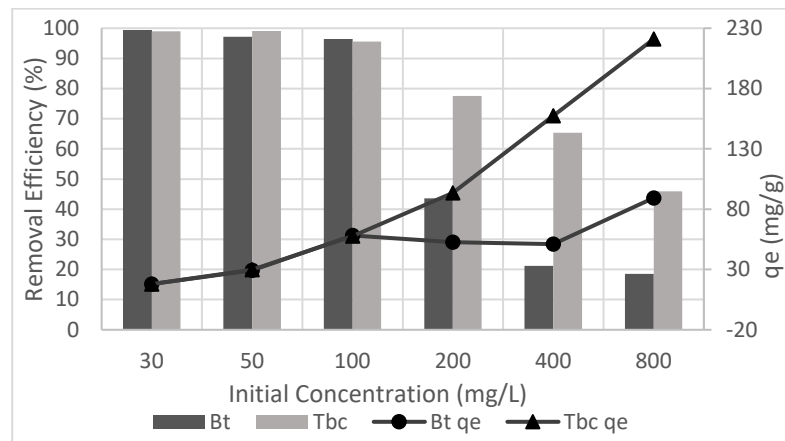
In the Figure 2, it is seen that removal efficiency above 85% was obtained in all doses and materials. No significant change in removal efficiency was observed in the cigarette butt samples depending on the dose. In the tobacco samples, removal efficiency decreased by around 10-14% with the increase in dose. The highest removal efficiency was obtained at around 99% at 1.66g/L dose for both adsorbents.

#### Effect of contact time

In order to show the effect of contact time on MG removal, adsorption experiments were carried out at different contact times. For this purpose, experiments were carried out at contact times of 1, 15, 30, 60, 90, 120, 180 and 240 min. In Figure 3, malachite green removal efficiencies and adsorption capacity ( $q_e$ ) values versus contact time are given. In both adsorbent samples, MG removal efficiency increased with increasing contact time. It is seen that cigarette butt samples reached equilibrium after 90 minutes

mass transfer from the liquid phase (adsorbate) to the solid phase (adsorbent) at the interface [23]. At high concentrations, the tobacco adsorbent is seen to have much higher removal efficiency and adsorption capacity than the cigarette butt adsorbent. At low concentrations, removal efficiency values above 95% were obtained for both adsorbents.

The  $K$  ( $\text{mol}^2/\text{kJ}^2$ ) value calculated in the D-R isotherm is a constant that represents the energy density or free energy change associated with the adsorption process and reflects the heterogeneity of the adsorbent surface. This parameter aids in distinguishing whether the adsorption mechanism is physical or chemical. Using the  $K$  value, the average free energy ( $E$ ) of the adsorption process can be determined. The  $E$  ( $\text{kJ/mol}$ ) value quantifies the energy required to transfer a molecule to the adsorption site. Specifically:  $E < 8 \text{ kJ/mol}$ : Adsorption is typically physical, dominated by weak forces such as van der Waals interactions.  $E = 8\text{--}16 \text{ kJ/mol}$ : Adsorption may involve chemical properties, such as ion exchange.  $E > 16 \text{ kJ/mol}$ : Adsorption is likely driven by



\*Bt: Butt, Tbc: Tobacco

**Figure 4.** Effects of initial concentration for butt and tobacco hydrochars.

and tobacco samples reached equilibrium after 60 minutes. The appropriate contact time for each adsorbent was selected as 90 minutes. After 90 minutes, efficiencies were obtained around 99%.

#### Effect of initial concentration

To determine the effect of MG initial concentration on adsorption, experiments were carried out at different initial MG concentrations. Initial concentration studies were carried out at 30, 50, 100, 200, 400 and 800 mg/L MG concentrations. In Figure 4, MG removal efficiencies and adsorption capacity ( $q_e$ ) values versus initial concentration are given.

In Figure 4, a gradual decrease in removal efficiency is observed with increasing concentration for both adsorbents. This can be explained by an existing higher driving force for

chemical bonding, such as covalent interactions [24]. The  $E$  values obtained from the study were determined to be 2.96 kJ/mol for butt hydrochars and 1.81 kJ/mol for tobacco hydrochars. These results indicate that the adsorption mechanisms for both materials can be classified as physical.

### 3.3 Adsorption isotherms

**Table 2.** Isotherm parameters for MG adsorption onto the butt and tobacco hydrochar

| Isotherms  | Parameters                                   | Malachite Green |                   |
|------------|--|-----------------|-------------------|
|            |  | Butt Hydrochar  | Tobacco Hydrochar |
| Langmuir   | $R^2$  | 0.90            | 0.97              |
|            | $K_L$ (L/mg)                                 | 0.02            | 0.04              |
|            | $Q_m$ (mg/g)                                 | 83.33           | 227.27            |
| Freundlich | $R^2$  | 0.73            | 0.97              |
|            | $K_F$ ( $\text{mg}^{1-n} \text{L ng}^{-1}$ ) | 29.11           | 32.10             |
|            | $n$  | 6.80            | 3.16              |
| D-R        | $R^2$  | 0,66            | 0,78              |
|            | $K$ ( $\text{mol}^2/\text{kJ}^2$ )           | 0,0571          | 0,1524            |
|            | $\text{Ln}q_m$                               | 3,99            | 4,76              |

The isotherm of adsorption explains the relationship between the adsorbate particles adsorbed on the adsorbent surface and the equilibrium adsorbate concentration in the liquid phase [25]. Adsorption mechanisms can be examined for physical and chemical adsorption. The weak Van der Waals force between the adsorbate molecules and the adsorbent surface is effective in physical adsorption [4, 25]. Strong covalent bonds or ionic interactions are effective in chemical adsorption. So, adsorbate molecules are accumulated on the adsorbent surface by chemical bonds in chemisorption [4]. A multi-molecular layer is formed in physical adsorption, and a mono-molecular layer is formed in chemical adsorption. The Langmuir isotherm indicates that adsorption is commonly monolayer due to adsorbate molecules adhering to particular homogeneous sites on the adsorbent surface [25]. There are unfilled sites on the adsorbent, and is no interaction between the molecules retained on the surface. The multilayer adsorption on the homogeneous sites of the adsorbent surface was clarified with the Freundlich adsorption isotherm. It is reversible (desorption with temperature increase or pressure reduction) [4, 12]. The Dubinin-Radushkevich (D-R) isotherm is a

model used to describe adsorption processes, particularly in cases where the adsorption follows a pore-filling mechanism rather than surface adsorption. It is suitable for predicting the adsorption of gases and liquids onto porous materials and considers the energy of adsorption to estimate the heterogeneity of the surface. Unlike the Langmuir isotherm, the D-R model can handle non-uniform systems and is based on the Polanyi potential theory [24].

Table 2 shows the isotherm parameters and their correlation coefficients ( $R^2$ ) for MG adsorption onto butt and tobacco hydrochar. Figure 5 shows the isotherm models graphs. The Langmuir isotherm model best fits the experimental data for MG onto butt and tobacco hydrochar according to the correlation coefficients ( $R^2$ ). Maximum adsorption capacity ( $Q_m$ ) 83.33mg/g and 227.27mg/g was derived for the adsorption of MG onto butt and tobacco hydrochars respectively.

**Table 3.** Kinetic parameters of MG adsorption onto the butt and tobacco hydrochar

| Kinetics            | Parameters  | MG             |                   |
|---------------------|---|----------------|-------------------|
|                     |   | Butt Hydrochar | Tobacco Hydrochar |
| Pseudo First Order  | $R^2$   | 0.90           | 0.70              |
|                     | $k_1$ ( $\text{min}^{-1}$ )                       | 0.008          | 0.05              |
|                     | $q_e$ ( $\text{mg g}^{-1}$ )                      | 2.57           | 893.90            |
| Pseudo Second Order | $R^2$   | 0.99           | 0.99              |
|                     | $k_2$ ( $\text{g mg}^{-1} \text{min}^{-1}$ )      | 0.034          | 0.05              |
|                     | $q_e$ ( $\text{mg g}^{-1}$ )                      | 17.45          | 17.18             |
| Intraparticle       | $R^2$   | 0.61           | 0.45              |
|                     | $k_i$ ( $\text{m g}^{-1} \cdot \text{min}^{-2}$ ) | 0.20           | 0.08              |
|                     | $C$   | 15.05          | 18.34             |

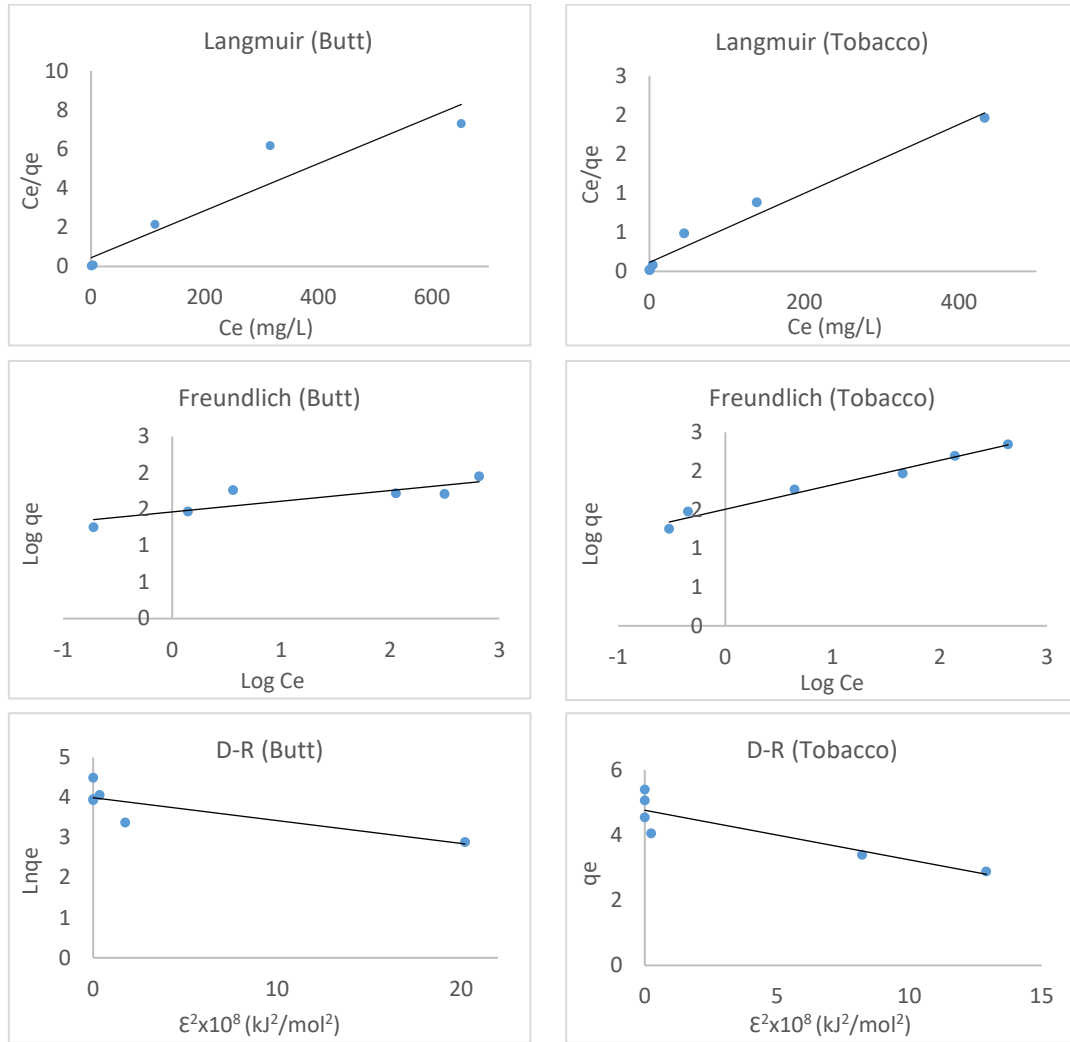


Figure 5. Adsorption isotherm graphs.

The Langmuir model describes monolayer sorption in that the adsorbate molecule is adsorbed on particular localized adsorption sites [25]. It indicates no transmigration of the adsorbate in the plane of the surfaces and gives uniform energies of monolayer sorption on the adsorbent surface [12].

The Freundlich isotherm model best fits the experimental data for MG onto tobacco hydrochar.  $K_F$  (mg/g) represents the adsorption capacity at equilibrium and  $n$  describes the adsorbent surface's heterogeneity and the adsorbed molecules' distribution on the adsorbent surface. The  $n$  was 3.16 (Table 2), showing the intensity of MG adsorption to tobacco hydrochar.  $n > 1$  indicates suitable adsorption of the adsorbate molecules onto the adsorbent surface [25].

### 3.4 Adsorption kinetics

The kinetics of adsorption gives information about the reaction rate concerning the time at constant pressure or concentration [12]. The first step of the sorption mechanism is diffusion adsorption from the adsorbate to the adsorbent surface. The adsorbate molecules coming to the liquid-solid interface pass through the stagnant part on the surface and move towards the pores of the adsorbent in the second stage. This stage is realized by film mass transfer or boundary layer diffusion theory. The third stage is known as pore diffusion. At this stage, the species to be adsorbed is transported in pores of different sizes subject. In the fourth stage, the adsorbate molecules are attached to the pores of the appropriate size and take place [25, 26].

Figure 6 shows the kinetic models graphs. The pseudo-first-order, pseudo-second-order, and intraparticle diffusion models studied the MG adsorption kinetics on butt and tobacco hydrochar. The pseudo-second-order kinetic model

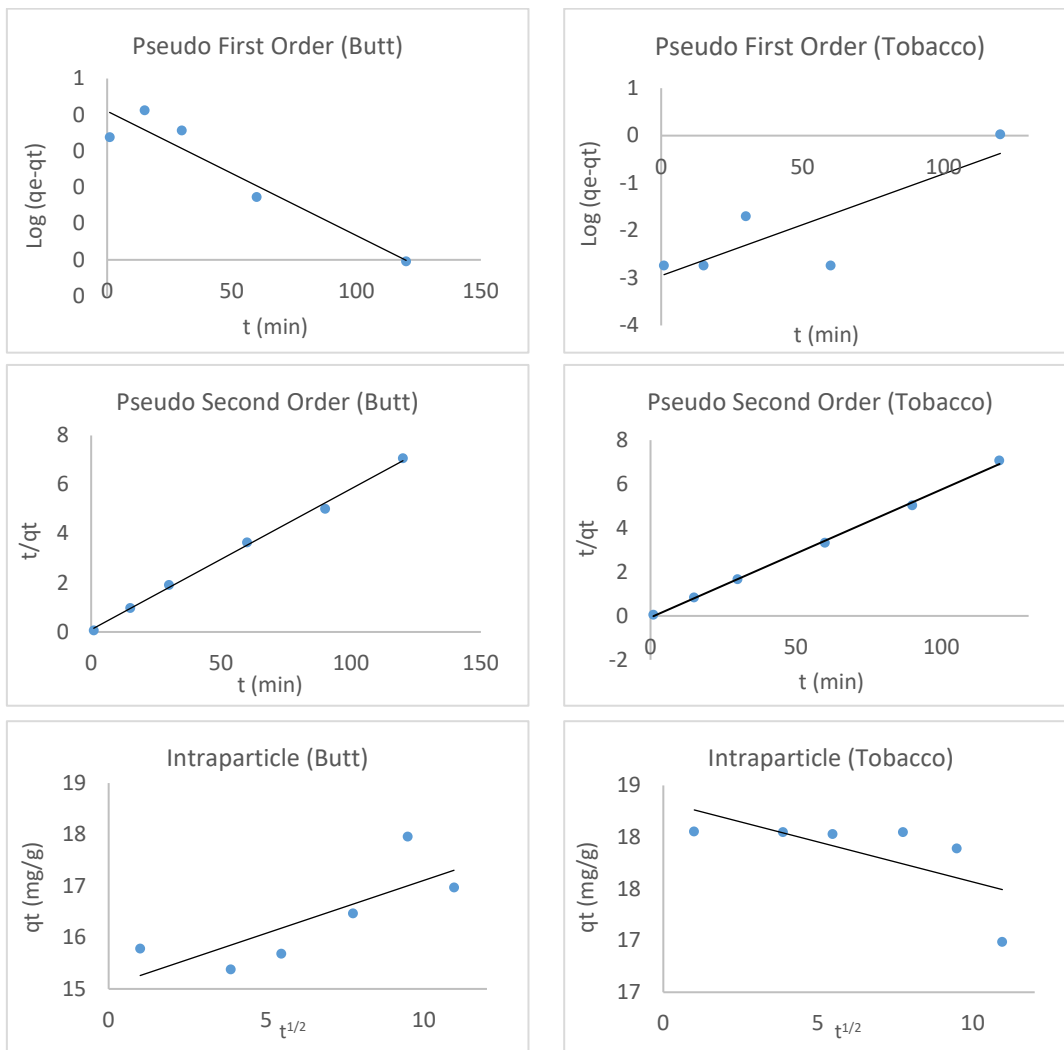


Figure 6. Adsorption kinetic graphs.

best fits the experimental data ( $R^2 = 0.99$ ) for the adsorption of MG onto butt and tobacco hydrochar (Table 3).

The pseudo-second-order kinetic model's fitting showed the chemisorption mechanism's involvement in the rate-determining step [26].

#### 4. Conclusion

In this study, chemically activated hydrochars were produced from cigarette butts and tobacco wastes using potassium hydroxide (KOH) through a two-step pyrolysis method. Elemental composition, morphological structure, and surface area analyses of the produced hydrochars indicated that they are suitable for use as adsorbents. The hydrochars were then applied to the removal of Malachite Green, a chemical dye widely used in various industrial applications that poses toxic risks to both the environment and human health, from aqueous solutions. The adsorption method was employed in the removal studies, yielding

exceptionally high removal efficiencies of up to 99%. However, a rapid decline in removal efficiency was observed at higher Malachite Green concentrations (200 mg/L and above). Isotherm and kinetic modeling studies were conducted to elucidate the adsorption mechanism. The results revealed that the adsorption process was single-layered, homogeneous, and chemical in nature. The findings suggest that tobacco and cigarette butt wastes can serve as effective and low-cost alternatives for dye removal. Future studies could further support these results through desorption and regeneration experiments.

#### References

- [1]. Adegoke, K.A. and O.S. Bello, "Dye sequestration using agricultural wastes as adsorbents", *Water Resources and Industry*, 12, (2015), 8-24.

- [2]. Mahmoodi, N.M., O. Masrouri, and F. Najafi, "Dye removal using polymeric adsorbent from wastewater containing mixture of two dyes", *Fibers and Polymers*, 15, (2014), 1656-1668.
- [3]. Sen, N.E. and Z.M. Senol, "Effective removal of Allura red food dye from water using cross-linked chitosan-diatomite composite beads", *Int J Biol Macromol*, 253, (2023), 126632.
- [4]. You, X., et al., "Adsorption of dyes methyl violet and malachite green from aqueous solution on multi-step modified rice husk powder in single and binary systems: Characterization, adsorption behavior and physical interpretations", *J Hazard Mater*, 430, (2022), 128445.
- [5]. Basakildan Kabakci, S. and S.S. Baran, "Hydrothermal carbonization of various lignocellulosics: Fuel characteristics of hydrochars and surface characteristics of activated hydrochars", *Waste Manag*, 110, (2019), 259-268.
- [6]. Yahav Spitzer, R., et al., "Biocrude extraction from human-excreta-derived hydrochar for sustainable energy and agricultural applications", *Environ Res*, 247, (2024), 118287.
- [7]. Amarasinghe, H.A.H.I., S.K. Gunathilake, and A.K. Karunaratna, "Ascertaining of Optimum Pyrolysis Conditions in Producing Refuse Tea Biochar as a Soil Amendment", *Procedia Food Science*, 6, (2016), 97-102.
- [8]. Krishna Veni, D., et al., "Biochar from green waste for phosphate removal with subsequent disposal", *Waste Manag*, 68, (2017), 752-759.
- [9]. Zi, W., et al., "Pyrolysis, morphology and microwave absorption properties of tobacco stem materials", *Sci Total Environ*, 683, (2019), 341-350.
- [10]. Wang, Y., R. Yin, and R. Liu, "Characterization of biochar from fast pyrolysis and its effect on chemical properties of the tea garden soil", *Journal of Analytical and Applied Pyrolysis*, 110, (2014), 375-381.
- [11]. Zhang, P., et al., "Characteristics of tetracycline adsorption by cow manure biochar prepared at different pyrolysis temperatures", *Bioresour Technol*, 285, (2019), 121348.
- [12]. Jalilian, M., et al., "A review: Hydrochar as potential adsorbents for wastewater treatment and CO<sub>2</sub> adsorption", *Sci Total Environ*, 914, (2024), 169823.
- [13]. Goel, C., et al., "CO<sub>2</sub> adsorption by KOH-activated hydrochar derived from banana peel waste", *Chemical Papers*, 78, (2024), 3845-3856.
- [14]. Zhou, N., et al., "Effect of pyrolysis condition on the adsorption mechanism of heavy metals on tobacco stem biochar in competitive mode", *Environ Sci Pollut Res Int*, 26, (2019), 26947-26962.
- [15]. Kibet, J.K., A. Jebet, and T. Kinyanjui, "Molecular oxygenates from the thermal degradation of tobacco and material characterization of tobacco char", *Scientific African*, (2019), 5.
- [16]. Wei, M., et al., "Extraction of Nitrogen Compounds from Tobacco Waste via Thermal Treatment", *Energies*, 13, (2020), 18.
- [17]. Onorevoli, B., et al., "Characterization of feedstock and biochar from energetic tobacco seed waste pyrolysis and potential application of biochar as an adsorbent", *Journal of Environmental Chemical Engineering*, 6, (2018), 1279-1287.
- [18]. Blankenship, L.S. and R. Mokaya, "Cigarette butt-derived carbons have ultra-high surface area and unprecedented hydrogen storage capacity", *Energy & Environmental Science*, 10, (2017), 2552-2562.
- [19]. Lima, H.H.C., et al., "Hydrochars based on cigarette butts as a recycled material for the adsorption of pollutants", *Journal of Environmental Chemical Engineering*, 6, (2018), 7054-7061.
- [20]. Calabuig, E., N. Juárez-Serrano, and A. Marcilla, "TG-FTIR study of evolved gas in the decomposition of different types of tobacco", *Effect of the addition of SBA-15*. *Thermochimica Acta*, 671, (2019), 209-219.
- [21]. Sevilla, M., J.A. Maciá-Agulló, and A.B. Fuertes, "Hydrothermal carbonization of biomass as a route for the sequestration of CO<sub>2</sub>: Chemical and structural properties of the carbonized products", *Biomass and Bioenergy*, 35, (2011), 3152-3159.
- [22]. Tomczyk, A., et al., "Purification of Aqueous Media by Biochars: Feedstock Type Effect on Silver Nanoparticles Removal", *Molecules*, 25, (2020), 12.
- [23]. Pathy, A., et al., "Malachite green removal using algal biochar and its composites with kombucha SCOBY: An integrated biosorption and phycoremediation approach", *Surfaces and Interfaces*, (2022), 30.
- [24]. Donat, R., et al., "Thermodynamic parameters and sorption of U(VI) on ACSF", *Journal of Radioanalytical and Nuclear Chemistry*, 279, (2008), 271-280.
- [25]. Zhang, X., et al., "Adsorption-reduction removal of Cr(VI) by tobacco petiole pyrolytic biochar: Batch experiment, kinetic and mechanism studies", *Bioresour Technol*, 268, (2018), 149-157.
- [26]. Haladu, S.A., "Highly efficient adsorption of malachite green dye onto a cross-linked pH-responsive cyclotriphosphazene resin: Kinetic, equilibrium and thermodynamic studies", *Journal of Molecular Liquids*, (2022), 357.

# A Study on Controllable Mod Exploiting the Intrinsic Symmetry Breaking of Low-symmetry Photonic Crystals

Özgür Önder Karakılınc<sup>1,\*</sup>

<sup>1</sup> Pamukkale University, Electrical and Electronics Engineering Department Denizli, Türkiye, okarakilinc@pau.edu.tr, ORCID: 0000-0003-4586-9845

## ABSTRACT

Photonic crystals are periodic dielectric structures that create photonic band gaps depending on the geometry of the lattice elements and the material properties. These structures allow light to be easily controlled, guided, and confined due to the tunability and adjustability of their design parameters. Conventional photonic crystals are typically designed with high-symmetry unit cells, while low-symmetry structures are created by breaking this symmetry. Low-symmetry structures are more sensitive to light manipulation and offer greater control and flexibility over light through geometric diversity. This study investigates the resonance effect in a cavity structure composed of a square lattice photonic crystal made of low-symmetry C2-type dielectric rods. The dependence of the resonance mode on the low-symmetry parameters was investigated and it was shown that, in contrast to other studies, mode splitting or merging can be achieved and tuned by exploiting and perturbing the intrinsic symmetry properties of the low-symmetry photonic crystal structure. The band structure, transmission spectra, and resonance frequencies of the low rotational symmetry photonic crystal were obtained using Lumerical and MEEP software. The analysis of resonance splitting and optical properties by symmetry manipulation will contribute to the understanding of light collimation and trapping.

## ARTICLE INFO

### Research article

Received: 16.11.2024

Accepted: 12.12.2024

### Keywords:

Photonic crystals, Low symmetry, Resonance mode

\*Corresponding author

## 1. Introduction

Photonic crystals (PCs) are artificial materials that exhibit photonic band gaps depending on the geometry of the structure and the refractive index properties, and contain a one-dimensional (1D), two-dimensional (2D) or three-dimensional (3D) periodic arrangement of a dielectric medium. The bandgap response and wave propagation characteristics of the photonic crystal lattice strongly depend on the rods' arrangement, geometry, and material [1], [2]. Furthermore, by introducing defects into photonic crystals, light can be controlled and manipulated, and integrated optical devices can be formed. In photonic crystal structures, cavities can be designed by creating line or point defects. Light is temporarily and spatially confined at the resonant frequency within these cavity structures, known as optical resonators. The optical resonator is a fundamental functional block required for filtering, modulation, buffering, and switching in integrated optical circuit systems [3]. The key components of photonic crystal circuits, such as channel-drop filters and coupled-cavity waveguides, take advantage of defect mode coupling. The effect on the defect mode shift is much more sensitive to a small change in the refractive index than the band edge shift. Applications of photonic crystals can be

divided into two types based on the reflective or transmissive nature of the photonic crystal. Light can be easily controlled in photonic crystals as a function of wavelength, enabling the creation of low-loss, wide or narrow bandwidths, and sharp bends equivalents compared to their counterparts [4]. Furthermore, by introducing defects into photonic crystals, light can be controlled and manipulated, and integrated optical devices can be formed [2]. By tuning the configuration of the defect or cavity structure, various functions for advanced signal processing can be realized in all-optical photonic circuits [3]-[5]. Light is temporarily and spatially confined at the resonant frequency within these cavity structures, known as optical resonators. The optical resonator is a fundamental functional block required for filtering, modulation, buffering, and switching in integrated optical circuit systems [3]. The quality factor or Q-factor is an important parameter that determines the performance of a resonant cavity. The photonic microcavity is characterized by the cavity resonant wavelength and the quality factor (Q-factor). The Q-factor is defined as the ratio of the cavity mode wavelength to the cavity mode spectral linewidth [1], [6]. The Q-factor and mode volume are measures of the temporary perturbation time and spatial occupation in the cavity, respectively. In wavelength division multiplexing applications, the Q-factor

and transmission characteristics are important for narrowband filtering [1]. In addition, the strong confinement of light also enhances nonlinear interactions [7]. A designer can change the bandwidth or shape of the frequency response by adjusting the coupling coefficients between the resonances present in the system. As the designer controls the strength of the perturbation, the separation between the two resonant mode frequencies varies accordingly. The key components of photonic crystal circuits, such as channel-drop filters and coupled-cavity waveguides, take advantage of defect mode coupling. The ability to control mode splitting by adjusting the perturbation strength is an important feature of photonic crystal structures. By manipulating the coupling between resonant modes, the designer can engineer the desired spectral response, which is critical for applications such as filtering, switching, and multiplexing in integrated photonic circuits. Defect mode coupling is the underlying principle of many fundamental photonic crystal devices, highlighting the importance of understanding and precisely controlling mode splitting in these periodic dielectric structures. Mode degeneracy in photonic crystal structures is a consequence of the inherent symmetry of the lattice. By deliberately introducing a perturbation, either by a physical change in the cavity or by the addition of an extra element, the mode degeneracy can be removed, leading to mode splitting. This ability to control and tune mode splitting is a valuable feature of photonic crystals, as it enables the engineering of desired spectral responses for applications such as filtering, switching, and multiplexing in integrated photonic circuits. The literature [8]-[11] has explored various approaches to achieving mode splitting, highlighting the flexibility and potential of this technique.

High rotational symmetry photonic crystals exhibit perfectly symmetric ordering. While it simplifies the design and analysis of these structures, it also limits the flexibility to manipulate the optical properties. By reducing the symmetry of the unit cell, low-symmetry photonic crystals (LSPCs) offer greater opportunities for geometric customization and, consequently, greater control over the light-matter interactions. This flexibility is achieved by introducing additional elements or reconfiguring the existing components within the unit cell [12]. The geometric and structural diversities introduced by symmetry reduction in photonic crystal waveguides and cavities enhance the dispersion properties of these periodic materials [13]-[15]. Additionally, low-rotational symmetric photonic crystal structures efficiently manipulate the equifrequency contours, leading to the emergence of self-collimation transmission [16], [17]. The ability to break high symmetry and explore low symmetry designs is featured in the design of photonic crystals to tailor their optical properties for applications such as sensors [18], [19], superprisms [20], and splitters [21]. In this study, the dependence of the degenerate resonance mode on the low-symmetry parameters was investigated, and unlike other studies [10], [11], [22], [23], the intrinsic low-symmetry

property of the low-symmetry photonic crystal structure was used to control the resonance modes. To obtain a low-symmetry photonic crystal structure, two rods with different radii were added next to the central rod in a square lattice photonic crystal formed in air, thus breaking the high symmetry of the unit cell (Figure 1). A shoulder-coupled cavity was then created within a linear defect waveguide (LDWG). The splitting and fusing of the cavity modes was studied by varying the position and radius of the low symmetry rods. Mode analysis of the cavity was performed for different radii and positions of the low-symmetry rods, and transmission and reflection spectra were obtained. The results showed that the splitting or merging of the degenerate cavity modes can be controlled by varying the position and/or radius of the low-symmetry rods without the need for additional perturbation. The PWE and FDTD methods implemented in MPB, MEEP and Lumerical software were used to obtain the dispersion behavior and transmission/reflection spectra of the photonic crystal structure. The final experimental study, which is a well-accepted method due to the scalable nature of photonic crystals, was attempted using a microwave experimental setup. However, the measurement results could not be reliably obtained due to the differences between the simulation environment and the experimental setup.

## 2. Coupled Mode Theory of the Cavity

In photonic crystal structures, two types of optical resonators can be designed: (1) resonators based on line or point defects. For example, a resonator is created by modifying the dimensions or dielectric constant of the rods, resulting in a defect that behaves like a resonator, and (2) ring resonators, where some rods are removed and/or modified to form a ring-shaped resonator. Optical resonators are typically used in conjunction with waveguides and the interaction between them is governed by Coupled Mode Theory (CMT). Optical resonators are divided into two groups related to standing wave (SW) and traveling wave (TW) resonators. Optical communication devices such as filters, add/drops, and multiplexers are realized with the SW or TW type of resonators placed between two optical waveguides. The light signal can be coupled into or dropped from the waveguides via the resonator structure [3]. Optical resonators are typically used in conjunction with waveguides and the interaction between them is governed by Coupled Mode Theory (CMT). In this section, the coupling equations for a standing wave-type direct or indirect shoulder-coupled structure in the waveguide-cavity-waveguide junction are given, and the transmission/reflection plots obtained using MATLAB are presented.

*Directly Coupled Cavity:* To characterize a directly coupled cavity of the standing wave type, as shown in Figure 1a, it is necessary to define some parameters, namely the resonant frequency or wavelength  $\omega_0$  ( $\lambda_0$ ); the amplitudes of the incident, transmitted, reflected and dropped waveguide modes

$s_i, s_t, s_r, s_d$ ; the perturbation rates  $1/\tau_w$  and  $1/\tau_i$  due to the coupling loss and the intrinsic loss of the waveguide; the corresponding quality factors  $Q_w$  and  $Q_c$ ; the total quality factor  $Q_t$ ; the normalized frequency  $\delta$ ; and the transfer functions  $t, r, d$  for the transmission, reflection and drop ports, respectively, as given in Eqs. (1-5) [3].

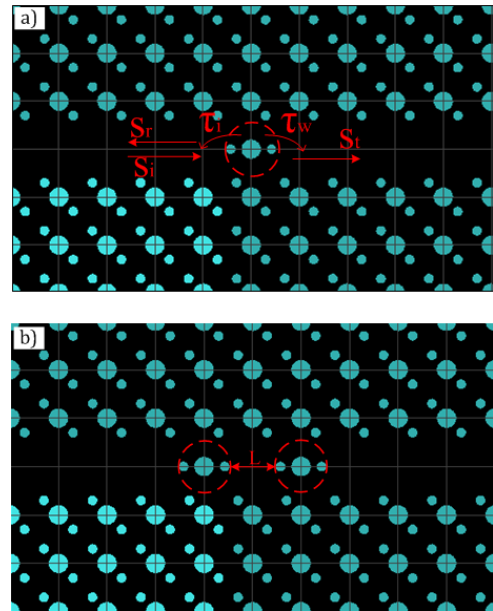


**Figure 1.** Low symmetry photonic crystal waveguide with (a) direct or (b) indirect shoulder-coupled standing wave resonator structure.

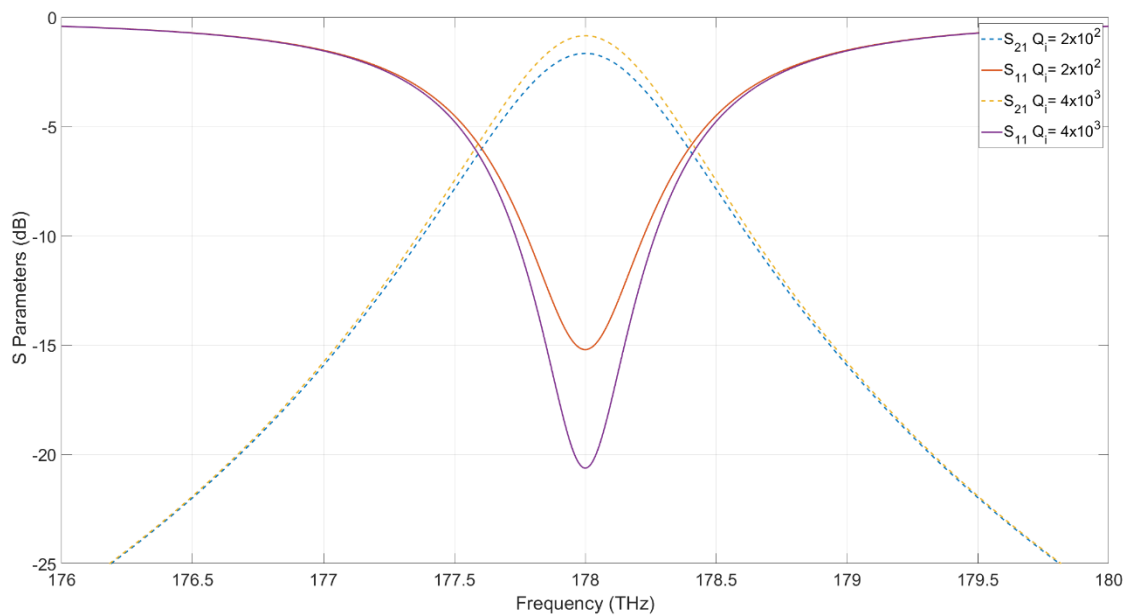


**Figure 2.** Transmission and reflection parameters for  $Q_w=2 \times 10^2$  at  $Q_i=2 \times 10^2$  and  $Q_i=4 \times 10^3$  with CMT for standing wave type direct shoulder coupled waveguide-cavity structure

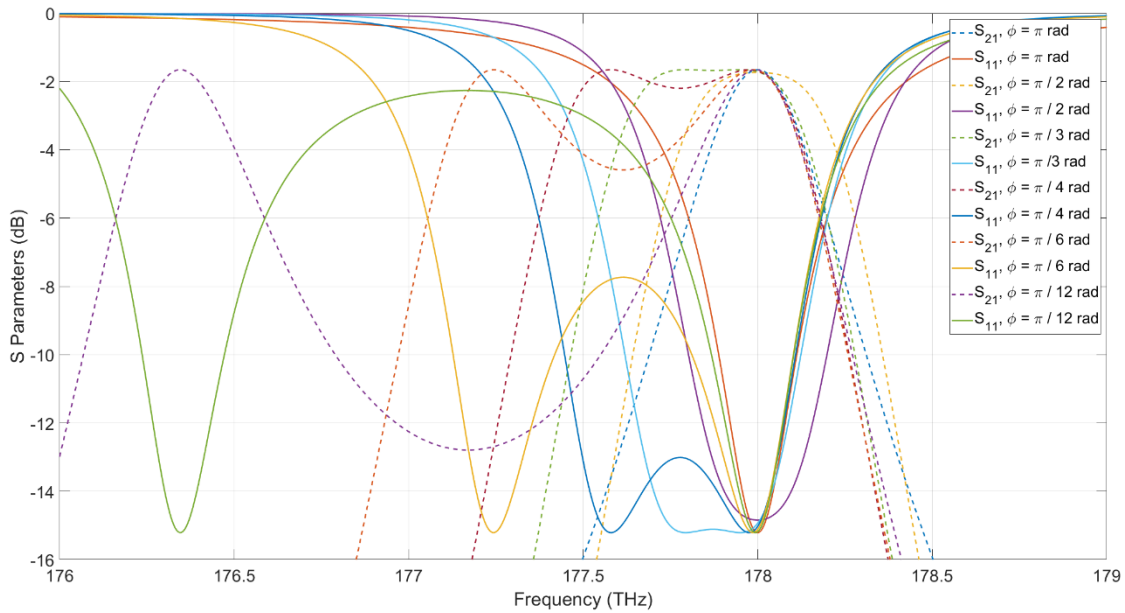


**Figure 3.** Transmission/reflection parameters for standing wave type indirectly shoulder coupled waveguide cavity structure with CMT for  $Q_i=4 \times 10^3$ ,  $Q_w=2 \times 10^2$  at  $\phi = \pi, \pi/2, \pi/3, \pi/4, \pi/6, \pi/12$  rad phase difference

$$\delta = \frac{\omega - \omega_0}{\omega_0} \tag{1}$$

$$\frac{1}{Q_t} = \frac{1}{Q_i} + \frac{1}{Q_w} \tag{2}$$

$$t = \frac{st}{si}, r = \frac{sr}{si}, d = \frac{sd}{si} \tag{3}$$

$$Q_i = \frac{\omega_0 * \tau_i}{2} \tag{4}$$

$$Q_w = \frac{\omega_0 * \tau_w}{2} \tag{5}$$

For the waveguide-cavity-waveguide configuration, we can use  $Q_w$  to represent the total waveguide coupling, so that  $Q_w = \omega_0 \tau_w$ . The term  $1/\tau_w$  is the decay rate due to the coupling loss of the waveguide. According to coupled mode theory, the transfer function at the transmit port is given by equation (6) [3]:

$$t = \frac{1/Q_w}{j2\delta + 1/Q_i + 1/Q_w} \tag{6}$$

The transmission T can be calculated as  $T = |t|^2$ , where  $\theta$  represents the phase shift and is calculated as  $\theta = \arg(t)$ , and  $\tau$  represents the group delay, calculated as  $\tau = d\theta(\omega)/d\omega$ . For a waveguide-cavity-waveguide structure supporting a standing wave (SW) cavity, the transmission level approaches unity when the condition  $Q_i \gg Q_w$  is satisfied, as shown in Figure 2. However, as the Q value increases, the intermodal isolation

within the passband decreases, and the mode frequencies approach each other.

*The indirectly coupled cavity:* This structure, formed by the sequential coupling of two standing wave waveguide-cavity-waveguide systems as shown in Figure 1b, contains two cavity modes due to the presence of two different cavities. This results in a phase shift of  $\phi$  between the cavities. Examining equation (7), the parameter  $\gamma$  represents the transfer function of the reflecting port for a singly coupled standing wave cavity. However, since the system consists of two indirectly coupled cavities, there are two different values of  $\gamma$ .

$$\gamma = \frac{-1}{2Q_w(j\delta + \frac{1}{2Q_i} + \frac{1}{2Q_w})} \tag{7}$$

Since there are two cavities in a cascaded port structure, two different  $\gamma$  values,  $\gamma_1$  and  $\gamma_2$ , can be considered. In the transfer function, amplitude transfers for the mirrors are  $-\gamma_1$  and  $-\gamma_2$ , while the amplitude reflections are  $-\gamma_1 - 1$  and  $-\gamma_2 - 1$ , respectively. The reflection and transmission functions of the whole system can then be obtained from equations (8-9).

$$t = \frac{\gamma_1 \gamma_2 e^{j\theta}}{1 - (1 + \gamma_1)(1 + \gamma_2) e^{j2\theta}} \tag{8}$$

$$r = \frac{-(1 + \gamma_1) + (1 + 2\gamma_1)(1 + \gamma_2) e^{j\theta}}{1 - (1 + \gamma_1)(1 + \gamma_2) e^{j2\theta}} \tag{9}$$

To simplify the system, if we assume  $\gamma_1 = \gamma_2$ , the transfer function of the transmitted port can be rewritten as Equation (10) [3].

$$t = \frac{1}{8Q_w^2 \sin \phi} \frac{1}{\left(j\left(\delta + \frac{\cot \frac{\phi}{2}}{4Q_w}\right) + \frac{1}{2Q_i} + \frac{1}{4Q_w}\right)\left(j\left(\delta - \frac{\tan \frac{\phi}{2}}{4Q_w}\right) + \frac{1}{2Q_i} + \frac{1}{4Q_w}\right)} \quad (10)$$

The intrinsic quality factor  $Q_i$  and the waveguide coupling quality factor are given as  $2Q_w$ . Since the resonant frequency splitting is highly dependent on  $\phi$ , it can only be changed by adjusting  $\phi$ . Figure 3 shows that as the phase difference between successive cavities decreases, the mode splits and the bandwidth increases. Conversely, as the phase difference increases, the modes merge again. Analyzing the mode splitting, it is observed that there is critical coupling at a phase difference of  $\pi/3$  and overcoupling at  $\pi/12$ .

### 3. Proposed Low-Symmetry Photonic Crystal Cavity Structure and Methodology

This study builds on the low-symmetry structure used in reference [24]. The low-symmetry configuration is created by adding two additional rods at a  $45^\circ$  orientation to a photonic crystal structure consisting of circular cross-section rods arranged in a square lattice on an air substrate. The dielectric constant of both the primary lattice rods and the low-symmetry rods is 12, with radii of  $r=0.2a$  and  $r_s=0.1a$ , respectively. The low symmetry rods are positioned at a distance of  $0.42a$  from the lattice rods. Here “ $a$ ” denotes the lattice constant, with all dimensions and operating frequencies of the photonic crystal normalized accordingly. For example, if  $a=1 \mu\text{m}$ , then a normalized frequency of 0.4 corresponds to 120 THz.

In the low-symmetry photonic crystal, a waveguide is formed by removing a row of lattice elements arranged in both a linear and a 90-degree bend configuration. In this design, a low-symmetry cavity is placed within the waveguide or at the corner bend region. This cavity structure acts as a coupling element between the waveguides within the low-symmetry photonic crystal structure. The waveguide-cavity coupling utilizes a shoulder coupling configuration operating in the standing wave type. Cases where the dielectric constant of the rods is 12 and 9.61 have been investigated. As a preliminary work, the band diagrams for each low-symmetry photonic crystal lattice were generated. By considering low-symmetry cavity structures, transmission and reflection spectra were obtained by applying various perturbations, such as adding rods, varying rod radii, and changing rod positions within the structure, allowing an analysis of mode splitting. However, this paper only presents results for the linear waveguide configuration with a dielectric constant of 12.

There is no definitive analytical solution for photonic crystal structures containing disorder. The theoretical study of photonic properties in disordered structures is limited to time-consuming numerical simulations. Due to the challenges of analytical approaches, numerical methods are used for the analysis and design of photonic structures. Several methods exist for analyzing the dispersion behavior and transmission spectra of photonic crystals, including the transfer matrix method (TMM) [25], the finite-difference time-domain (FDTD) method [26], the plane wave expansion (PWE) method [27], and the finite element method (FEM) [28], among others. These methods can be divided into frequency domain and time domain calculations. Frequency domain methods are primarily used to calculate band structures, whereas time domain methods are more suitable for evaluating wave propagation and transmission, resonance modes, decay times, etc. Each method has its own strengths and limitations, with PWE and FDTD standing out in terms of performance and meeting the requirements for effective analysis of photonic crystal-based optical devices.

The approach to solving the band structure of a photonic crystal, known as the Plane Wave Expansion (PWE) method, is based on the Fourier expansion of the electromagnetic field and the dielectric function [1], [27]. The PWE method is primarily used for the theoretical analysis of photonic crystal structures, initially using the concept that the eigenmodes in periodic structures can be represented as a superposition of plane waves. The PWE method excels in the calculation of band structure diagrams and modal field patterns. When the original periodicity of the crystal is disturbed, or when a point or line defect appears within the structure, the supercell approach must be applied [1]. Although this method provides an accurate solution for the dispersion properties (propagation modes and photonic band gap) of a photonic crystal, it has certain limitations. Transmission spectra, field distributions and back reflections cannot be derived as only propagation modes are considered. An alternative approach, widely used for the calculation of both transmission spectra and field distributions, is based on the numerical solution of Maxwell's equations via the finite-difference time-domain (FDTD) method. Transmission and reflection spectra are calculated using a numerical FDTD method with Perfectly Matched Layers (PML) or absorbing boundary conditions [26]. Typically, the PWE method is used to calculate the photonic band gap and propagation modes of the photonic crystal structure, while FDTD is used to calculate the transmission spectrum [29]. In this study, the angular position of the low-symmetry rods in the cavity was varied in  $15^\circ$  steps from  $0^\circ$  to  $180^\circ$ , and the rod radius was adjusted between  $0.05a$  and  $0.1a$  to investigate the transmission characteristics and mode splitting. The transmission characteristics (S-parameters) were obtained and visualized using Lumerical FDTD software. In the final stage, experimental studies were carried out using a microwave setup, exploiting the scalability of

photonic crystals. The physical dimensions of the structure were adapted to the microwave range by exploiting the scalability characteristic of photonic crystals. For example, by choosing a lattice constant of  $a=15.8$  mm, a normalized frequency of 0.4 corresponds to a frequency of 7.5 GHz. Variations in the purity of the dielectric constant of the available rods and inconsistencies in the rod diameters also affected the experimental results. In the experimental setup designed according to the proposed configurations, the  $S_{21}$  parameter could be measured with a network analyzer, while accurate  $S_{11}$  measurements were difficult. The reasons for this include differences in source placement and type between the experimental and simulation setups. In the simulation, the source is placed directly inside the structure, whereas this is not possible in the microwave measurement setup. In addition, in the simulation the structure is isolated from the external environment and surrounded by a Perfectly Matched Layer (PML), whereas such isolation is not possible in the experimental setup.

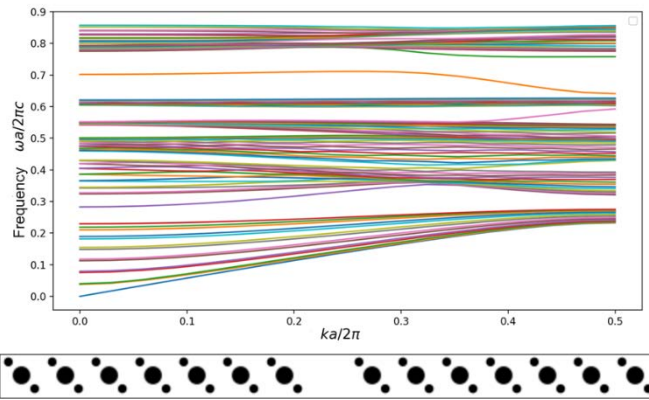


**Figure 4.** Supercell structure and TM band diagram of the PC structure with low symmetry linear defect ( $\epsilon_r=12$ ,  $\Theta$ :  $45^\circ$ )

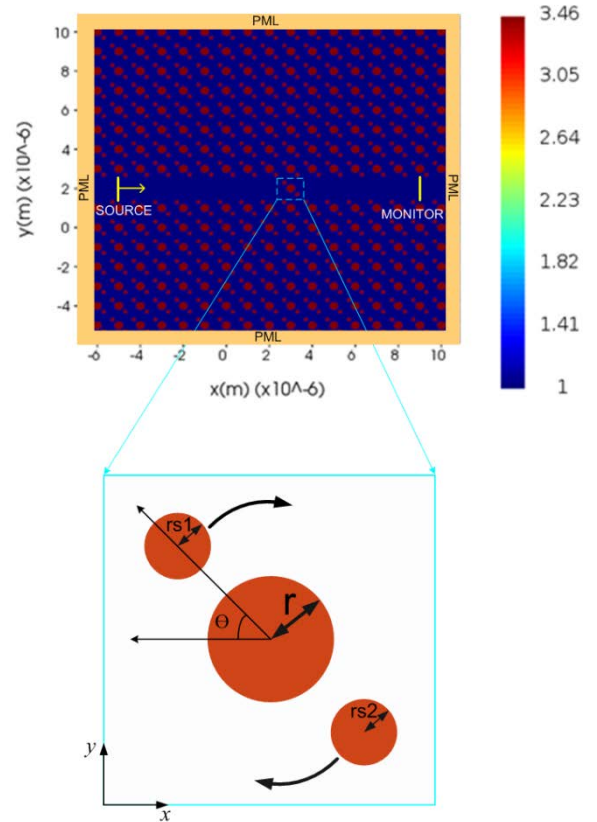


**Figure 5.** Simulation schematic and refractive index representation of the cavity structure used with the waveguide in the Low Symmetry PC

#### 4. Simulation Results and Analysis

In the simulation phase, both direct and indirect coupling configurations were investigated. In the indirect coupling structure, two identical cavities were positioned at a distance of  $2a$ . For the waveguide-cavity coupling configuration, the position and radius of the low-symmetry rods adjacent to the central rod were varied for both cavity types, allowing the transmission coefficient ( $S_{21}$ ) and reflection coefficient ( $S_{11}$ ) to be calculated. The angle between the low symmetry rods and the horizontal axis was varied from  $0^\circ$  to  $180^\circ$  in  $15^\circ$  increments. The rod radius was varied from 0 to  $0.1a$  in steps of  $0.05a$ . According to the simulation results, mode splitting and merging can be achieved by simply changing the angular position of the low-symmetry rods, without the need for additional perturbation in the cavity. As the angle of the low-symmetry rod relative to the  $x$ -axis increases, the resonant mode frequency splits, resulting in an expanded bandwidth. In addition, the center frequency of the band shifts to lower frequencies.

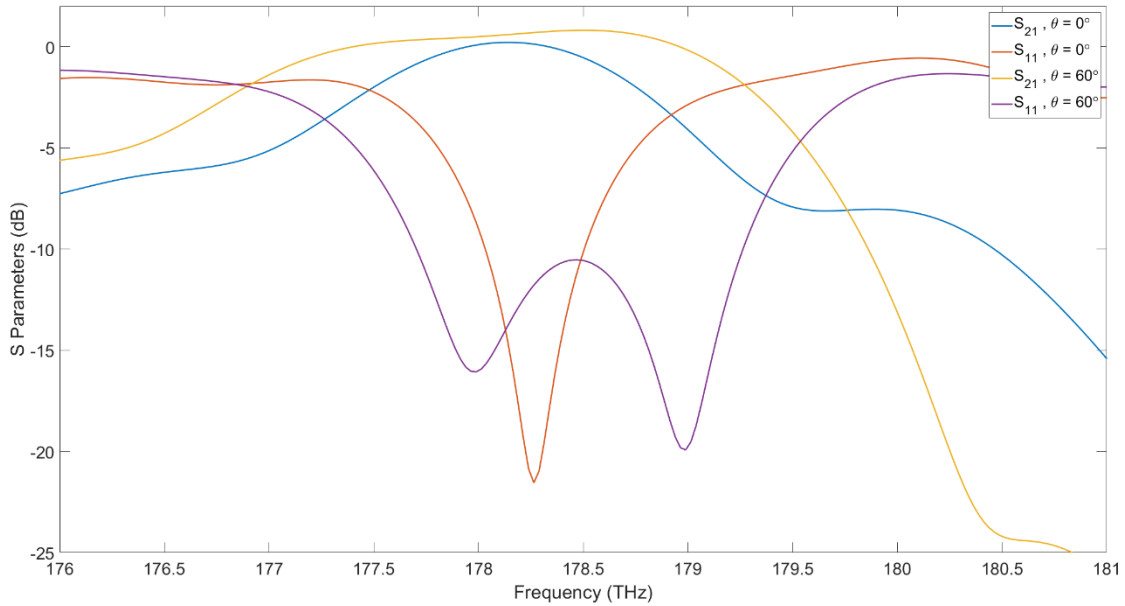


**Figure 6.** Transmission/reflection parameters obtained by simulation at different low symmetry rod angle values in direct coupled cavity ( $rs=0.1a$ )

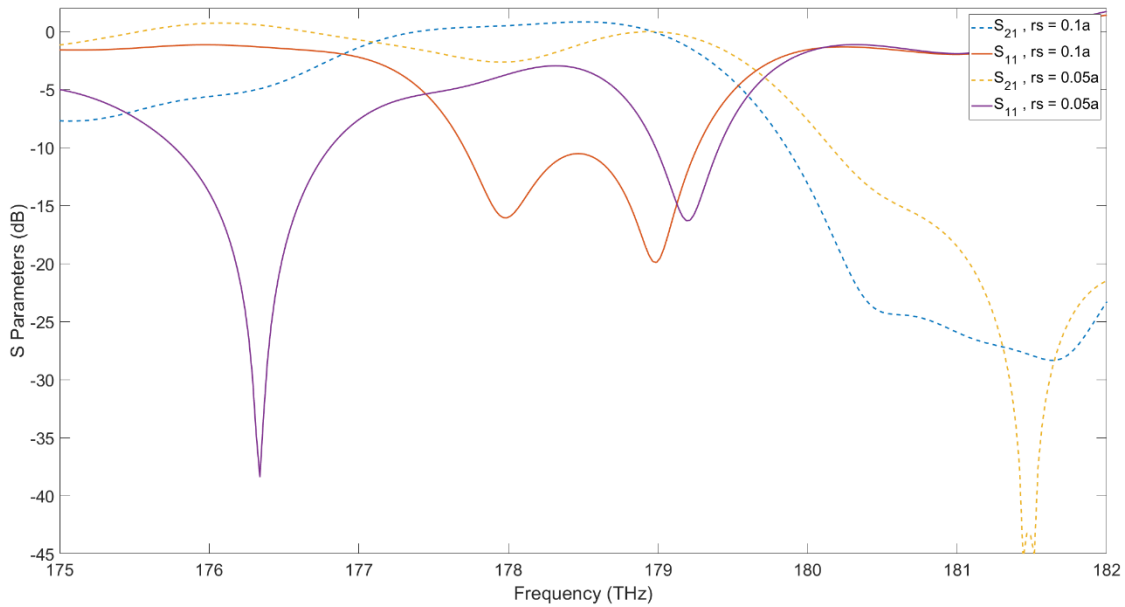


**Figure 7.** Transmission/reflection parameters obtained by simulation at different low symmetry rod radius values in direct coupled cavity ( $\theta=0^\circ$ )

#### 4.1 Directly Coupled Cavity

In the simulation results for the directly coupled cavity shown in Figure 6 (corresponding to the structure in Figure 1a), it is observed that the 3dB bandwidth of the band for a single mode is 1.4 THz. As the angle increases, the mode splits and the bandwidth reaches 2.5 THz. At the same angle, mode splitting

is observed for both low-symmetry rod radii, with an increase in bandwidth at lower radius values, as shown in Figure 7. Mode analysis of the low-symmetry cavity using the MPB simulation gave the calculated values  $Q_i=4 \times 10^3$  and  $Q_w=2 \times 10^2$ . When these values are used with the CMT equations, the results are in good agreement with the simulation, as shown in Figure 8.

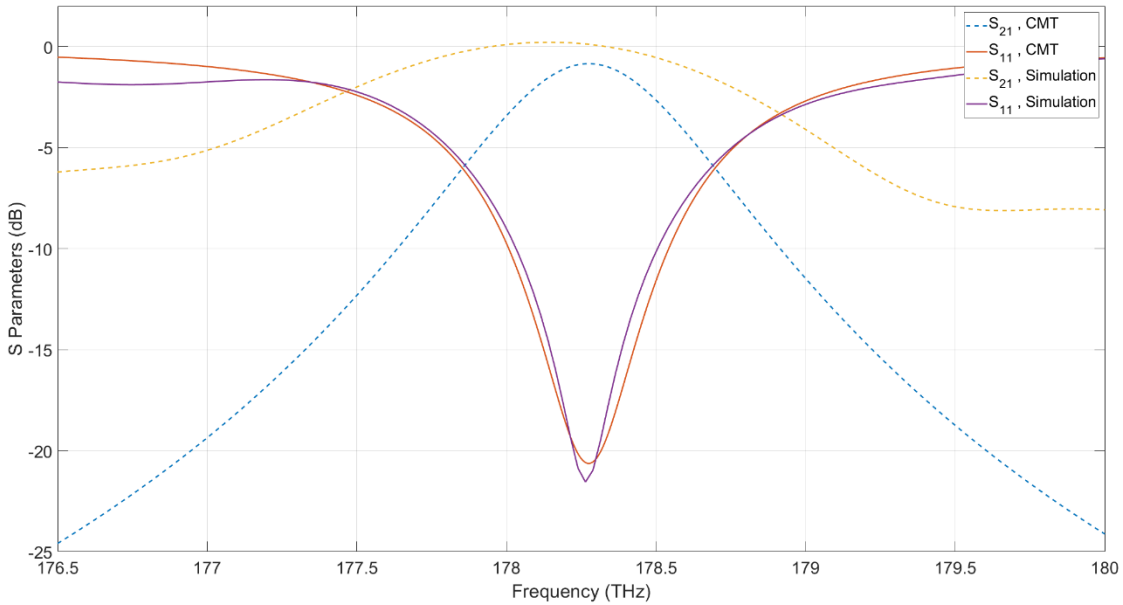


**Figure 8.** Comparison of CMT calculation and simulation result ( $Q_i=4 \times 10^3$ ,  $Q_w=2 \times 10^2$ ,  $\theta=0^\circ$  ve  $rs=0.1a$ )

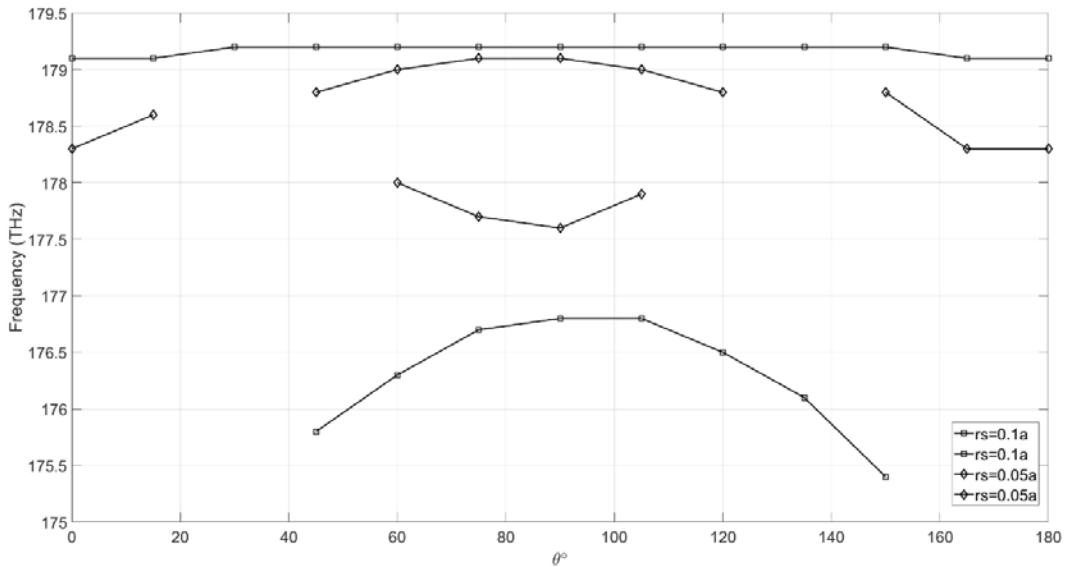


**Figure 9.** Variation of mode frequencies at different angle values for  $rs=0.05a$  and  $rs=0.1a$  in direct coupled structure

#### 4.2 Indirectly Coupled Cavity

As a further part of the study, the indirectly coupled cavity structure shown in Figure 1b was created using the methodology described in the previous section. Two cavities with equivalent properties were placed  $2a$  apart. The angle between the low-symmetry rods and the horizontal axis and

the rod radii were varied in both cavities and the transmission/reflection parameters were plotted. In the zero degree configuration, a single mode appeared in the directly coupled structure, while mode splitting occurred in the indirectly coupled structure. However, as the phase difference between the adjacent cavities increased, the modes merged again, as shown in Figure 3. The bandwidth, on the other hand, increased as the phase difference decreased. When the phase difference between the two cavities was  $\pi/36$ , the comparison

between the CMT calculation and the simulation showed good agreement, as shown in Figure 11. When comparing the CMT and simulation results, shift in mode frequencies is observed in Figure 11 compared to Figure 8. In the indirectly coupled cavity model shown in Figure 1b, the distance between the cavities, enclosed by the red dotted line, is denoted as  $L$ .

However, upon examining each cavity, which consists of primary lattice rods and low-symmetry rods, it becomes evident that each cavity contains a separate defect within itself. This change in distance, and consequently the phase difference, can be considered the cause of the observed shift in the transmission spectrum.

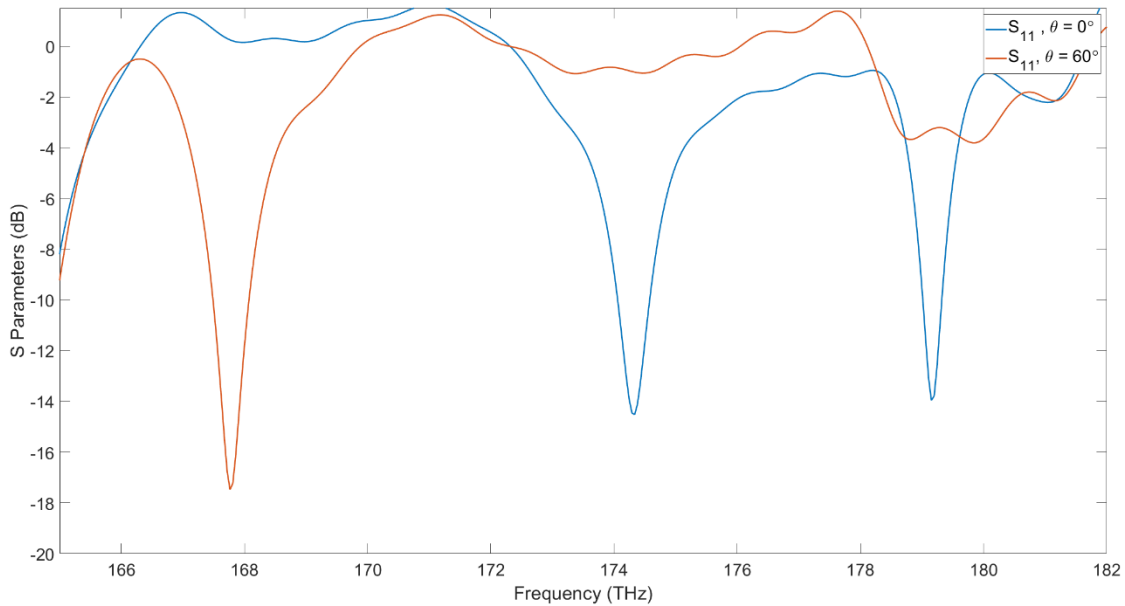


**Figure 10.** Reflection parameter obtained by simulation at different low symmetry rod angle values in the indirectly coupled cavity ( $rs=0.1a$ )

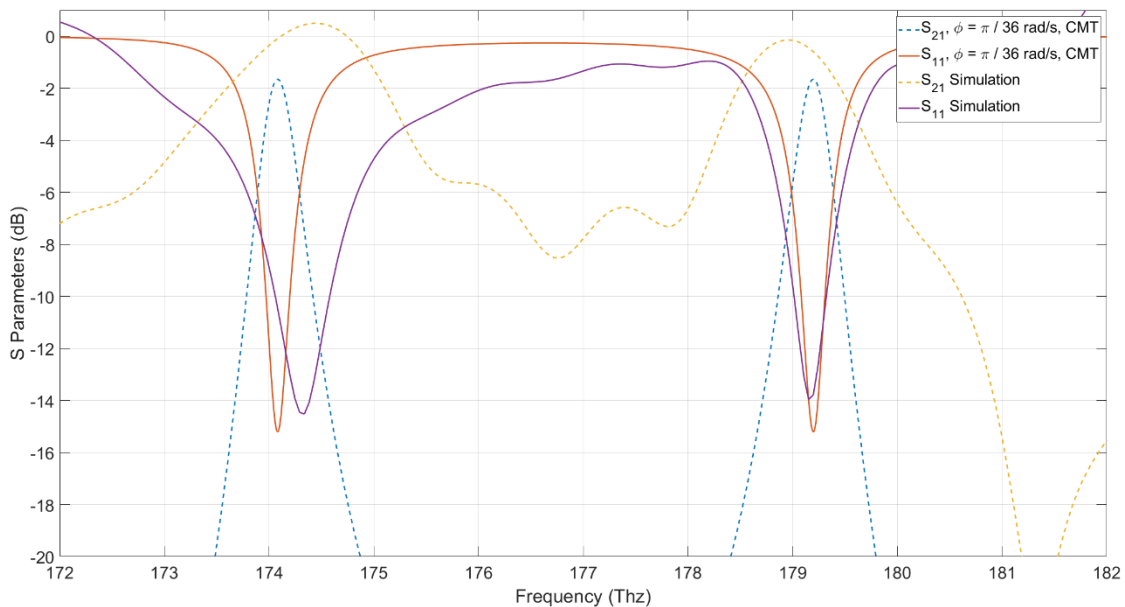


**Figure 11.** Comparison of CMT calculation and simulation result in the indirectly coupled cavity ( $Q_i=4 \times 10^3$ ,  $Q_w=2 \times 10^2$ ,  $\theta=0^\circ$  ve  $rs=0.1a$ )

### 4.3. Microwave Measurement Setup Proposal

The final stage of the study involved setting up a microwave measurement system for the designed cavity structure to measure the transmission and reflection coefficients. Due to the scalable characteristic of photonic crystals, conducting experiments in the microwave region is an acceptable method in literature. Sub-micron-scale device fabrication and testing require highly costly nanomanufacturing conditions. However, it is also clear that the structures developed for the microwave region cannot be directly applied as photonic devices. Nevertheless, waveguides, splitters, and resonant cavities developed using this technique provide proof of concept essential for advancing our understanding of the interaction between electromagnetic waves and disordered media. In the measurement setup shown in Figure 12, the low-symmetry, direct-coupled, zero-degree configuration cavity structure is shown within a photonic crystal structure consisting of alumina rods arranged in a square lattice. Alumina can be chosen as a dielectric material for the rods, or the rods can be fabricated using 3D printing techniques with materials such as PLA, ABS etc.. In this case, the dielectric constant of the simulated rods should match the dielectric constant of the experimental rods. Since the dielectric constant of the material varies according to the frequency studied, this situation should also be taken into consideration. Additionally, irregularities in the manufacturing process, such as variations in rod diameter or material impurities, can yield erroneous results. To mitigate potential negative effects during measurement, materials with low dielectric constant, such as Plexiglas, can be used as the base plate on which the rods are placed, and the medium can be surrounded by absorber layers. A horn antenna connected to a vector network analyzer was used to apply a source in the range of 8.2 GHz to 12.4 GHz at the input, while the output was measured using an equivalent horn antenna. The scalability property of photonic crystals allows for the frequency range to be adjusted by changing the lattice constant. For example, with a lattice constant of 1.58 cm and 1  $\mu\text{m}$ , the corresponding actual frequencies for a normalized frequency of 0.59 are 11.2 GHz and 177 THz, respectively. In this setup, the lattice constant ( $a$ ) was selected as 15.8 mm. Accordingly, the actual dimensions of the rods used in the experiment were determined. For instance, a rod with a radius of  $0.2a$  was implemented as a rod with a radius of 3.16 mm. Since two-dimensional (2D) structures effectively represent many scenarios in photonic crystal-based designs, simulations are typically conducted in 2D, with the third dimension considered infinitely long. Adding the third dimension to simulations significantly increases computational time, approximately proportional to the cube of the dimensions. In the experimental setup, the third dimension of the rods is also present. However, rods of about 15 cm or 20 cm in length, which is about eight to ten times the working wavelength, can

be acceptable as the infinite length considered in the simulations in this study.

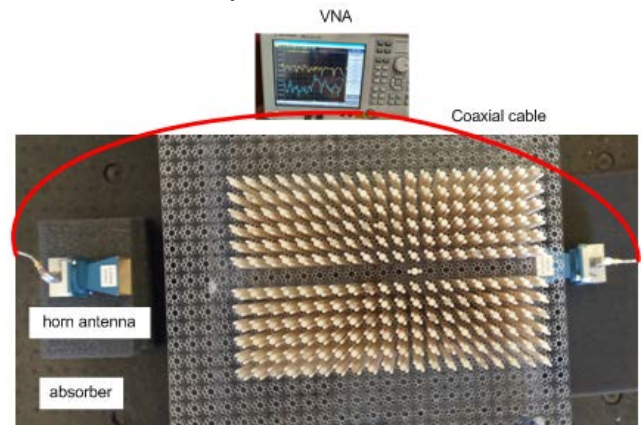


**Figure 12.** Experimental setup measured in the microwave region

The transmission bands observed in the experimental results were consistent with the frequency ranges predicted in the simulations. In this respect, the simulation and experimental results agree. However, deviations in the material parameters and differences between the experimental setup and the simulation environment affected the S-parameter values, leading to inaccuracies. For example, the diameters of the dielectric rods were not uniformly distributed, and their dielectric constants varied due to material impurities. Furthermore, in simulations, the source was placed directly within the structure, but this configuration could not be replicated in the microwave measurement setup. In the simulation environment, the structure was isolated from external influences using a perfectly matched layer (PML), which could not be achieved experimentally. Consequently, the experimental results were excluded from the study.

## 5. Conclusion

In contrast to traditional high-symmetry structures, low-symmetry photonic crystal structures have opened up a new perspective on light manipulation, offering a wide range of geometric possibilities. This study differs from previous research in that it investigates the effect of angular and dimensional variations in a low-symmetry structure on the cavity resonance mode. The results show that manipulation of the low-symmetry property can lead to the splitting of the resonant mode. The results of this study provide a novel perspective on light transmission and manipulation in low-symmetry photonic crystal structures.

## 6. Acknowledgements

This study is supported by TUBITAK (The Scientific and Technological Research Council of Turkey) with the project no 118E954. I would like to thank the anonymous referees for their comments.

## REFERENCES

- [1] Joannopoulos JD, Johnson SG, Winn JN, Meade RD. *Photonic Crystals: Molding the Flow of Light, Second Edition*. New Jersey USA, Princeton University Press, 2008.
- [2] Mingaleev S, Kivshar Y. “Nonlinear photonic crystals toward all-optical technologies”. *Optics & Photonics News*, 13 (7), 48, 2002.
- [3] Li Q, Wang T, Su Y, Yan M, Qiu M. “Coupled mode theory analysis of mode-splitting in coupled cavity system”. *Optics Express*, 18 (8), 8367–82, 2010.
- [4] Mekis A, Chen JC, Kurland I, Fan S, Villeneuve PR, Joannopoulos JD. “High Transmission through sharp bends in photonic crystal waveguides”. *Physical Review Letters*, 77 (18), 3787–3790, 1996.
- [5] Fan S, Villeneuve P, Joannopoulos J, Haus H. “Channel drop filters in photonic crystals”. *Optics Express*, 3 (1), 4, 1998.
- [6] Noble E, Nair RV, Jagatap BN. “Interaction between dual cavity modes in a planar photonic microcavity”. *Journal of Modern Optics*, 63 (19), 1981-1991, 2016.
- [7] Prorok S. “Nanophotonics and integrated optics photonic crystal cavities”. CST Computer Simulation Technology, Darmstadt Germany, whitepaper, 18.04.2013.
- [8] Zhang Z, Dainese M, Wosinski L, Qiu M. “Resonance-splitting and enhanced notch depth in SOI ring resonators with mutual mode coupling”. *Optics Express*, 16 (7), 4621, 2008.
- [9] Mahmoodian S, McPhedran R, Sterke C, Dossou K, Poulton C, Botten L. “Single and coupled degenerate defect modes in two-dimensional photonic crystal band gaps”. *Physical Review A*, 79 (1), 013814, 2009.
- [10] Daraei A, Khozayemeh F. “Investigation on mode splitting and degeneracy in the L3 photonic crystal nanocavity via unsymmetrical displacement of air-holes”. *The International Journal of Engineering and Science*, 2 (2), 146–150, 2013.
- [11] Karakilinc OO, Dinleyici MS. “Design of dual-mode dual-band photonic crystal bandpass filters for terahertz communication applications”. *Microwave and Optical Technology Letters*, 57 (8), 1806-1810, 2015.
- [12] Yuksel ZM, Oguz H, Karakilinc OO, Turdnev M, Berberoglu H, Adak M, Kart SO. “Enhanced self-collimation effect by low rotational symmetry in hexagonal lattice photonic crystals”. *Physica Scripta*, 99, 065017, 2024.
- [13] Turdnev M, Giden I. H., and Kurt H. “Modified annular photonic crystals with enhanced dispersion relations: polarization insensitive self-collimation and nanophotonic wire waveguide designs”. *Journal of the Optical Society of America B*, 29(7):1589–1598, 2012.
- [14] Gumus M. A., Tutgun M, Yilmaz D, and Kurt H. “A reduced symmetric 2D photonic crystal cavity with wavelength tunability”. *Journal of Physics D: Applied Physics*, 52(32):325103, 2019.
- [15] Giden I. H., Turdnev M., and Kurt H. “Reduced symmetry and analogy to chirality in periodic dielectric media”. *Journal of the European Optical Society - Rapid publications*, 9(0), 2014. ISSN 1990-2573.
- [16] Giden I. H., Turdnev M., and Kurt H. “Broadband supercollimation with low-symmetric photonic crystal”. *Photonics and Nanostructures - Fundamentals and Applications*, 11(2):132–138, 2013.
- [17] Gumus M., Akcaalan O., and Kurt H. “Crossed chiral band approximation for wide-band self-collimation of light”. *Journal of Physics D: Applied Physics*, 53(23):23LT03, 2020.
- [18] Erim N., Erim M. N., and Kurt H. “An optical sensor design using surface modes of low-symmetric photonic crystals”. *IEEE Sensors Journal*, 19(14):5566–5571, 2019.
- [19] Giden I. H. “Photonic crystal based interferometric design for label-free all-optical sensing applications”. *Optics Express*, 30(12):21679–21686, 2022.
- [20] Gumus M., Giden I. H., and Kurt H. “Enhanced superprism effect with self-collimation by dispersion management in C1 symmetric photonic crystals”. In Ali Adibi, Shawn-Yu Lin, and Axel Scherer, editors, *Photonic and Phononic Properties of Engineered Nanostructures VIII*, 10541, 105411L, SPIE, 2018.
- [21] Yasa U. G., Giden I. H., Turdnev M., and Kurt H. “Polarization splitting phenomenon of photonic crystals constructed by two-fold rotationally symmetric unit-cells”. *Journal of Optics*, 19(9):095005, 2017.
- [22] Chun-ping C, Anada T, Greedy S, Benson TM, Sewell P. “A novel photonic crystal band-pass filter using degenerate modes of a point-defect microcavity for terahertz communication”. *Microwave and Optical Technology Letters*, 56 (4), 792–797, 2014.
- [23] Xia P, Fu Y, Kong M, Liu Z, Zhou J, Zhou J. “Theoretical analysis of the mode splitting properties in periodically patterned microring resonators”. *Journal of Lightwave Technology*, 35 (9), 1700-1704, 2017.
- [24] Gumus M, Giden HI, Kurt H. “Broadband self-collimation in C2 symmetric photonic crystals”. *Optics Letters*. 43, 2555-2558, 2018.
- [25] Pendry JB, MacKinnon A. “Calculation of photon dispersion relation”, *Physics Review Letters*, 69 (19), 2772-2775, 1992.
- [26] Taflove A. *Computational Electrodynamics: The Finite-Difference Time Domain Method*. Boston: Artech House, 2005.
- [27] Pendry JB. “Calculating photonic band structure”. *Journal of Physics: Condensed Matter*, 8 (9), 1085-1108, 1996.

- [28] Pelosi G, Coccioli R, Selleri S. Quick finite elements for electromagnetic waves. Boston USA, Artech House, 1997.
- [29] Oskooi AF, Roundy D, Ibanescu M, Bermel P, Joannopoulos JD, Johnson SG. “Meep: A flexible free-software package for electromagnetic simulations by the FDTD method”. *Computer Physics Communications*, 181 (3), 687–702, 2010.